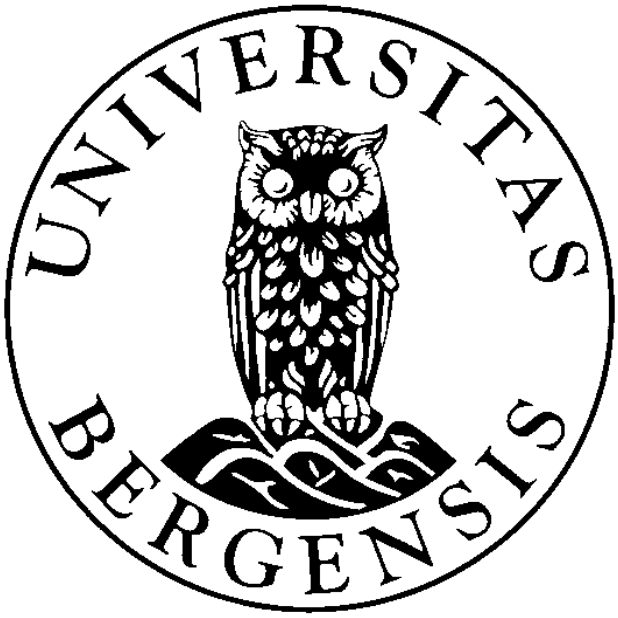

Pore-scale investigation of methane hydrate phase transitions and growth rates in synthetic porous media

Master Thesis in Reservoir Physics

By
Maksim Lysyy

Department of Physics and Technology
University of Bergen

June 2018

Abstract

A growing demand for energy and natural gas in particular, makes methane gas hydrates a potential target to supplement natural gas production from conventional resources. Several pilot projects have proven the feasibility of gas production from hydrates both onshore and offshore, but the proposed models of gas hydrate behavior in sediments lack experimental support. In particular direct pore-scale observations of gas hydrate phase transitions can assist in a better understanding of the fundamentals of gas hydrate phase transitions in sedimentary systems. In this thesis, methane gas hydrate formed from methane gas and distilled water was visually investigated in high-pressure micromodel based on a thin section of Berea sandstone. The main objective of this work was to supplement previous research at the Reservoir Physics groups to determine hydrate formation and dissociation mechanisms on pore scale; and to estimate the hydrate growth rates.

Fifteen primary and twenty-two secondary hydrate formation experiments were performed in this work. The first seven primary formations were carried out with initial water saturation ranging from 0.30 to 0.60 and nearly constant pressure (83-84 bar) and temperature (1.2-1.4 °C), with the main intention to study the hydrate formation mechanisms and the effect of initial water saturation and pore sizes on the hydrate growth rates. The remaining experiments were conducted at various pressure-temperature conditions to further investigate formation mechanisms and provide growth rate measurements as function of driving force (degree of subcooling).

The hydrate formation was first observed in the continuous water-gas interface, followed by hydrate growth into trapped gas. For both gas configurations, the hydrate growth initiated at the water-gas interface along the pore walls and then progressed towards the pore center. The hydrate growth resulted in two different hydrate configurations: crystalline hydrate with total gas consumption and hydrate films/shell with enclosed gas. Hydrate was also observed to grow in water at the water-hydrate interface, but this was rare and restricted to locations where the free gas was available within a relatively short distance. Massive growth in water was only achieved due to forced dissolution of methane in water.

The hydrate formation was quantified by estimating the hydrate film growth rates. The hydrate growth at the water-gas interface along the pore walls was approximately two orders of magnitude faster compared to the hydrate growth towards pore center. The hydrate film growth rates were studied with respect to initial water saturation, pore sizes and driving force (degree of subcooling, ΔT). No clear effect of initial water saturation and pore sizes on the growth rate was observed. The hydrate growth rate towards the pore center seemed to increase with driving force but the relationship was weak. The growth rate along the pore walls was proportional to ΔT^2 and showed a good agreement with the measurements of hydrate film growth reported in literature for bulk systems.

Thirty-four hydrate dissociation experiments were conducted by reducing the pressure several bars below the equilibrium pressure. The hydrate dissociation was studied with respect to hydrate configurations (crystalline and hydrate films/shell). The dissociation of crystalline hydrate was slower and resulted in a gas front that flowed through the pore space, inducing further hydrate dissociation. The dissociation of hydrate films/shell with enclosed gas initiated in the pore center and then continued towards the pore walls, leading to the mobilization of enclosed gas. The direct contact with mobile gas rather than water favored hydrate dissociation. The overall dissociation rate of crystalline hydrate seemed to increase with decreasing hydrate saturation.

Acknowledgements

This work would have not been possible without contribution from others. I would like to express my gratitude to the following persons:

To my supervisor, Associate Professor Geir Ersland, for providing an opportunity to work with such a fascinating topic as gas hydrates. His guidance and support cannot be overstated. He always systematized my ideas and thoughts and pointed me to the right direction. I am especially grateful for a possibility to improvise and work independently.

To PhD candidate Stian Almenningen, for his help in the laboratory and for general advices related to this master thesis. Our discussions enabled me to look at my project from a different perspective.

To Professor Martin Fernø, for introducing me various image processing software and for giving me valuable scientific advices. To Professor Arne Graue, for leading the Reservoir Physics group; and to all other members of the Reservoir Physics group, for creating a productive as well as cheerful environment during these years.

To my parents, Larisa and Stepan, for teaching me good study habits and for supporting me in everything I do.

To my girlfriend, Kristina, for always believing in me and for creating a positive environment at home while tough days of writing the thesis. Her endless support was absolutely invaluable. I dedicate this work to her.

Table of Contents

Introduction

Being the fastest-growing fossil fuel, natural gas plays an important role in the world's energy supply. Its worldwide consumption is expected to increase by 45 % in 2040 compared with 2016 (International Energy Agency, 2017). With growing environmental concern, natural gas is more preferred over other fossil fuels due to its significantly lower emissions of greenhouse gases to the atmosphere upon combustion. However, natural gas is non-renewable source of energy and the world may face the shortage of natural gas in not-too-distant future. Unconventional gas reserves such as natural gas hydrates can potentially meet the growing demand for natural gas. Gas bound in natural hydrate reserves are vast but uncertain where estimates range between 10^{14} and 10^{18} Sm^3 (Sloan & Koh, 2008). Nevertheless, even the lower end estimates suggest that the amount of energy trapped in natural gas hydrates compares to energy bound in all the conventional fossil fuels combined. Although only a fraction of these estimates is a target for exploitation (Moridis et al., 2011), gas hydrates can potentially become one of the most promising alternative future energy resources.

Gas hydrates are solid compounds consisting of gas molecules trapped inside water molecules. They have an ice-like physical appearance and typically form under high pressures and low temperatures in the sub seafloor under water columns of 4-500 meters and in regions with permafrost. Pressure-temperature conditions, heat and mass transport and the availability of water and gas are key parameters affecting gas hydrate formation. The hydrates can be detected by seismic waves and well-logs (Goldberg & Saito, 1998; Hornbach et al., 2003).

Production of natural gas from hydrates typically involves depressurization, thermal stimulation, inhibitor injection (Makogon, 1997). In both depressurization and thermal stimulation production techniques, the hydrates are destabilized by pressure reduction and temperature increase respectively. Injection of inhibitors such as salts or alcohols shifts the hydrate stability curve to higher pressures and lower temperatures, thereby destabilizing the gas hydrates at local pressure-temperature conditions. Besides three most common means to extract natural gas from hydrates, several alternative production techniques have been proposed, including $\mathrm{CH}_4 - \mathrm{CO}_2$ exchange. The main challenge associated with methane production from hydrates is that the fuel is in the solid state, and the fluids must therefore first be mobilized. For this reason, conventional hydrocarbons recovery techniques are difficult to apply (Lee & Holder, 2001).

Despite steadily increasing number of hydrate-related publications, the fundamentals of gas hydrate are still not appropriately studied and therefore further research in this field is required to understand phase behavior and mobilization of fluids in sediments. Recent studies of gas hydrates at the Reservoir Physics group have focused on the hydrate phase transitions on core- and pore-scale involving MRI and microscopic visualization as imaging techniques. This master thesis will further investigate the gas hydrate formation and dissociation on pore-scale, with focus on the hydrate formation/dissociation mechanisms; and the effect of initial fluid saturations, pore sizes and driving force on the hydrate film growth rates.

1 Theoretical part

This chapter provides an insight into gas hydrate phenomenon. Sections 1.1-1.3 introduce the general natural gas phenomenon, describe the knowledge history of gas hydrate and explain different hydrate structures. The aim of this thesis is to study the hydrate formation and dissociation mechanisms on pore-scale; and main focus of this chapter is kept on a microscopic phenomenon of gas hydrates as it will assist in the interpretation of the experimental results obtained in this work.

1.1 General overview

Natural gas hydrates are crystalline compounds developed from a mixture of gas molecules ("guest") trapped inside hydrogen-bonded water molecules ("host") at high pressures (typically more than 0.6 MPa) and low temperatures (typically less than 27 °C). Gas hydrates are abundantly present in the ocean and in the permafrost regions where pressure and temperature are favorable for hydrate thermodynamic stability. Figure 1.1 shows hydrate stability conditions for two different geological settings: permafrost (Figure 1.1a) and marine (Figure 1.1b). The hydrate stability zone (HSZ) is colored yellow and is generally thicker in permafrost than in ocean. Its thickness is strongly dependent on the geothermal gradient in sediments. About 97% of natural gas hydrates reserves are accumulated in marine sediments, and only 3 % in permafrost (Makogon, 2010).

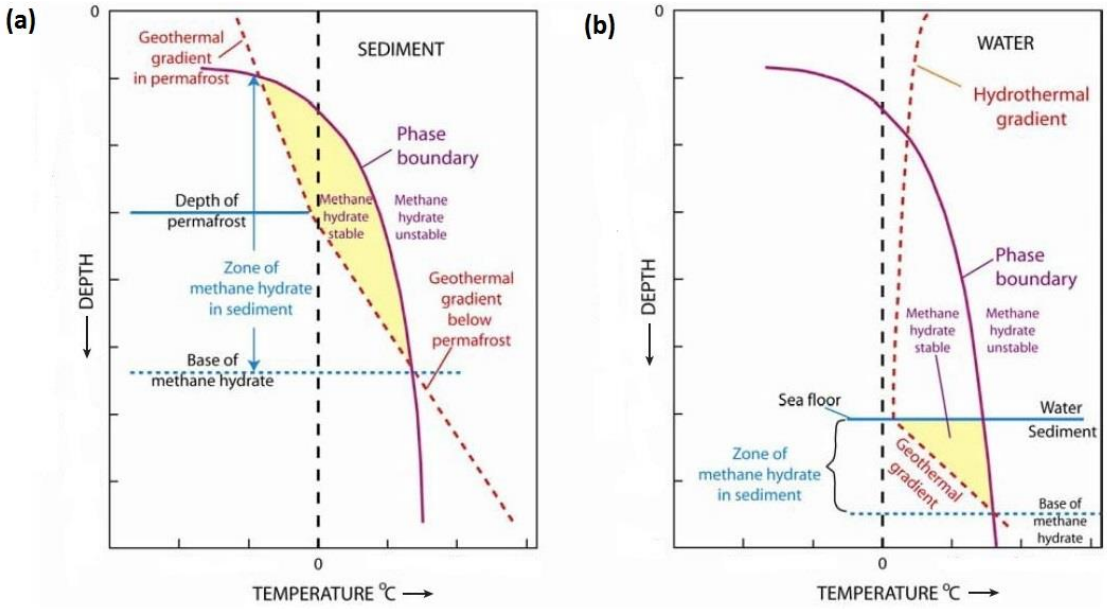

Figure 1.1. Hydrate stability zone for (a) permafrost and (b) ocean regions (Modified from Sloan et al., 2010).

The gas and water composition together with pressure-temperature conditions determine the composition of a hydrate. Methane, ethane, propane, and carbon dioxide are typical gas hydrate formers, with methane being most abundant component (Makogon, 2010). Over geological time, the hydrate composition can change due to variations in thermodynamic conditions and water and gas migration. The occurrence of hydrates with a significant fraction of heavier components has been reported (Table 1.1).

Methane gas in natural hydrates originate from biogenic (from bacterially produced methane) and thermogenic (generated by high-temperature catagenesis) sources, with biogenic methane being the most abundant (Sloan & Koh, 2008). The methane hydrate can form in nature either due to (1) in-place generation of methane dissolved in water or (2) upward migration of dissolved and free methane.

Table 1.1. Composition of natural gas hydrates (Modified from Makogon, 2010).

Gas hydrate deposit	Gas composition, mol %							
	CH_4	C_2H_6	C_3H_8	iC_4H_{10}	nC_4H_{10}	C_{5+}	CO_2	N_2
Nankai Trough	99.3						0.63	
Bush Hill White	72.1	11.5	13.1	2.4	1			
Green Canyon White	66.5	8.9	15.8	7.2	1.4	0.2		
Bush Hill	29.7	15.3	36.6	9.7	4	4.8		
Messoyakha	98.7	0.03					0.5	0.77
Mallik	99.7	0.03	0.27					

Methane has a lower solubility in water compared with non-organic hydrate formers. For example, the solubility of carbon dioxide is nearly two orders of magnitude higher compared with methane at STP (The Engineering ToolBox, n.d.; *b*). The solubility of gases in water is temperature-dependent. The presence of gas hydrates in the system alters the temperature-dependence trend. The methane concentration in water decreases with increasing temperature in the absence of gas hydrates, whereas it shows the opposite trend when the gas hydrates are present in the system (Figure 1.2).

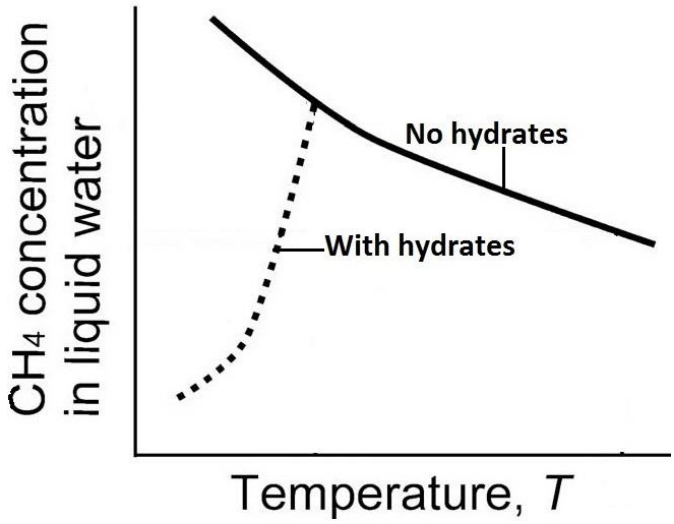

Figure 1.2. The effect of temperature on the methane concentration in water at constant pressure with the presence of hydrates (dashed curve) and without (solid curve) (Modified from Katsuki et al., 2008).

Natural gas hydrates can potentially become a significant energy resource. However, the production of gas from hydrates may involve geomechanical challenges. The hydrate-bearing sediments suitable for gas extraction are often poorly consolidated with limited shear strength (Moridis et al., 2011). Thus, the dissociation of solid-state gas hydrate can weaken the structural strength of the sediments that can result in the slope failure and consequent possible marine hazards such as tsunamis (Figure 1.3). Furthermore, it was suggested that gas hydrates might have an impact on a global climate change due to methane release from gas hydrates caused by seasonal alterations in pressure and temperature as a result of a sea-level variations (Macdonald, 1990). In addition, the occurrence of hydrates is undesired in processing engineering due to their ability to plug pipelines.

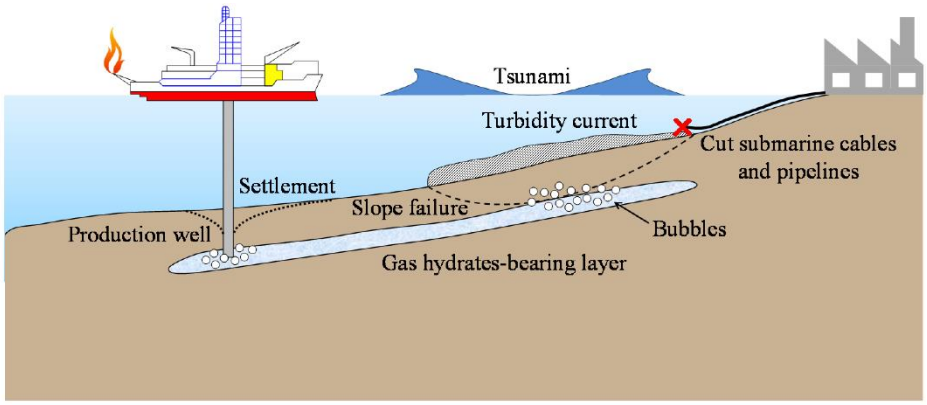

Figure 1.3. Illustration of possible hazards in marine sediments caused by gas production from hydrates (Iwai et al., 2015).

1.2 Historical perspective

Sir Humphrey Davy's discovery of chlorine hydrate in 1810 is generally considered as the first observance of hydrates. Following this discovery, researchers in the field attempted to provide a quantitative description of hydrates formed from inorganic formers such as chlorine, bromine, and carbon dioxide. Villard first identified the existence of organic hydrates in 1888 (Sloan & Koh, 2008).

Until 1930s, gas hydrates were only considered as a laboratory curiosity. Hammerschmidt (1934) first discovered hydrates as pipeline plugs, and studied the effect of thermodynamic inhibitors on hydrates, with methanol being one of the most valuable inhibitors at that time. In the late 1940s and early 1950s, Von Stackelberg and his coworkers reported two decades of x-ray diffraction experiments on hydrate crystals, that enabled researchers to investigate two different forms of gas hydrates, namely structures- I and II (Sloan & Koh, 2008). Ripmeester et al. (1987) discovered a third hydrate structure (structure H). Discovery of different hydrate structures enabled researchers to predict hydrate thermodynamic properties more accurately. In 1959, Van der Waals and Platteeuw proposed statistical theory, which provides the basis for current thermodynamic models (Sloan & Koh, 2008).

It was not until the middle of 1960s, when a Soviet scientist Makogon first announced the potential of gas hydrates as an energy resource, that a large experimental effort related to production of natural gas from hydrates begun (Sloan & Koh, 2008). The first major gas hydrate accumulation was discovered by a Soviet drilling crew in the Siberian Messoyakha field, which was set to commercial exploitation in 1969, with a decade of gas production, possibly from hydrates (Sloan & Koh, 2008; Demirbas, 2010). The above discovery initiated further geological research around the world where gas hydrates could be discovered.

The existence of gas hydrates in oceanic sediments was inferred based on the seismic observations (Demribas, 2010). The discovery of oceanic gas hydrates has increased the interest in offshore hydrate accumulations. In 1992, the Ocean Drilling Program initiated the drilling activities offshore intended to expand the knowledge about oceanic hydrate deposits, and hydrate cores in the deep waters were recovered for further study (Sloan & Koh, 2008; Demirbas, 2010).

Since Makogon's announcement of the gas hydrate potential as an energy resource, many researchers have doubted the possibility of commercial exploitation of gas from hydrates, mainly due to economic and technical reasons (Collett, 2008). However, the last decades the paradigm has changed from evaluation of hydrate accumulations to production of gas from hydrates. A major breakthrough came in 2002, when gas hydrate production testing was conducted in permafrost regions in the Mallik well in Canada. This project provided the evidence for technical and commercial feasibility of gas extraction from hydrates by combining pressure reduction and thermal stimulation techniques (Sloan & Koh,

2008). Furthermore, the Mount Elbert test well was drilled in the Alaska North Slope in 2007 intended to collect a set of well-log, core and downhole production test data (Collett, 2008). In addition to the Mallik 2002 program, another onshore production field trial started in the Ignik Sikumi #1 well in Alaska in 2011 where the alternative production technique ($CH_4 - CO_2$ exchange) was successfully tested (Schoderbek et al., 2012).

Besides onshore production tests, the National gas hydrate programs were launched by several Asian countries in order to enhance overall understanding of marine gas hydrates (Collett, 2008). In 2013, the first offshore field test was carried out by a depressurization technique in the Eastern Nankai Trough off the Pacific coast of Japan. Even though the test terminated after 6 days due to critical sand production, this field trial demonstrated the applicability of pressure reduction technique even in marine deposits (Yamamoto et al., 2014; Li et al., 2016). Following the Nankai Trough 2013 project, the second marine gas hydrate production testing has been planned in the Eastern Nankai Trough to confirm more stable and prolonged gas production; and the drilling survey campaign begun in 2016 to obtain the logging data ahead of the production test (Tamaki et al., 2017). Furthermore, China conducted its first production test in South China Sea in May 2017 that has lasted for approximately 6 weeks (Yanlong et al., 2017).

Table 1.2. Milestones in the gas hydrate history.

Year	Event
1810	Chlorine hydrate discovery by Davy
1888	Villard observed organic gas hydrates
1934	Hammerschmidt discovered hydrates to plug gas pipelines
1969	Gas production began in the Siberian Messoyakha field, possibly from hydrates
1992	Ocean Drilling Program intended to discover gas hydrate deposits began
2002	Mallik field test in Canada demonstrated that gas hydrates could be economically and technically produced in the permafrost regions
2013	Nankai Trough field test confirmed the possibility of gas recovery from marine sediments

1.3 Hydrate structures

Gas hydrates are crystalline complexes composed of hydrogen-bonded water molecules that are able to accommodate gas molecules inside their lattice cavities (or cages). The crystalline lattice becomes stable when the guest gas molecules occupy the minimum number of cavities, thereby preventing the breakage and strain of the hydrogen bonds (Sloan, 2003). In addition to the water- “guest” interactions inside the lattice, the cavities are stabilized by their shape and size.

The existence of several hydrate structures has been discovered, based on the arrangement of water molecules in the crystalline structure. Three are three common forms of natural gas hydrates: two cubic structures I (sI) and II (sII) and one hexagonal structure H (sH). Figure 1.4 provides a visual illustration of these structures and their constituents.

Besides three most commonly accepted hydrate forms, the observance of unusual hydrate structures has been reported. For example, Jeffrey’s structures III to VII, with bromine being a hydrate former in structure III and no “true” hydrates known for structures IV or V. Since the occurrence of these hydrates is extremely rare, their detailed description is not provided in this work. This chapter describes the main features of hydrate structures I, II and H, as outlined by Sloan and Koh (2008), from which much of the below discussion has been excerpted.

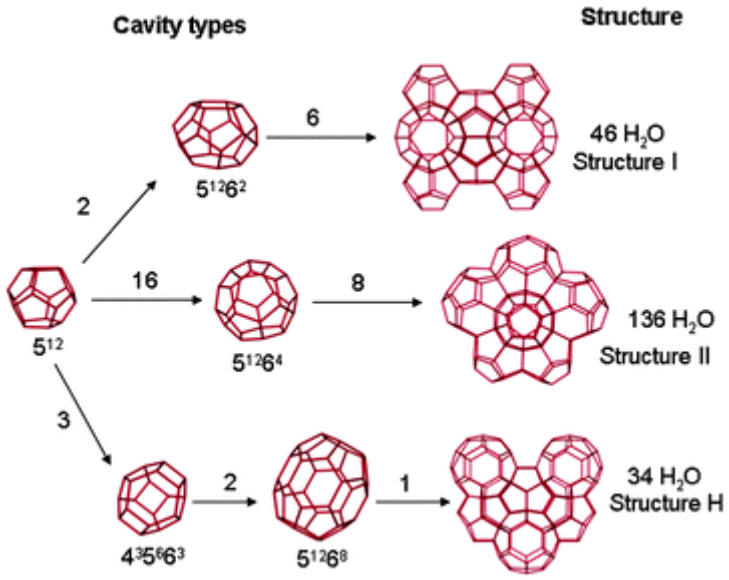

Figure 1.4. Different cavities and structures in gas hydrates (Steed and Atwood, 2009).

Structure I (sI)

In sI hydrate, the smallest symmetrical structure is a 12 Å cube consisting of 46 water molecules that has two types of cavities: small and large (Figure 1.5). Structure I predominates in nature; and the occupancy of one cavity type only is sufficient for stability (Sloan, 2003).

Two small cavities are pentagonal dodecahedra (5^{12}), e.g. they are composed of twelve pentagonal faces. This type of cavity has an average radius 3.95 Å that is perfectly sized for small guest molecules such as methane. The cavities have almost spherical shape.

Six large cavities are tetradecanhedra ($5^{12}6^2$), e.g. have twelve pentagonal and two hexagonal faces. Since they have an average radius 4.33 Å, large cavities are capable of accommodating methane molecules. In addition, large cavities fit well for larger molecules such as ethane and carbon dioxide. The large cavities are slightly oblate.

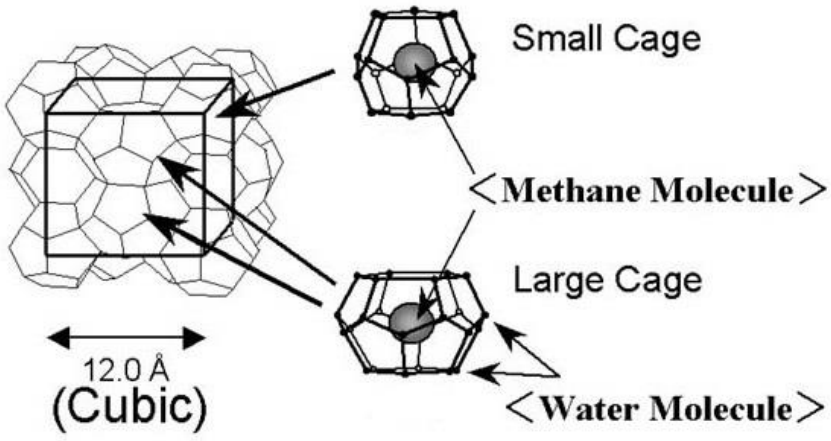

Figure 1.5. Schematic of structure I hydrate (Modified from Kitami Institute of Technology, n.d.).

Structure II (sII)

The unit cell of sII hydrate is a 17.3 Å cube consisting of 136 water molecules that has small and large cavities. Structure II occurs in mostly artificially created systems, and is stabilized by filling one cavity type only (Sloan, 2003).

Sixteen small cavities have pentagonal dodecahedra (5^{12}) shape. They have an average radius 3.91 Å and thus can be occupied by the smallest hydrated molecules, for instance oxygen and nitrogen. The small cavities are distorted.

Eight large cavities are hexadecahedra ($5^{12}6^4$), e.g. have twelve pentagonal and four hexagonal faces. Large cavities have an average radius 4.73 Å and consequently can be filled by larger molecules such as propane and iso-butane. This type of cavities has almost spherical shape.

Structure H (sH)

The smallest symmetrical structure in sH hydrate is a hexagonal system with lattice parameters *a* = 12.2 Å and *c* = 10.1 Å consisting of 34 water molecules and having small, medium and large cavities. Structure H may occur in both man-made and natural environments (Sloan, 2003). Nevertheless, sH hydrate stabilizes only when the molecules of appropriate size occupy both small/medium and large cavities.

Three small cavities have pentagonal dodecahedra (5^{12}) and an average radius 3.94 Å. Two medium cavities ($4^3 5^6 6^3$) with an average radius 4.04 Å have three square, six pentagonal and three hexagonal faces. Small molecules such as methane can occupy both small and medium cavities.

One large cavity ($5^{12}6^8$) has twelve pentagonal and eight hexagonal faces and an average radius 5.79 Å. The large cavity can host even larger molecules such as neohexane. Therefore, mixtures of small and large molecules such as methane and neohexane can potentially form gas hydrates.

1.4 Hydrate formation and dissociation

Unlike structures and thermodynamics of hydrates, hydrate formation and dissociation are kinetic time-dependent phenomena. The hydrates form when both hydrate-former and water molecules are available in sufficient quantities and the system is within hydrate stability zone. On molecular level, the hydrate formation process can be divided into nucleation and growth stages. The hydrates dissociate when the pressure-temperature conditions are outside the hydrate stability region. Since this thesis emphasizes the hydrate formation and dissociation on a pore-level, a detailed description of microscopic phenomenon of gas hydrates is provided in this section.

1.4.1 Hydrate nucleation

Hydrate nucleation is the process during which small clusters of water and gas grow and dissipate to reach the critical size at which continued (stable) growth is possible (Sloan & Koh, 2008). Nucleation is the critical step in understating the formation of hydrates. Even though several hypotheses attempt to explain nucleation, its mechanism is not known with any degree of certainty. Three main limitations complicate the study of hydrate nucleation (Sloan & Koh, 2008). First, being a microscopic phenomenon with tens to thousands of molecules involved; the nucleation stage is difficult to observe experimentally. Second, this stage is a statistically probable (but not deterministically certain) process. Third, nucleation is associated with high degree of metastability that can be defined as the ability of a nonequilibrium state to persist for a long period of time.

Different nucleation nomenclature can be found in the literature. To avoid inconsistency, the discussion of nucleation in this thesis will refer to the theory of homogeneous and heterogeneous nucleation in crystallization, as outlined by Mullin (2001) and Sloan and Koh (2008).

Homogeneous nucleation (HON)

Homogenous nucleation is a spontaneous crystallization process that occurs in systems in the absence of impurities such as foreign particles and/or surfaces. A stable crystal nucleus may contain up to

several thousand molecules. Nevertheless, the simultaneous collision of the required number of molecules that can form a stable nucleus is an extremely rare event. It is more probable that a stable nucleus could result from a sequence of biomolecular collisions according to the following scheme:

$A + A \leftrightarrow A_2$ (cluster containing two molecules)

$A_2 + A \leftrightarrow A_3$ (cluster containing three molecules)

$A_{n-1} + A \leftrightarrow A_n$ (critical cluster)

Initially, two molecules collide to form a cluster (embryo). A newly formed cluster combines with another molecule/cluster, thereby creating a new cluster of increased size. Sequential cluster growth continues until the critical cluster size is reached. Before a cluster attains a critical size, many of clusters fail to achieve maturity and they simply redissolve because of density or composition fluctuations. However, after achieving the critical size, further molecular collisions with the critical cluster would cause nucleation and successive stable growth of the nucleus. Since a critical nucleus is too small to observe directly, its structure is not known.

The formation of critical cluster size and spontaneous growth is governed by the excess Gibbs free energy, ΔG, between a small solid particle of solute (assumed to be a sphere of radius *r*) and the solute in solution. This can be expressed as the sum of the surface excess free energy, ΔG_s, and the volume excess free energy, ΔG_v:

$$\Delta G = \Delta G_S + \Delta G_V = 4\pi r^2\gamma + \frac{4}{3}\pi r^3 \Delta G_v \tag{1.1}$$

where ΔG_v is the free energy change per unit volume and γ is the interfacial tension between the crystalline surface and liquid in which it is located. The surface excess free energy and the volume excess free energy have the opposite signs, with surface excess free energy being a positive quantity (Figure 1.6). The function of the excess free energy has a maximum (ΔG_{crit}) at the radius corresponding to the critical cluster/nuclei, r_c. The expressions for ΔG_{crit} and r_c can be derived by differentiating equation 1.1 and setting the result to zero:

$$r_c = \frac{-2\gamma}{\Delta G_v} \tag{1.2}$$

and

$$\Delta G_{crit} = \frac{4\pi\gamma r_c^2}{3} \tag{1.3}$$

The equations above demonstrate that the critical cluster size is strongly dependent on a maximum of the excess free energy. ΔG_{crit} can be interpreted as an energy barrier that a cluster must overcome in order to achieve a critical size that is energetically favorable to sustain growth. Otherwise, nuclei are unstable and shrink if their size is less than the critical cluster size.

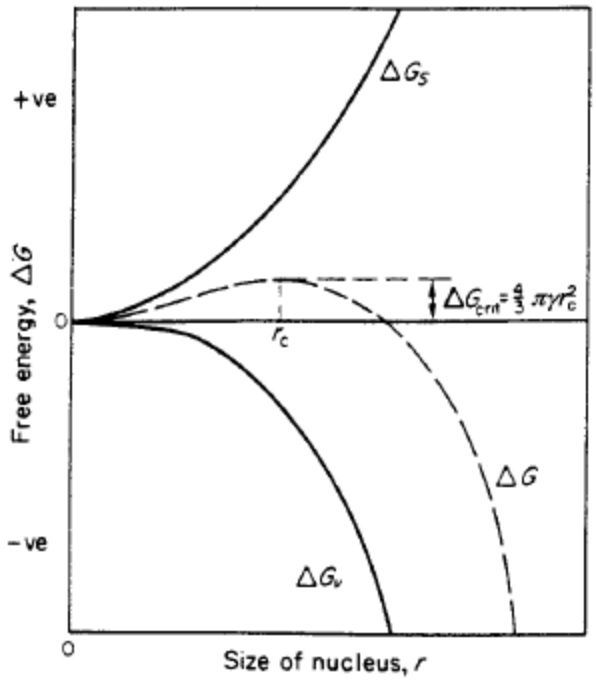

Figure 1.6. Free energy diagram for nucleation (Mullin, 2001).

Heterogeneous nucleation (HEN)

Heterogeneous nucleation is typical for systems containing impurities. Laboratory prepared aqueous solution may contain more than 10^6 solid particles per cm^3. Even though a careful filtration can reduce the number of foreign particles by three orders of magnitude, it is not practically possible to prepare impurities-free solution. It is generally agreed that true homogeneous nucleation is difficult to achieve and most systems nucleate heterogeneously.

It is thermodynamically feasible to achieve heterogeneous nucleation at degrees of supercooling lower than required for spontaneous nucleation. When a critical nucleus forms heterogeneously, the associated overall free energy change, $\Delta G'_{crit}$, must therefore be less than for spontaneous nucleation:

$$\Delta G'_{crit} = \phi \Delta G_{crit} \tag{1.4}$$

where ϕ is the factor less than one.

From equation 1.1, free energy change is affected by interfacial tension. In heterogeneous systems containing a solid surface, three different interfacial tensions arise (Figure 1.7). They are the solid crystalline-liquid interfacial tension, γ_{cl}; the foreign solid surface-liquid interfacial tension, γ_{sl}; and the solid crystalline-foreign solid surface interfacial tension, γ_{cs}. In the porous media saturated with gas hydrates, crystalline deposit and foreign solid surface relate to hydrate and grain respectively.

The factor ϕ in equation 1.4 is related to the contact angle between the crystalline deposit and a foreign surface, θ, according to the following expression:

$$\phi = \frac{(2 + \cos\theta)(1 - \cos\theta)^2}{4} \tag{1.5}$$

Contact angle θ provides the information about the wetting preference of a system. Figure 1.8 illustrates the relationship between the factor ϕ and contact angle θ. The fraction ϕ can be lowered

effectively by decreasing contact angle θ. Since $\Delta G'_{crit}$ is directly proportional to ϕ, the reduction of ϕ leads to lower values of $\Delta G'_{crit}$. Therefore, the nucleation is easier to achieve at lower contact angles between the crystalline deposit and a foreign surface.

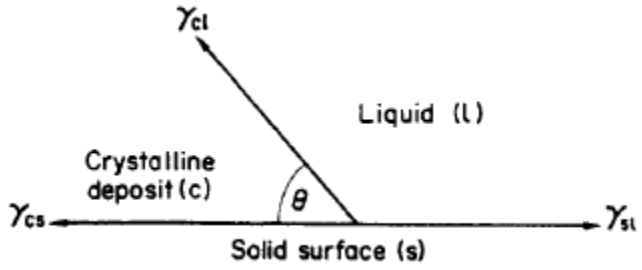

Figure 1.7. Interfacial tension diagram for a system containing two solids (crystalline deposit and foreign solid surface) and a liquid (Mullin, 2001).

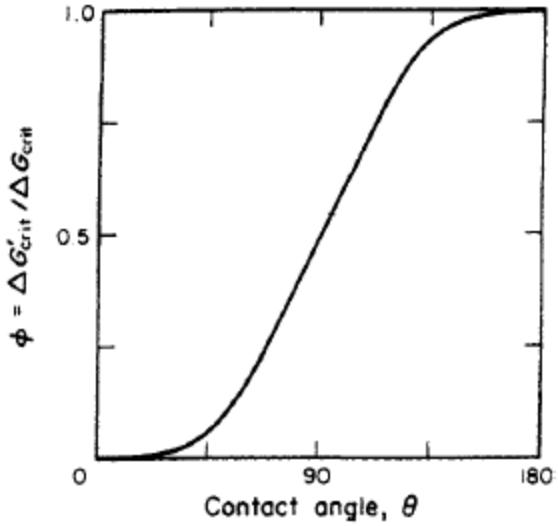

Figure 1.8. Ratio of overall free energy changes of homogeneous and heterogeneous nucleation as a function of the contact angle (Mullin, 2001).

1.4.2 Main nucleation parameters

The experimental results obtained by different researchers show that the behavior of hydrate nucleation is not governed by any common thermodynamic property but is rather stochastic (Sloan & Koh, 2008). Many parameters can influence the nucleation process. Driving force, induction time, agitation and memory effect are believed to affect the results of present MSc project and thus their description will be provided below.

Driving force for nucleation

As defined by Mullin (2001), nucleation rate is the number of nuclei formed per unit time per unit volume, which in turn is related to the driving force (Servio & Englezos, 2003). Even though various parameters have been reported to drive the nucleation process such as chemical potential, fugacity, degree of subcooling, supersaturation, etc., Christiansen and Sloan (1995) derived an expression that accounts for all driving forces discussed by other authors (Sloan & Koh, 2008). The general driving force for nucleation can be related to the total molar change in Gibbs free energy of hydrate formation, Δg^{exp}, expressed as

$$\Delta g^{exp} = \Delta g^{reactants} - \Delta g^{products} \quad (1.6)$$

where Δg^{exp} is a function of pressure, temperature, chemical potential and fugacity; the term $\Delta g^{reactants}$ represents gas and water that are converted to hydrate, whereas the term $\Delta g^{products}$ is related to hydrate.

The driving force for hydrate formation is often represented by the degree of subcooling, *ΔT*, which is defined as the temperature difference between the system's temperature, T_{sys}, and the triple equilibrium temperature of the methane-hydrate-water system under a given pressure, T_{eq}. Nevertheless, this parameter does not encompass the effect of pressure. Arjmandi et al. (2005) studied the effect of pressure on the driving force. They found out that for pure gas-water systems the driving force was proportional to the degree of subcooling at constant pressure and temperature conditions. Further, it was concluded that the degree of subcooling alone could represent the driving force in pure gas-water systems at pressures exceeding 200 bar.

In this master project, pure methane gas (>99.5%) was used and the system's temperature was approximately the same for the majority of experiments; therefore, the degree of subcooling is assumed to represent the driving force.

Induction time

Even though the system's pressure and temperature are within the hydrate stable region, the hydrates do not massively form for a certain period due to metastability. This period is called induction time which can be defined as the time elapsed from the establishment of hydrate stable conditions until the growth of detectable amount of hydrate (Kashchiev & Firoozabadi, 2003). Sloan and Koh (2008) summarizes some important features of the induction time as follows:

- Induction time is most likely to be dominated by nucleation stage, but is also affected by growth stage until hydrates are first detected.
- Induction time is stochastic, especially at low driving forces.
- The stochastic behavior is less pronounced at high driving forces and with constant cooling.

In addition, the induction time tends to depend on the accuracy of detection by means of apparatus. Flatlandsmo (2015) used similar experimental setup to that of this project to study the hydrate formation and dissociation on pore-level, and estimated that hydrate growth could be detected through a microscope only if the hydrate layer thickness exceeded 1.5 µm. Hence, the induction time in this thesis is likely to relate to the thickness of hydrate layer.

Memory effect

It is generally agreed that the hydrates keep a memory of their structure when they are decomposed at moderate temperatures. The gas hydrates are expected to nucleate more readily in a system that has earlier been dissociated, than in a system with renewed water with no previous hydrate history. This phenomenon is called the memory effect. This effect can be destroyed by sufficient heating of the system above the hydrate formation temperature at a given pressure. Based on the experimental observations of the memory effect, two opposing hypotheses are proposed to explain this phenomenon (Sloan & Koh, 2008):

1. Hydrate structure continues to exist in a system in the form of either residual structure of partial hydrate cages or persistent hydrate crystallites.
2. Dissolved gas resides in the solution after hydrate dissociation.

Despite numerous observations of the memory effect, there is no general agreement on this phenomenon due to lack of direct molecular studies to verify the above hypotheses. Although the

results of many experiments conclude that the memory effect seems to reduce the induction time, some other researchers have cast a doubt on the existence of memory effect (Rodger, 2000; Wilson & Haymet, 2010).

Two distinct types of hydrate formations were performed in this thesis: primary and secondary formation. Several definitions of primary and secondary formation arise in the literature. According to Mullin (2001), unlike primary formation, the secondary hydrate formation initiates under the presence of crystalline matter. In this thesis, secondary formation is undergone in a system that has previously been dissociated but has not been heated afterwards. Therefore, secondary formation performed in this work is believed to be affected by memory effect. In contrast, primary hydrate formation is unlikely to be affected by the memory effect since a system was heated and cleaned with water prior to every experimental run to remove any residual hydrate structures.

Agitation

High driving forces alone do not always induce nucleation and promote a further growth. Agitation (cavitation or turbulence) is frequently used to enhance nucleation. The degree of agitation tends to affect the induction time both in bulk systems and in synthetic porous media.

When it comes to the hydrate studies on pore-scale performed by other master students at the Reservoir Physics group, they all reported difficulties related to the hydrate formation in high-pressure micromodels under static conditions. Flatlandsmo (2015) and Iden (2017) emphasized the importance of agitation for hydrate formation. Their systems were rarely observed to nucleate spontaneously under static conditions and hence agitation was successfully forced into the micromodel to induce hydrate formation. The agitation technique similar to that applied by Iden (2017) was utilized in this work.

1.4.3 Hydrate growth

Once the critical cluster size is attained and the induction time is over, the stable hydrate growth initiates. Three main parameters influence the hydrate growth on the molecular level (Sloan & Koh, 2008): (1) the kinetics of crystal growth at the hydrate forming area, (2) mass transfer of molecules to the hydrate forming area, and (3) heat transfer of the exothermic heat released during hydrate formation away from the hydrate forming area. However, it has been suggested that heat and mass transport dominate the hydrate growth in multiphase systems, whereas the role of hydrate intrinsic kinetics can be less significant (Sloan & Koh, 2008). Many of the nucleation parameters also appear to influence the hydrate growth. In this thesis, the hydrate growth rates will be estimated as the quantification of hydrate growth may assist in a better understating of general phenomenon of hydrate formation.

General crystal growth mechanism

Cahn et al. (1964) distinguish between two main kinetic growth mechanisms: stepwise and continuous. In stepwise growth mechanism, the molecules attach at step kink sites and the solid interface grows by the lateral motion of steps. Continuous growth mechanism involves the molecular attachment everywhere on the surface and the continuous advance of the solid interface normal to itself. It is proposed that the driving force in terms of subcooling affects the kinetic mechanism by which the growth proceeds. The sufficiently low driving forces result in a step growth, whereas a continuous growth operates at sufficiently high driving forces.

The occurrence of a certain growth mechanism can be validated experimentally in terms of kinetics and morphology. For instance, the linear dependence of a growth rate on supercooling provides a strong evidence for a continuous mechanism. With regard to morphological features, the development

of well-defined crystallographic surfaces indicates a stepwise mechanism. However, the morphological evidence must be considered only when the heat transfer is not a limiting factor because heat flow restrictions will also result in a rounded crystal surface independent of the growth mechanism. Moreover, morphology developed during the active growth process differs from that of equilibrated crystal since the shape of the latter does not depend on the growth mechanism.

Figure 1.9 demonstrates the formation of methane hydrate crystals at the water-methane interface performed by Freer et al. (2001). The initial growth results in the well-defined crystals postulating the step mechanism (Figure 1.9a). As pressure increases, the mechanism shifts from step to continuous growth indicated by the disappearance of the facets and film roughening (Figure 1.9b).

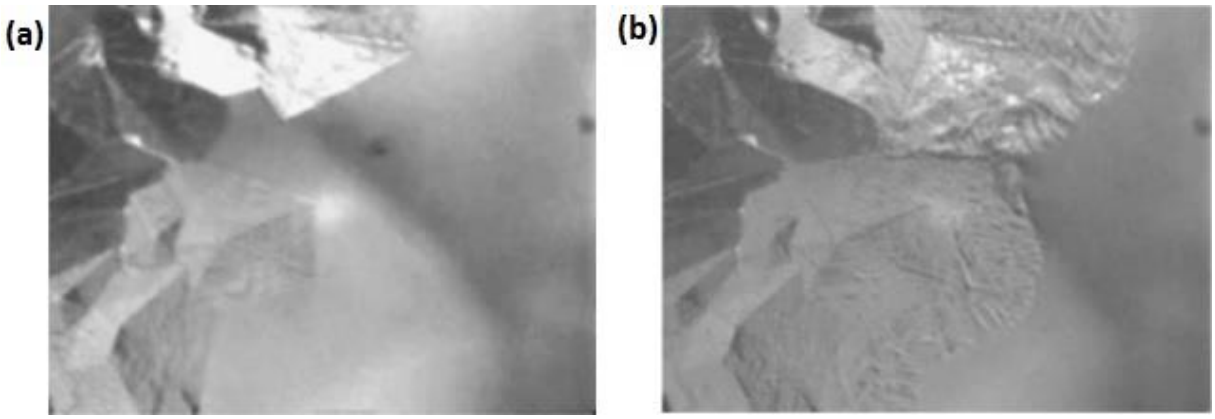

Figure 1.9. (a) The development of methane hydrate crystals at the water-methane interface; (b) the facets vanish and the film roughens upon pressure elevation postulating the transition from step to continuous growth (Freer et al., 2001).

Hydrate formation mechanism

The hydrate growth typically initiates at the water-hydrocarbon interface due to significantly higher hydrate component concentrations compared with mutual fluid solubilities (Sloan, 2003). Based on the experimental analysis of a hydrate films/shell development at the water-hydrocarbon interface performed by different authors, Sloan and Koh (2008) proposed the mechanism for hydrate formation according to the following steps (Figure 1.10):

1. Development of a thin porous hydrate film across the water-hydrocarbon interface.
2. Thickening of a porous hydrate film.
3. Transformation from porous to completely solid nonporous hydrate film.

The development of a hydrate film at the interface inhibits further growth due to mass transport limitations through the solid hydrate membrane (Sloan, 2003). Nevertheless, water and hydrate former should easily diffuse through the porous hydrate film (Staykova et al., 2003). Figure 1.11 shows a porous methane hydrate image obtained by a field emission scanning microscopy (Staykova et al., 2003).

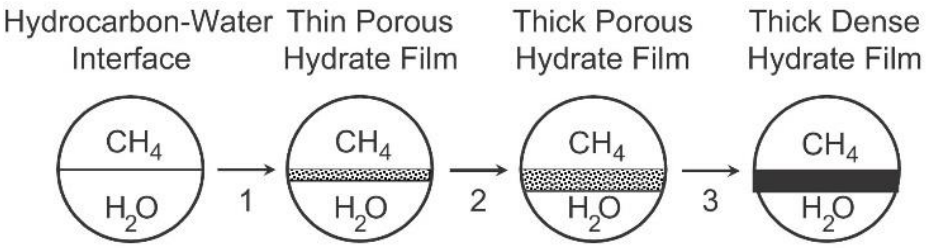

Figure 1.10. Schematic of the proposed mechanism for the development of a hydrate film at the water-hydrocarbon interface (Taylor et al., 2007). Step 1: Thin porous hydrate film develops across the water-hydrocarbon interface. Step 2: A porous hydrate film expands. Step 3: Conversion of porous to solid nonporous hydrate film.

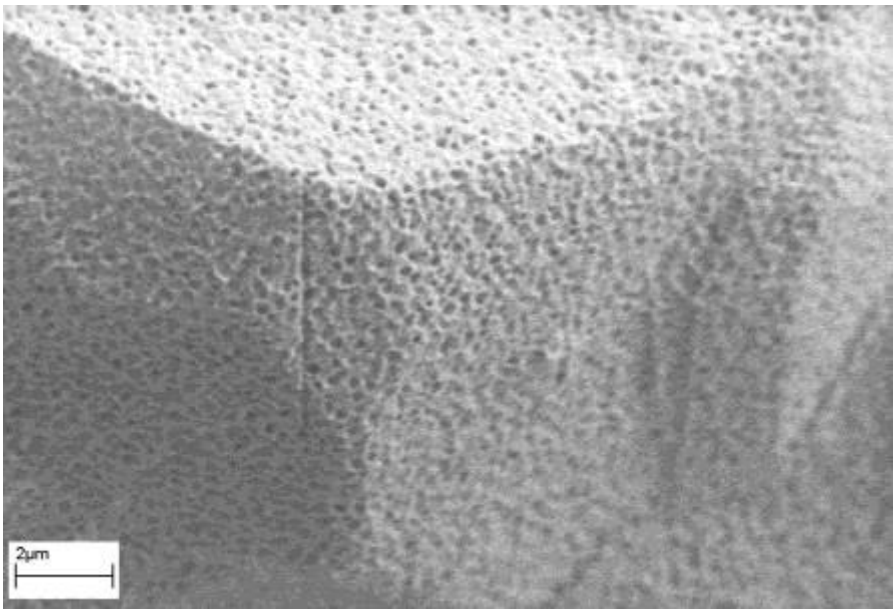

Figure 1.11. A field emission scanning electron microscopy image of a porous methane hydrate crystal (Staykova et al., 2003).

Crystal morphology

Several studies show that crystal morphology depends on the applied driving force and generally unaffected by hydrate former (Sloan & Koh, 2008). The development of faceted/columnar crystals is expected at low driving forces, whereas the crystal morphology transforms to rough needle-like dendritic form at high driving forces. Servio and Englezos (2003) suggest that the growth of dendritic crystals at high driving forces is due to a larger number nucleation sites compared to that at low driving forces. As discussed by Mullin (2001), the rate of nucleation is proportional to the degree of supersaturation, which in turn is proportional to the driving force (Servio & Englezos, 2003). Hence, at high driving force hydrate crystals are likely to grow at different locations with faster nucleation kinetics, thereby leading to more random crystal growth that in turn results in a rougher surface. In contrast, at low driving force hydrate nucleates at fewer nucleation sites, where the slower crystal growth occurs in a more regular manner.

Columnar/faceted and dendritic crystal morphologies have been observed in various hydrate systems depending on the applied driving force. Figure 1.14 illustrates columnar (Figure 1.14a) and dendritic hydrate crystals (Figure 1.14b) developed at the water-methane interface in bulk. Figure 1.12 shows the development of faceted (Figure 1.12a) and dendritic methane hydrate crystals (Figure 1.12b) in synthetic porous media. The formation of needle-like dendritic methane hydrate crystals covering the surface of water droplets is shown in Figure 1.13.

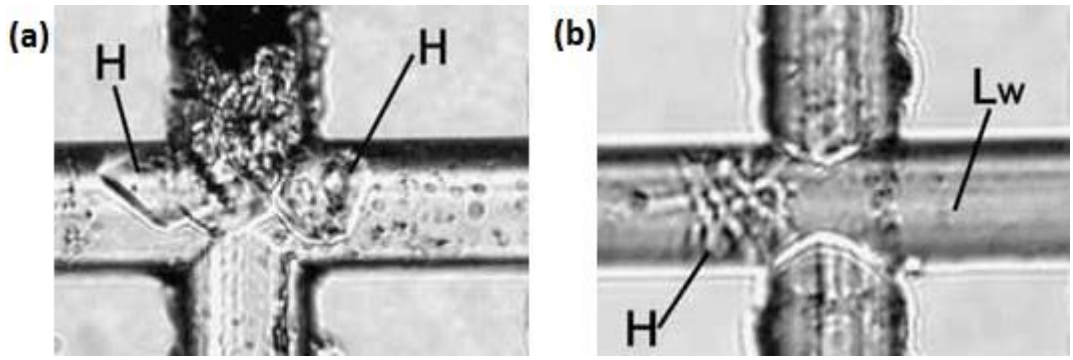

Figure 1.12. Different morphology of the methane hydrate crystals developed in synthetic porous media: (a) faceted crystals (symbol H), (b) dendritic crystals (symbol H) (Katsuki et al., 2007). L_w and H, the symbols in this figure, represent the liquid water and methane hydrate crystals.

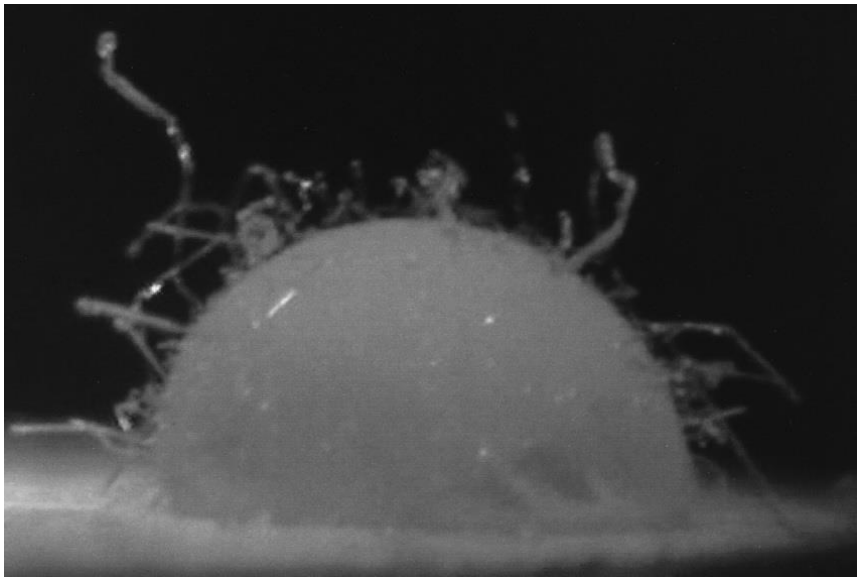

Figure 1.13. Needle-like dendritic crystals of methane hydrate covering the surface of water droplet (Servio & Englezos, 2003).

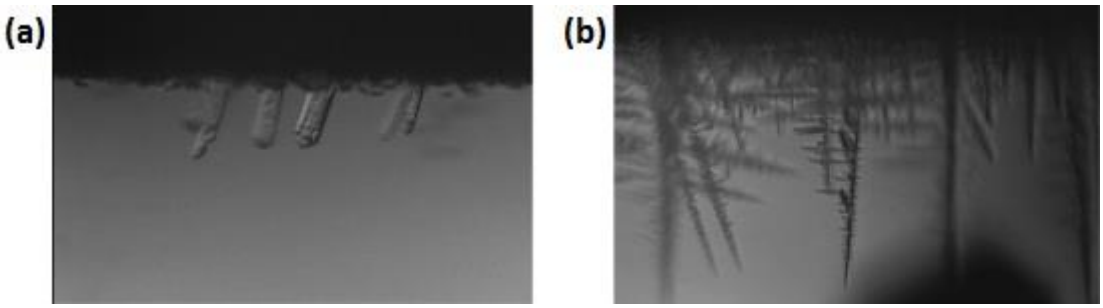

Figure 1.14. Different morphology of hydrate crystals developed at the interface between methane and water presaturated with methane in bulk: (a) columnar crystals at low driving forces, (b) dendritic crystals at high driving forces (Ohmura et al., 2005).

1.4.4 Hydrate formation in porous media

The hydrate nucleation and growth in porous media differ from those in bulk systems. In addition to parameters described in section 1.4.2, the hydrate formation in porous media is also affected by wettability, capillarity, pore sizes and fluid saturations. Nevertheless, the effect of pore sizes can be neglected at values exceeding 100 nm (Sloan & Koh, 2008). The thermodynamic properties in porous media are different from those in bulk due to two main reasons (Clennell et al., 1999):

1. Molecular interactions between the hydrophilic mineral surfaces and fluids.
2. Energy necessary to support capillary equilibrium.

In water-wet systems, a thin water film coats the grain surface (Figure 1.15a). Unlike pore water, this bound water does not participate in hydrate formation (Handa & Stupin, 1992). The interactions between grains and water reduce the activity of water where activity is defined as a chemical potential normalized to a reference state (Figure 1.15b). The capillary forces further reduce the water activity (Handa & Stupin, 1992). As a result of the combined effect of these factors, higher pressures or lower temperatures are needed to form hydrates in porous media compared to those in bulk systems, and therefore, experimental results obtained in bulk systems may not necessarily be correlated to porous systems (Handa & Stupin, 1992). However, capillary inhibition of hydrate formation in porous media can be counteracted by capillary supersaturation, i.e. an increased gas concentration in water due to equal chemical potentials of dissolved gas and free gas bubbles (Clennell et al., 1999). Capillary supersaturation can be achieved by additional gas supply, increased pressure or reduced temperature.

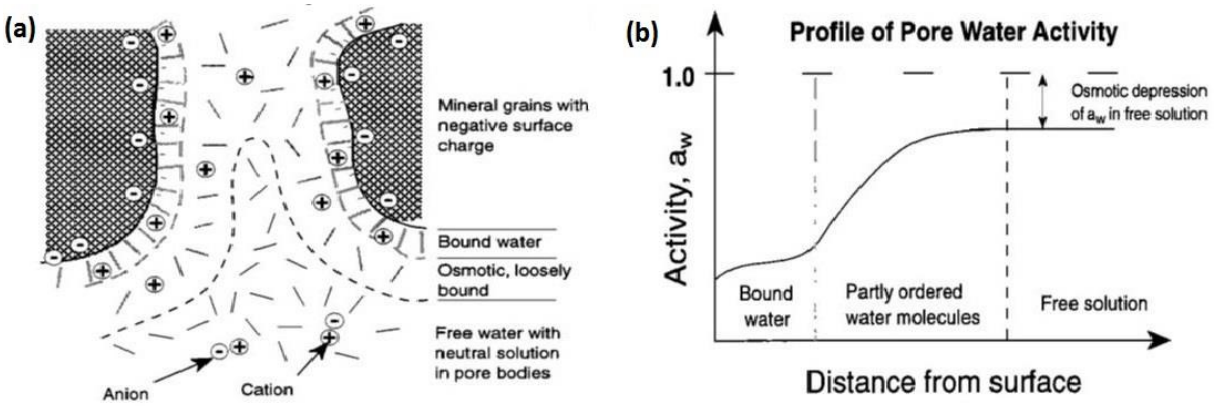

Figure 1.15. (a) Different water layers and grain surfaces in porous media. A thin water film coats the mineral surfaces and does not participate in hydrate formation. (b) Water activity as a function of distance from grain surface. Activity of bound water coating the grain surfaces is reduced (Clennell et al., 1999).

Hydrate distribution in the pore space

The hydrate pore occupancy is an important concern when evaluating the hydrate systems in nature. The distribution of gas hydrates is widely discussed in literature in relation to their ability to cement the grains. Several schemes of hydrate deposition can be found in literature. To avoid inconsistency, the cementing nature of gas hydrates is discussed here based on the model proposed by Ecker et al. (1998). They described two extreme schemes of the hydrate distribution within the pore space: (1) contact-cementing hydrates (or grain cementing), which reside on the rock grains; and (2) non-cementing hydrates (or pore filling), which occupy the pore space away from the grains (Figure 1.16). The grain cementing hydrates stiffen the sediments, whereas pore filling hydrates are unlikely to reinforce the grains. The grain cementation by hydrates can therefore have a great impact on the sediment stability and the interpretation of seismic data.

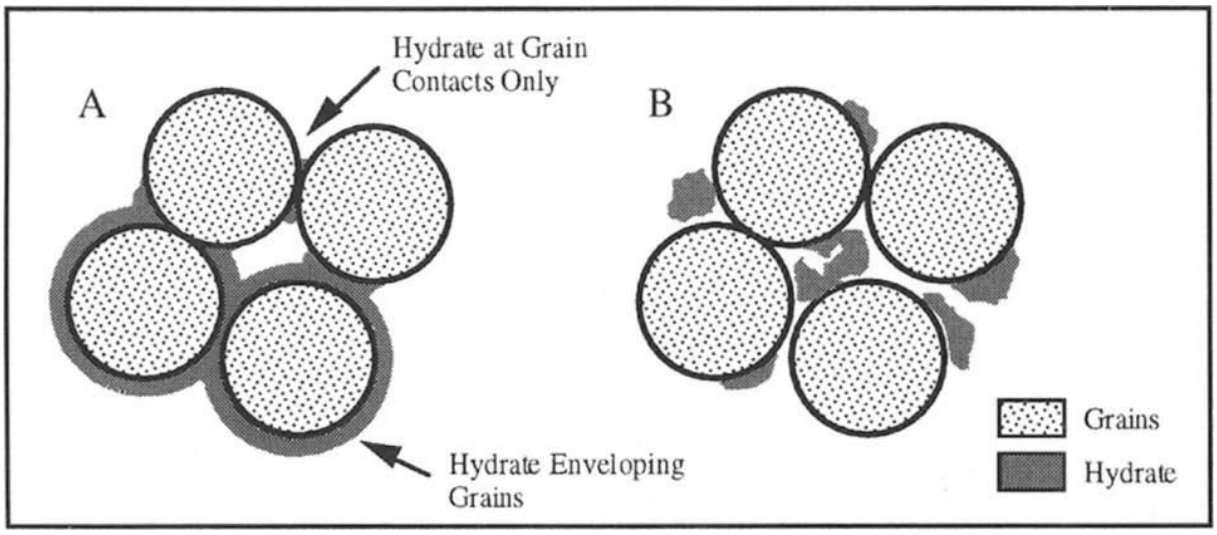

Figure 1.16. Two possible hydrate distributions within the pore space: (A) grain cementing hydrates and (B) pore filling hydrates (Ecker et al., 1998).

1.4.5 Hydrate dissociation

Hydrate dissociation is an endothermic process that incorporates heat and mass transfers together with intrinsic kinetics. However, many studies have shown that heat transfer predominantly governs the hydrate decomposition (Moridis et al., 2002; Hong et al., 2003; Davies et al., 2006). Hong et al. (2003) suggest the kinetics can dominate the early stages of dissociation. Nevertheless, the heat transfer controls the later stages due to the developed temperature gradient in the hydrate zone as a consequence of the decomposition process. The mass transfer can also influence the hydrate dissociation. The effect of fluid flow (water and gas) away from the hydrate interface becomes more pronounced on field scale, whereas the heat transfer and the kinetic dissociation of hydrates are the dominant factors on laboratory scale (Tang et al., 2007).

Almenningen et al. (2018) analyzed the heat transfer in a silicon micromodel and concluded that the heat transfer at the pore bottom and the pore corners (both are made of silicon wafer) was more favorable than at the glass plate on top of pores due to the difference in heat conductivity between the silicon wafer and the top glass plate. In this master thesis, the hydrate formation and dissociation occurs in a similar silicon micromodel and the heat transfer effects are assumed the same as described by Almenningen et al. (2018).

Self-preservation of natural gas hydrates

Many researchers have reported the natural gas hydrate ability to delay the dissociation by lowering the pressure below equilibrium under sub-zero temperatures (Sloan & Koh, 2008). This phenomenon is called anomalous self-preservation, which can have practical implications for natural gas storage where the prolonged gas hydrate stability is desired. Self-preservation of natural gas hydrates at $T < 0$ °C is likely due to ice shielding from the water released during the hydrate dissociation (Makogon & Ghassemi, 2010).

Makogon and Ghassemi (2010) studied the effect of self-preservation in porous media at temperatures above 0 °C. They determined that the fresh water-methane hydrate dissociation temperature increased by several degrees compared with theoretical values. This was explained by the capillary pressure increase due to alterations of the pore size and structure as a result of hydrate formation in porous media. The effect of natural gas hydrate self-preservation in porous media results in a greater amount of energy needed to dissociate the hydrates in sediments. In this work, the effect of self-

preservation was believed to cause the delayed hydrate dissociation observed in one of the experiments.

1.4.6 Production techniques

Various production techniques are proposed to produce natural gas from hydrates. The most common means are depressurization, thermal stimulation and inhibitor injection (Makogon, 1997). Although gas from hydrates can be extracted using one of the mentioned methods only, the combination of various techniques is often applied on a long-term (Moridis et al., 2011). Figure 1.17 illustrates the effect of various production techniques on the pressure-temperature conditions and the gas-hydrate-water stability curve. In this master project, the hydrates are dissociated through pressure reduction.

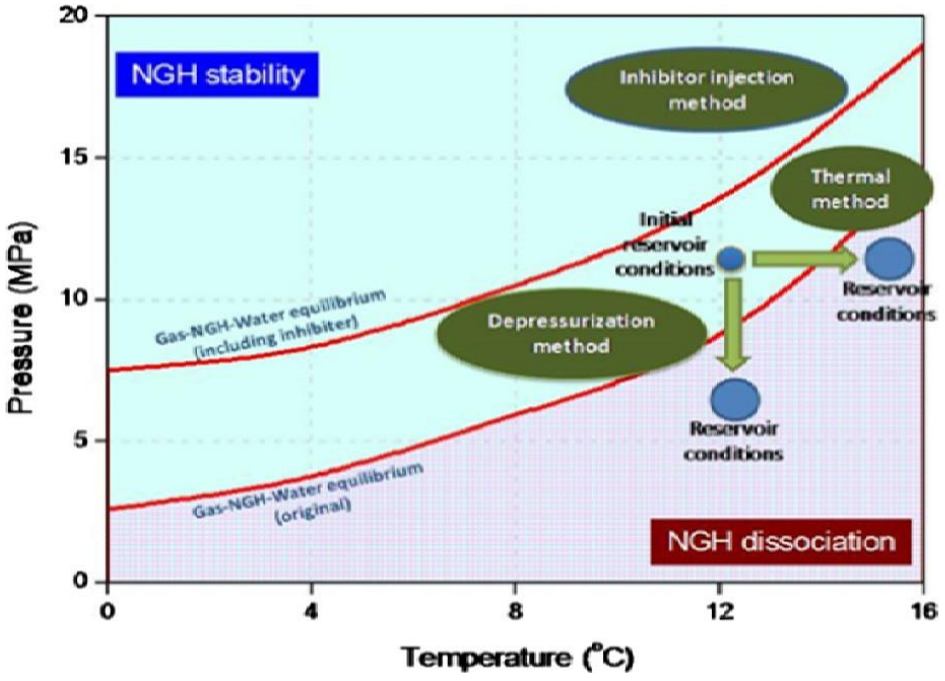

Figure 1.17. Schematic of different production techniques (Li et al., 2016). Inhibitor injection technique alters the gas-hydrate-water equilibrium line, whereas depressurization and thermal stimulation change the pressure-temperature reservoir conditions. NGH stands for natural gas hydrate.

Depressurization

The hydrates can be decomposed by reducing the pressure below the equilibrium value at a given temperature. Due to endothermic nature of the hydrate dissociation, the gas production by depressurization will result in a continuous temperature decrease in a hydrate decomposing area. Once the local temperature drops to the equilibrium value at a given pressure, further dissociation might terminate. Hence, the sufficient heat must be supplied from surroundings to promote further dissociation (Sloan & Koh, 2008). Among the three common methods of gas production from hydrates, depressurization is the most cost-efficient (Sloan & Koh, 2008).

Thermal stimulation

The thermal stimulation technique involves the temperature rise above the equilibrium value at a given pressure. This can be performed by hot water/steam injection or by direct heating of the formation. The thermal stimulation method can compensate for drawbacks of the depressurization technique such as the heat loss, the low gas production rate, the hydrate reformation or ice formation, and the blocking effect (Song et al., 2015). However, this production technique is relatively slow and requires an intensive amount of energy (Ruppel, 2011).

Inhibitor injection

The injection of chemicals such as methanol and ethanol glycol inhibits the gas hydrate stability at local pressure and temperature conditions by shifting the hydrate equilibrium line to higher pressures and low temperatures. Although the inhibitor injection promotes a relatively fast dissociation, the efficiency of this production technique depends on diffusion and effective permeability to solution in the reservoirs (Li et al., 2016). The chemical injection is not considered as the primary technique to produce gas from hydrates for a prolonged production period or on a large scale (Ruppel, 2011).

2 Literature survey

This literature overview summarizes previous research on gas hydrates relevant to this master thesis. Since the main intention of this work is to study the methane hydrate phase transitions in the silicon micromodel, the focus of this chapter is kept on the pore-level hydrate formation and dissociation patterns in micromodels (sections 2.1-2.2). The quantification of the hydrate growth is an important part of this MSc project. Section 2.3 addresses the hydrate growth rate in bulk and synthetic porous media. In addition, the effects of the water saturation and pore size of the porous media are included in section 2.4.

2.1 Hydrate formation in micromodels

The first attempt to visually observe gas hydrate formation and dissociation at the microscopic scale in synthetic porous media (glass micromodel) was performed by Tohidi et al. (2001). They studied the hydrate formation from soluble hydrate former (tetrahydrofuran), free gas (methane), and dissolved gas (carbon dioxide). The experiments provided the visual evidence that hydrates could also develop from phases dissolved in water (carbon dioxide), without the presence of a free-gas phase. Independent of the system studied, the hydrates accumulated in the center of the pore, whereas water films coated the grain surfaces. This phenomenon likely restricts the potential for sediment cementation, which was only observed in the regions where the gas hydrate occupied a significant part of the pore space or the grain size was small. The hydrates formed from tetrahydrofuran initially grew as curved crystal faces, but then transformed into hexagonal shapes with angular margins. The skeletal shapes were observed to develop in hydrates formed from dissolved carbon dioxide. For methane-water system, hydrate grew first at the water-gas interface, resulting in the formation of a hydrate layer around the gas bubble, which was then totally converted to hydrate (Figure 2.1b). In addition, the hydrate formation was also observed in isolated gas bubbles, likely due to the movement of small seed nuclei and/or the alteration in the structure of the surrounding water. After crystallization, the hydrates redistributed over time (Figure 2.1c).

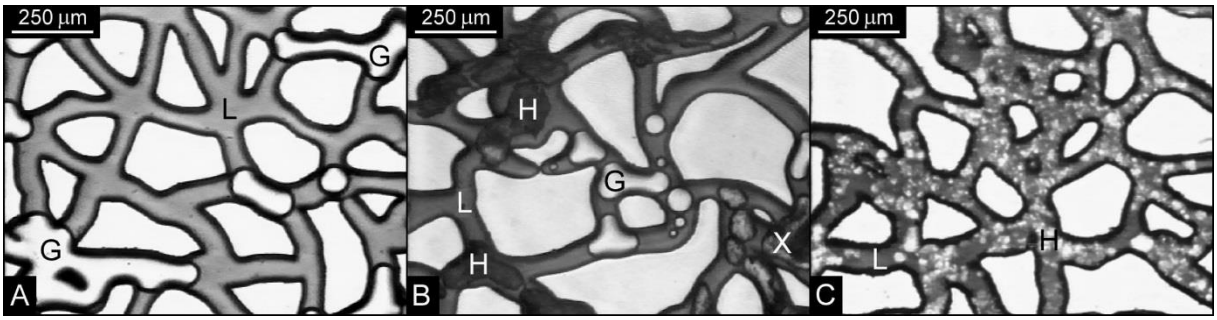

Figure 2.1. Methane hydrate formation in synthetic porous media (Tohidi et al., 2001): (a) Water (L) and methane (G) prior to hydrate formation, (b) newly formed hydrates (H) and a thin hydrate layer encapsulating the gas bubbles (X) prior to total conversion to hydrate, (c) hydrate redistribution over time.

Katsuki et al. (2007) studied the effect of the system subcooling on the methane hydrate growth in a glass micromodel. Four different system subcoolings were studied, $\Delta T = 3.4$ K, 6.7 K, 12.3 K, and 14.1 K. The continuous growth of the faceted crystals, which bridged the channels, was observed when the system subcooling was equal or lower than 6.7 K. Physical bonding that generated between the faceted hydrate crystals and the glass walls of the porous media was likely because insufficient resolution failed to detect thin water films along the grains. At the system subcooling equal or greater than 12.3 K, they initially observed the development of the dendritic hydrate crystals, which then transformed into particulate hydrate systems. No channel bridging was observed. The absence of a sufficient amount of an additional methane supply likely restricted the bridging possibility. The magnitude of the mass

transfer of methane molecules through liquid water was the key mechanism affecting the morphology of the hydrate crystals.

Hauge et al. (2016) studied the formation of the methane and carbon dioxide hydrates in high-pressure silicon micromodel. They concluded that the fluid connectivity and local fluid distribution were the main factors affecting the hydrate growth pattern. The hydrate growth in the gas-filled pores progressed in three different steps:

1. The thin-film hydrate growth on the water-gas interfaces.
2. The thicker-layer hydrate growth along the pore walls and towards the pore center.
3. The hydrate redistribution over time.

In carbon dioxide-water system, the initial hydrate growth was observed in the gas-filled pores. Even though the hydrate also formed from the isolated gas bubbles, further hydrate growth was terminated due to limited mass transfer caused by the hydrate layer on the interface between carbon dioxide and water (Kvamme et al., 2007). The growth of carbon-dioxide hydrate was also observed in water-filled pores if they were adjacent to the hydrate-filled pore. The methane hydrate initially had the coarse texture, which then became more transparent after the hydrate redistribution. The methane hydrate did not grow in the water-filled pores, unless water was partially displaced by free gas. Lower methane solubility compared with carbon dioxide likely inhibited the methane hydrate formation in the water-filled pores.

2.2 Hydrate dissociation in micromodels

Tohidi et al. (2001) studied the hydrate dissociation by means of thermal stimulation at the microscopic scale in synthetic porous media. Three different hydrate systems were studied – tetrahydrofuran-water, free methane gas-water, and dissolved in water carbon dioxide-water systems. They observed the complete redistribution of the fluids, independent of the system studied. Initially, the dissociation of tetrahydrofuran hydrates led to a slurry of fine crystals. The system was then returned to liquid only. In methane-water system, the areas covered by hydrate reduced in size, leading to the separation of hydrate sections. As a result, these sections started to move within the liquid. The gas bubbles were then released from hydrates and spread over the model. Moreover, small crystalline structures remained in the liquid even at temperatures beyond the hydrate stability region, likely due to anomalous preservation of methane hydrate. The hydrates formed from dissolved carbon dioxide dissociated completely, without a sign of any crystalline structures left. The system returned to its original single-liquid state. No gas bubbles were observed until pressure was lowered below 0.69 MPa at room temperature.

Katsuki et al. (2008) dissociated methane hydrate in a glass micromodel by temperature increase and pressure reduction. They observed that methane gas released from dissociating hydrate formed vapor slugs that completely filled the pore space. No formation or growth of vapor methane phase on the hydrate crystal surface was observed. The dissociation due to temperature increase was initially associated with the formation of microscale methane bubbles on a hydrate crystal surface, which then diffused through liquid water to a larger bubble or methane gas slug. Upon pressure reduction, the small methane bubbles initially developed in liquid water. These bubbles grew in size and transformed into larger slugs, which then flowed in pore channels (Figure 2.2).

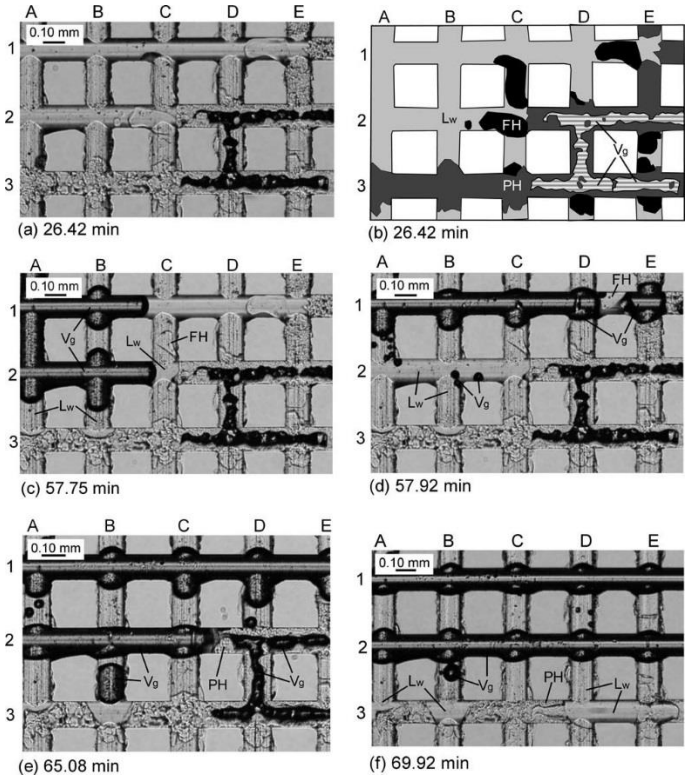

Figure 2.2. Dissociation of methane hydrate by depressurization (Katsuki et al., 2008). The geometries in (a) are illustrated in (b) as faceted hydrate crystals (FH), particulate hydrate crystals (PH), gaseous methane (Vg), and liquid water (Lw).

Almenningen et al. (2018) studied the dissociation of methane hydrate developed from distilled and saline water using high-pressure silicon micromodel. They utilized two distinct dissociation methods – depressurization and thermal stimulation. For a distilled water system, dissociation pattern induced by pressure reduction was affected by initial pore occupancy. When a pore was completely filled with a solid hydrate without enclosed gas, the hydrate dissociation initiated in the pore corners first. This was explained by the transmission of pressure reduction through wetting water films coating the grains in the pore corners. In pores occupied by a hydrate films/shell with enclosed gas, the pressure reduction was transferred through the enclosed gas phase, resulting in a dissociation pattern from the pore center towards the pore wall. During thermal stimulation, the hydrates first dissociated in the pore corners and then towards the pore center, likely due to the difference in heat conductivity between the silicon wafer pore walls and the top glass plate. For a saline water system, water freshening during dissociation resulted in distinct dissociation patterns. Local hydrate reformation was observed.

2.3 Hydrocarbon hydrate growth rate

The hydrate growth has been extensively studied in bulk systems. Bulk systems and porous media have distinct thermodynamic properties (Clennell et al., 1999), and therefore hydrate formation mechanisms in bulk may not be directly applicable to porous systems. One of the objectives of this thesis is to quantify the growth of methane hydrate on pore-scale and to compare the obtained results with those measured in bulk volumes.

2.3.1 Hydrate growth rate in bulk

Freer et al. (2001) measured the lateral growth rate of the methane hydrate film along the planar water-methane interface in bulk system (high-pressure cell) over a wide range of pressures (3.55-9.06 MPa) and temperatures (1.0-4.0 °C), using optical microscopy. They found out that the growth rate was linearly dependent on the bulk temperature at constant equilibrium temperatures postulating a

continuous growth mechanism. However, the growth rate as a function of equilibrium temperature at constant bulk temperatures did not show a linear trend, suggesting that a unique growth rate may not exist for a given driving force.

Taylor et al. (2007) studied the film thickness and the propagation rate at the planar water-hydrocarbon interface for cyclopentane and methane hydrates in bulk (high-pressure cell) over the pressure range of atmospheric to 8.3 MPa and temperature range of 260-273 K, using video microscopy combined with gas consumption measurements. They demonstrated that the film thickness increased with time and subcooling, independent of hydrate former. The growth rate of methane hydrate along the water-methane interface increased with degree of subcooling, represented by a power law trend. Film thickening was observed to be much slower that the lateral growth. The obtained results showed a reasonable agreement with the growth rates measured by Freer et al. (2001). The film growth in the water phase was also observed, suggesting that the film thickness and growth rate were mass-transfer dependent, expressed in terms of the hydrate-former solubility in the water phase. Figure 2.3 illustrates the hydrate growth at the planar water-gas interface.

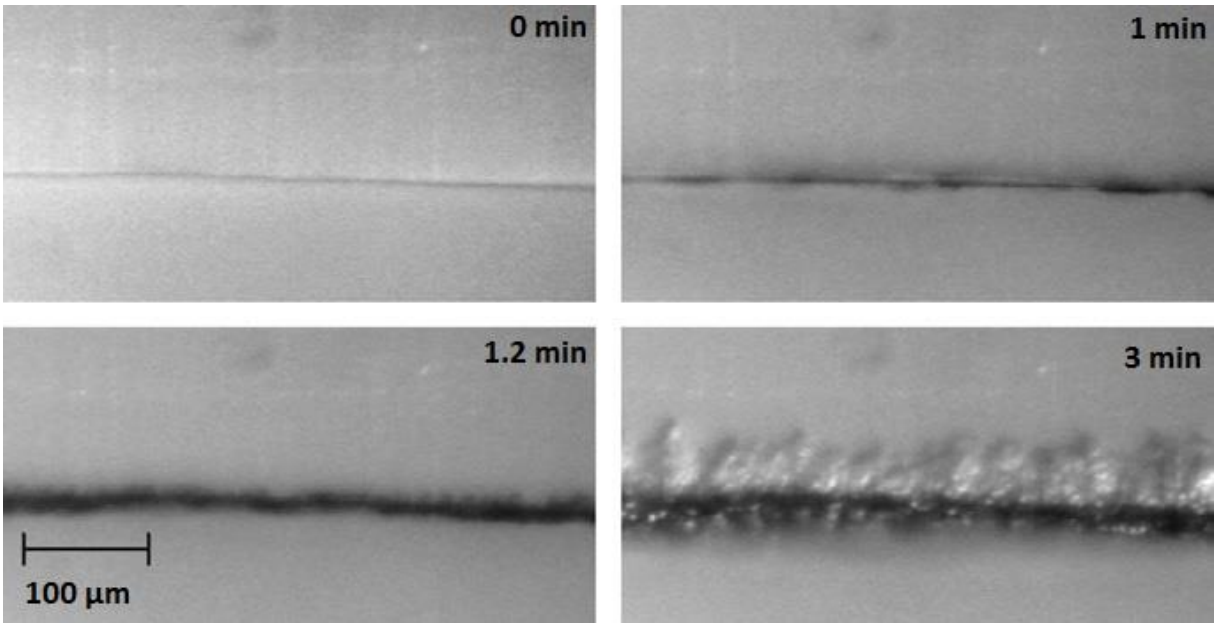

Figure 2.3. Methane hydrate film growth at the planar water-gas interface (Taylor et al., 2007). Methane is above the interface and water is below.

Besides a hydrate growth on a planar interface, the studies of growth rates in bulk volumes were also extended to a curved water-hydrocarbon interface using both pure-gas and mixed-gas hydrate formers. Peng et al. (2007) investigated the hydrate film growth on the surface of a gas bubble suspended in water. Tanaka et al. (2009), Saito et al. (2010) and Wu et al. (2013) examined the hydrate growth on the surface of a water droplet exposed to a gas phase (Figure 2.4). They all found out that the growth rates increased with increasing degree of subcooling.

The growth rates measured by Peng et al. (2007), Tanaka et al. (2009), Saito et al. (2010) and Wu et al. (2013) were consistent with those of Freer et al. (2001) and Taylor et al. (2007). However, the values for gas-mixtures hydrates were slightly lower compared with pure gas hydrates. Figure 2.5 provides a comparison between the growth rates obtained by Freer et al. (2001), Tanaka et al. (2009) and Saito et al. (2010).

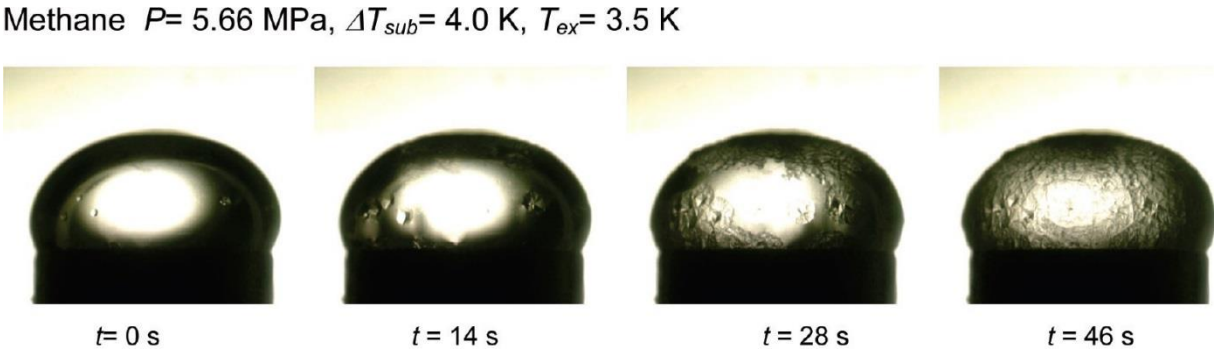

Figure 2.4. The growth of methane hydrate on the surface of the water droplet exposed to methane gas (Tanaka et al., 2009).

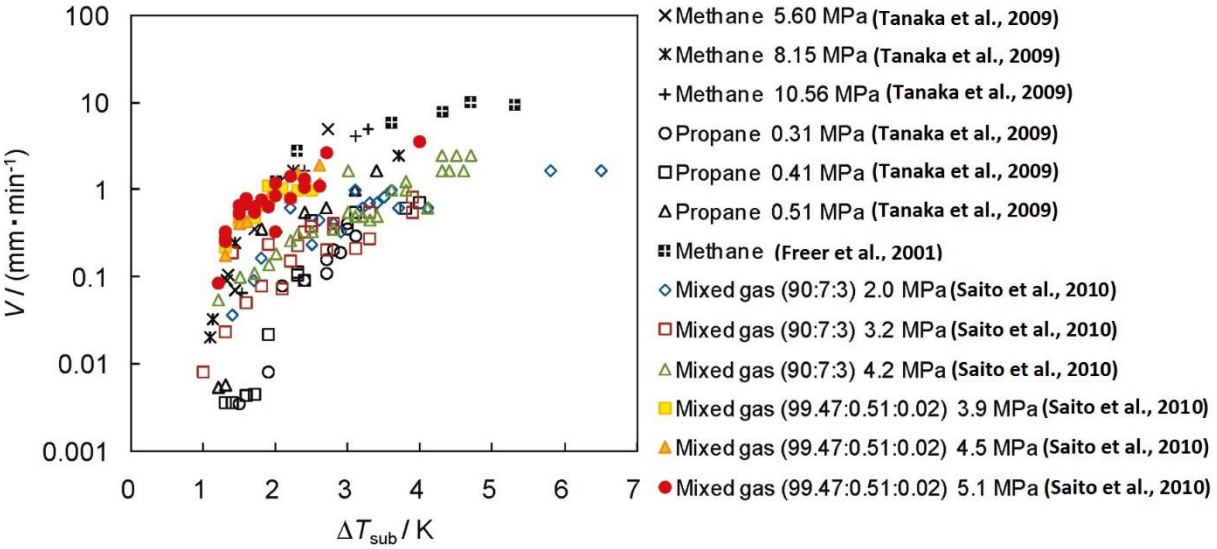

Figure 2.5. Comparison of the hydrate growth rates at the water-gas interface in bulk (Saito et al., 2010).

2.3.2 Hydrate growth rate on pore-scale

Hauge et al. (2016) were first to place emphasis on the hydrate film growth rate in porous media on micro-scale, using high-pressure silicon micromodel. They quantified the growth rate of the secondary methane hydrate formation at 8 MPa and 4.4 °C. The growth rate along the pore wall was estimated to be ~ 500 µm/s at T = 4.4◦C, which was consistent with the film growth rates reported by Freer et al. (2001). In contrast, hydrate growth towards the pore center was much slower, 6.9 µm/s. The difference in growth rates was attributed to the cross-sectional shape of the etched pores. The water-wet nature of porous media and the pore shape provided a sufficient water availability along the pore walls, which resulted in relatively high growth rate. On the other hand, hydrate growth towards the pore center was governed by a slow water transfer from pore corners and adjacent water-filled pores along the wetting films. One of the main objectives of this master thesis is to extend the studies of the methane hydrate growth rates in high-pressure silicon micromodels performed by Hauge et al. (2016).

2.4 Effect of water saturation and pore size on hydrate formation

Kang et al. (2009) studied the effect of driving force and pore size on the methane and carbon dioxide hydrates in silica gel pores, with pore sizes of 6, 30 and 100 nm. They found that the rate of hydrate formation expressed in terms of gas consumption over time was closely related to driving force; and that carbon dioxide hydrate formed faster than methane hydrate. The pore sizes did not affect the hydrate formation rate.

Kumar et al. (2010) formed carbon dioxide hydrate at various initial water saturations in a synthetic porous medium made of packed glass beads. It was discovered that at initial water saturations exceeding 35%, the hydrates demonstrated a pore-filling tendency, whereas the hydrate formation on the grain surface was observed at water saturation less than 35%. Fitzgerald et al. (2014) investigated the methane hydrate formation in the porous media at different water saturations using a glass bead sample pack. They determined that the initial hydrate formation rate expressed in mol/s increased with decreasing initial water saturations.

3 Methodology

This chapter describes how the raw data was acquired and analyzed. Section 3.1 emphasizes the experimental procedures for the hydrate formation and dissociation as well as the main characteristics of the silicon micromodel. Section 3.2 focuses on the optic features of the micromodel. The procedures for quantitative characterization of the visual images are provided in section 3.3.

3.1 Experimental part

All experiments were carried out in the micro-laboratory at the Department of Physics and Technology at the University of Bergen. The experimental setup was adapted from the previous work performed by master and PhD students at the Reservoir Physics group. The overview of experimental apparatus and fluids is provided below.

Apparatus:

- High-pressure micromodel
- Quizix Q5200 Pump system
- Aluminium holder
- 1/16”PEEK (polyetheretherketone) and 1/8” steel tubing
- Dual cooling chamber
- Thermo Scientific Neslab RTE 17 refrigerated bath circulator
- Propylene glycol based antifreeze by Camco
- HH506RA Omega Multilogger thermocouple
- Nikon SMZ1500 microscope
- Photonic LED F1 Cold light 5500K light source
- Nikon D7100 camera

Experimental fluids:

- Distilled water
- Methane gas from YaraPraxair with ≥ 99.5% purity

3.1.1 Micromodel properties

Hydrate formation and dissociation was studied in synthetic porous medium by means of a micromodel capable of withstanding pressures up to 150 bar. The bottom part of the model is made of a silicon wafer, which is anodically bonded to a borosilicate glass on top. The porous network is etched on the silicon wafer by a DRIE (Deep Reactive Ionic Etching) technique that ensures a realistic representation of geometrical and topological rock properties such as sharp corners, rough pore walls, high aspect ratio (i.e. ratio of pore body to pore throat). The porous medium is based on thin sections of Berea sandstone, with an average pore diameter in the order of 100 µm and dimensions 2.8 cm x 2.2 cm x 0.0025 cm. The micromodel has a water-wet nature as a result of manufacturing procedure. Four holes (ports) are drilled on the backside of the silicon wafer, providing an external access to the micromodel. Two high-permeable channels between the ports allow fluid transport through the porous network (Figure 3.1). Hornbrook et al. (1991) and Buchgraber et al. (2012) provide a detailed description of the manufacturing procedure.

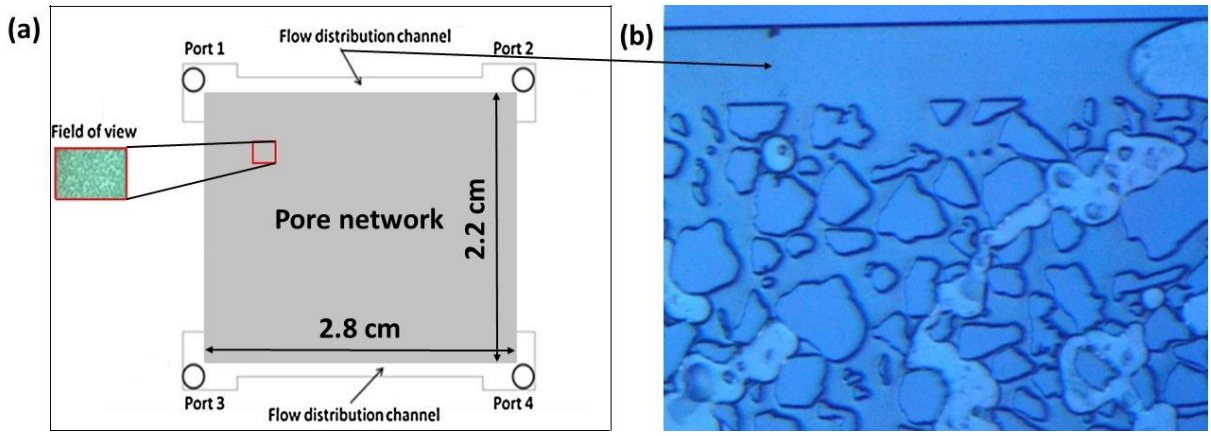

Figure 3.1. Schematic representation of the micromodel with etched pore network, two distribution channels and four ports. Field of view refers to the area visualized by the microscope that is around 1% of the entire model area (Modified from Hauge et al., 2016). (b) Microscopic view of the pore network and distribution channel occupied by fluids.

3.1.2 Experimental design

Figure 3.2 demonstrates a schematic of the experimental setup utilized in this work. The setup was adapted from the previous work performed by master and PhD students at the Reservoir Physics group.

The micromodel was carefully assembled an aluminum holder which was then placed in a dual cooling chamber. The outer part of the cooling chamber was filled with circulating cooling liquid (water and antifreeze) to maintain a constant temperature, whereas the inner part was filled with stagnant distilled water to minimize the disturbance around the micromodel. Two parts of the chamber were separated by an aluminum barrier, which ensured efficient heat transfer between them. The cooling chamber was covered by a lid to prevent any disturbance from the surroundings.

Quizix Q5200 pump system consisted of two separate pump cylinders operating independently of each other. Each cylinder was filled with a distinct fluid (distilled water and methane gas), which were injected to the micromodel in order to saturate the porous media and pressurize the system to a target pressure. Two operating modes were utilized: constant volumetric flow rate mode (to inject and reinject the fluids) and constant pressure mode (to maintain a constant pressure). The communication between the micromodel and the pump system was established through PEEK and steel tubing. Two cylinders were connected in two opposite ports of the micromodel to create a diagonal flow through the porous media (port 3 for water and port 2 for gas, Figure 3.1). This set-up of flow lines ensured even distribution of fluids in the model. Two other ports remained unconnected to any pumps, with port 1 being used to induce agitation in the system.

A refrigerated bath circulator filled with water and antifreeze was connected to the cooling chamber to provide a controlled cooling of the system. The temperature was monitored by a thermocouple placed in the still water directly beneath the micromodel. Flatlandsmo (2015) utilized similar experimental setup and briefly evaluated the heat transfer through the model with a general conclusion that the temperature in the still water and micromodel could be assumed equal. A microscope connected to a camera provided a direct visual observation of the hydrate behavior by means of images or videos. The camera was further connected to a computer screen, thereby providing an improved life-view monitoring of the micromodel. The observed area in the model (field of view) was illuminated by a cold light source.

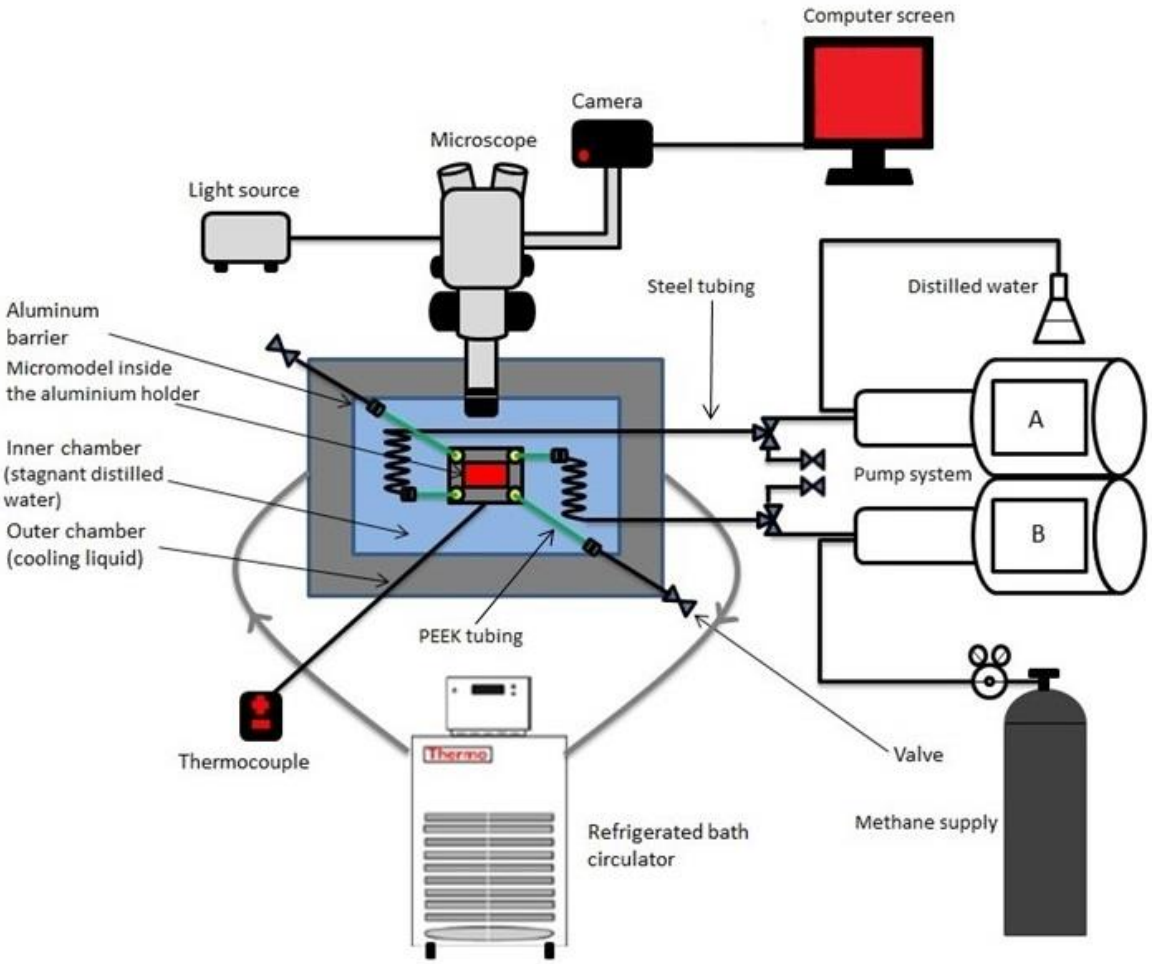

Figure 3.2. Experimental setup (Modified from Iden, 2017).

3.1.3 Experimental procedures

This section provides a brief description of the procedures for methane hydrate formation and dissociation.

Primary hydrate formation procedure

Two different types of hydrate formation procedures were used in this work; one for primary and one for secondary hydrate formations. The following procedure was implemented to perform primary methane hydrate formation:

1. Cylinder A and cylinder B were filled with distilled water and methane gas respectively.
2. The cylinder filled with methane gas was pressurized to the experimental pressure.
3. The flow connections and micromodel were flushed with distilled water to remove gaseous methane and any residual hydrate structures from the system.
4. The entire micromodel was carefully studied to visually confirm 100% water saturation.
5. Three outlet valves from the micromodel were closed, whereas the valve connecting the model and water cylinder remained open.
6. The system was carefully pressurized with water by 10 bar pressure increments to the experimental pressure, which was maintained constant for 24 hours to identify any possible leakages from the model.
7. The valve connecting the gas cylinder and the micromodel was opened.

8. Methane was injected into the micromodel at constant volumetric flow rates until the target fluid saturation in porous media was reached.
9. One of the pump cylinders (usually cylinder A) was stopped, whereas another pump cylinder was set to constant pressure operation mode to maintain the pressure in the model.
10. The refrigerated bath circulator was turned on to cool down the system to a target temperature.
11. The camera was set to automatic interval shooting (produces images) to monitor the fluid behavior in the micromodel.
12. In case of no visible hydrate formation under static conditions within 48 hours, the system was agitated by quickly opening and closing one of the valves connecting the micromodel to atmospheric conditions.
13. The camera settings were switched to video recording, which enabled to continuously monitor the fluid behavior in the micromodel.
14. Agitation resulted in the redistribution of fluids, which in turn caused the hydrate formation within several minutes.

Hydrate dissociation procedure

The primary hydrate formation has typically lasted for 24-48 hours until no visible changes in the hydrate structures were observed. The system was then depressurized to induce the hydrate dissociation in the following way:

1. One of the pump cylinders was retracted at constant volumetric rates, which ensured a controlled pressure reduction in the system. The hydrate behavior was monitored through video recording.
2. Once the system's pressure was lowered several bars below the equilibrium value at a given temperature, the pump cylinder was set a constant pressure operation mode.
3. The hydrate dissociation was monitored until no hydrate structures were visually detected in the micromodel.

Once methane hydrate has completely dissociated, both cylinders were depressurized to atmospheric conditions and the refrigerated bath circulator was turned off, enabling the system to equilibrate with room temperature. The distilled water was removed from the inner part of the cooling chamber. The system was then ready for a new primary hydrate formation.

Secondary hydrate formation procedure

Instead of increasing the system's temperature to room conditions after hydrate dissociation was finished, the micromodel could be re-pressurized to induce secondary hydrate formation. The formation procedure was similar to that of primary formation. The only difference was that the system was pressurized by fluid injection (mostly water) at constant volumetric flow rates until the hydrate formation was visually observed. The injection of fluid could then be either stopped or continued in order to provide an additional fluid supply to the model. Once the target pressure was established in the system, the pump cylinder was switched to a constant pressure operation.

3.2 Optic features

The raw data in this work was acquired through two-dimensional visual investigation of the silicon micromodel. A detailed discussion of the optic properties and limitations of the raw images is required for correct interpretation of the qualitative data.

3.2.1 Microscopic view

This thesis investigates the hydrate behavior in the micromodel illuminated by the light source. Understanding the light propagation through the micromodel is therefore essential when interpreting raw image data obtained in this work. Different media are present in the micromodel. They are illustrated in Figure 3.3 as methane gas (G), distilled water (W), hydrate films/shell with encapsulated gaseous methane (HF), crystalline hydrate without encapsulated gas (H), and rock grains (R).

The fluids can be distinguished under microscopic view based on the difference in refractive index (describes how the light propagates though a medium) and the wettability of the micromodel. Since the porous network has a water-wet nature, methane gas develops a convex curvature toward the water phase and the grains, enabling the observer to distinguish between the gaseous phase from water (Figure 3.3a).

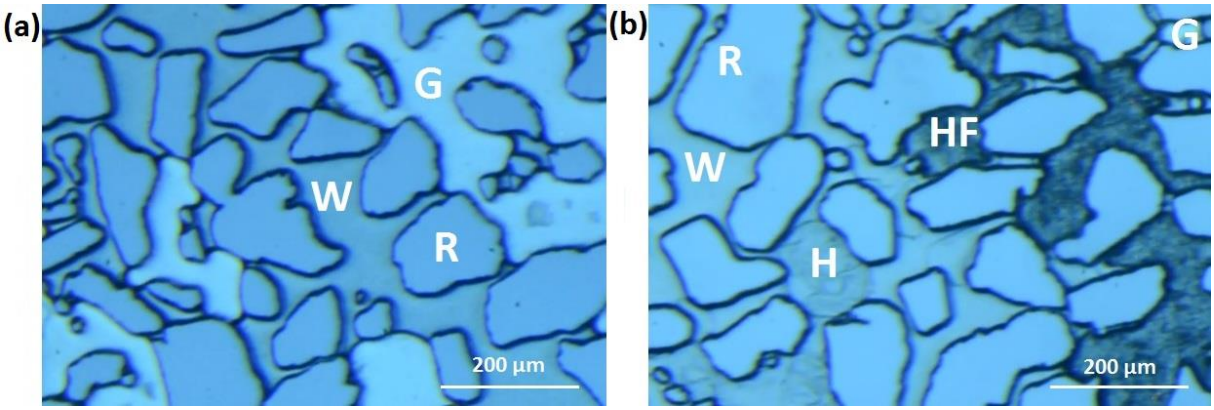

Figure 3.3. Microscopic view of the micromodel: (a) water (W), methane gas (G) and grains (R) prior to hydrate formation. (b) The micromodel after hydrate formation with two different hydrate configurations: hydrate films/shell (HF) appear black, whereas crystalline hydrate (H) is transparent.

In this thesis, the hydrate growth resulted in two different configurations of hydrate within a single pore space: (1) hydrate films/shell enclosing the methane gas and (2) crystalline hydrate in the entire pore depth. Almenningen et al. (2017b) performed a color analysis to distinguish between two different hydrate configurations, based on the fact that two non-absorbing materials cannot be visually distinguished when they have similar refractive indices (Bylov & Rasmussen, 1997). Insignificant difference in refractive indices between water [$n_{water} = 1.333$ (The Engineering ToolBox, n.d.; *a*)] and methane hydrate [$n_{hydrate} = 1.346$ (Bylov & Rasmussen, 1997)] results in no/little light reflection at the interface between the fluids. Almost all the light propagates through both phases and is reflected to the microscope by silicon wafer at the bottom of the micromodel. This causes the crystalline hydrate to appear transparent under microscopic view. On the other hand, the difference in refractive indices between methane gas and methane hydrate is significant [$n_{methane} = 1.000$ (The Engineering ToolBox, n.d.; *a*)]. Therefore, the presence of methane gas below/under the hydrate films/shell causes the light to be bent and reflected at the phase boundary between the fluids. Only a small amount of light will return to the microscope, thereby resulting in the darker appearance of the hydrate films/shell (Figure 3.3b).

3.2.2 Image quality

The images presented in this work might be of different color and brightness. The quality of images was affected by several factors such as camera settings, microscope magnification, internal and external light sources, and angle between the microscope lens and the micromodel.

The raw data was obtained by either microscopic images generated through interval timer shooting or by video recording. These two sources of raw data had different camera settings: 1/100 shutter speed, auto ISO, f/13 aperture for images; and 1/30 shutter speed, 2200 ISO, f/13 aperture for videos. These settings ensured high-quality images suitable for correct analysis of the raw data. However, the images generated by automatic interval shooting were typically darker than those obtained by video recording (Figure 3.4a, b).

The magnification of the microscope has a zoom ratio ranging from 0.75X to 11.25X. The internal light source is not uniform, thereby causing an uneven illumination of the micromodel. This effect becomes more pronounced at lower zoom, resulting in the images that were lighter in the middle and darker in the corners. The shadows in the corners of the images and along the grains could also be created by an external light source (illumination in the laboratory). The effect of uneven illumination could be diminished by choosing a higher magnification of the microscope. For this reason, the images were generated with the zoom ratio 5X, which ensured both good-quality data and representative areal coverage of the porous media.

To ensure images with an even color distribution, the micromodel was placed parallel to the lens of the microscope. The micromodel assembled inside the aluminum holder was installed inside the cooling chamber, which in turn was placed on the laboratory table. This construction procedure resulted in a small angle developed between the micromodel and the microscope lens, which in turn induced a color gradient in the micromodel. As a result, some parts of the micromodel appeared reddish through microscopic view, whereas other parts had blueish appearance (Figure 3.4b, c).

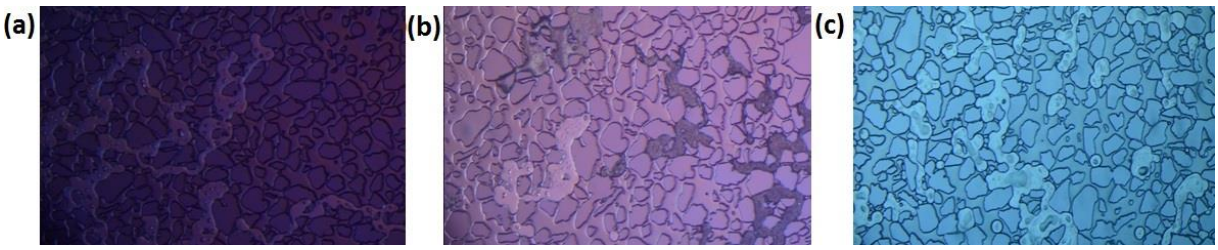

Figure 3.4. Images with different brightness and color. Image obtained by interval timer shooting appears darker (a) than by video recording (b). The images (b) and (c) were taken in different parts of the micromodel, which resulted in distinct colors.

3.2.3 Surface roughness

The DRIE construction technique caused the roughness of the micromodel surfaces, including pore walls and bottom of the silicon plate (Figure 3.5a). Due to the roughness of the micromodel bottom, water droplets could reside below the gas phase after the injection of fluids (Figure 3.5b). Depending upon their volume, these water droplets could have different appearance (Figure 3.6). Moreover, they sometimes acted as the nucleation sites for methane hydrate.

Rough pore walls could cause the light to be reflected from their surfaces, which in turn could result in the development of a thin light-blue layer between the grain surface and the gas phase (Figure 3.6a). Iden (2017) studied the effect of saline water on the hydrate behavior in micromodel and believed that the presence of salt crystals caused the observed thin light-blue layer. However, only distilled water was used in this thesis and it is therefore more likely that the thin light-blue layer was caused by light

reflection from the grains rather than by salt crystals. Note that these light reflections were not observed in those parts of the micromodel, which appeared blueish through microscopic view (Figure 3.6b). Light reflection from the grains assisted in a more accurate estimation of the hydrate growth rates along the pore walls because this light-blue layer transformed into black upon hydrate formation.

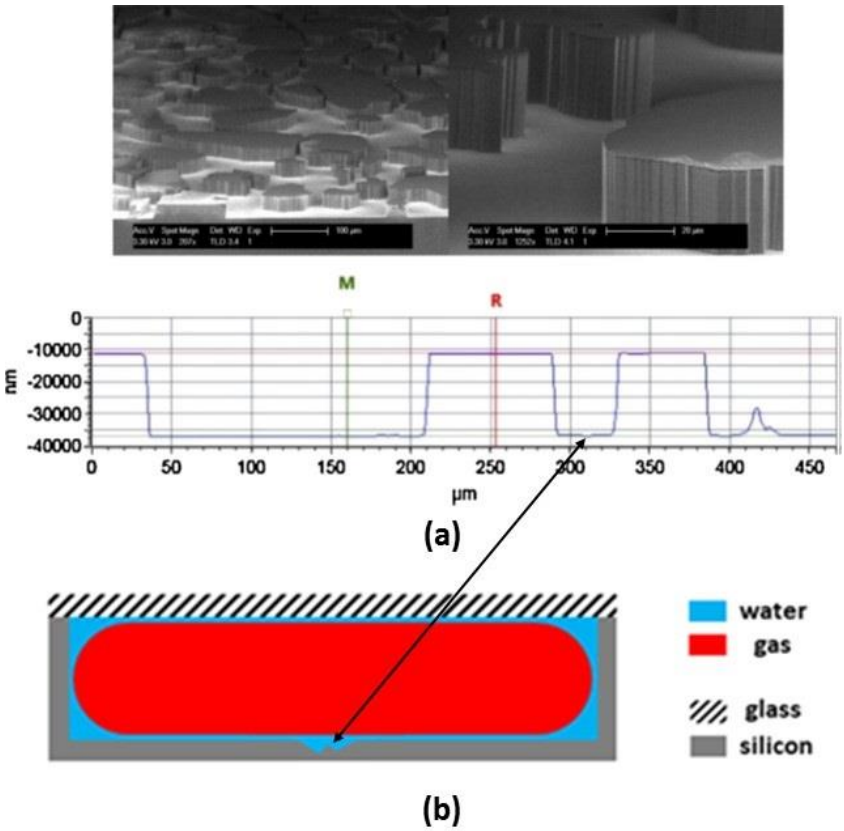

Figure 3.5. (a) Scanning electron microscope (SEM) images (top) and 1D-depth profiles (bottom) illustrating the rough pore walls and bottom of the micromodel. Images courtesy of PharmaFluidics (Modified from Hauge et al., 2016). (b) The pore cross-sectional area with the surface roughness, where the water droplet could accumulate (Modified from Almenningen et al., 2018). The arrows in the figure denote the surface roughness.

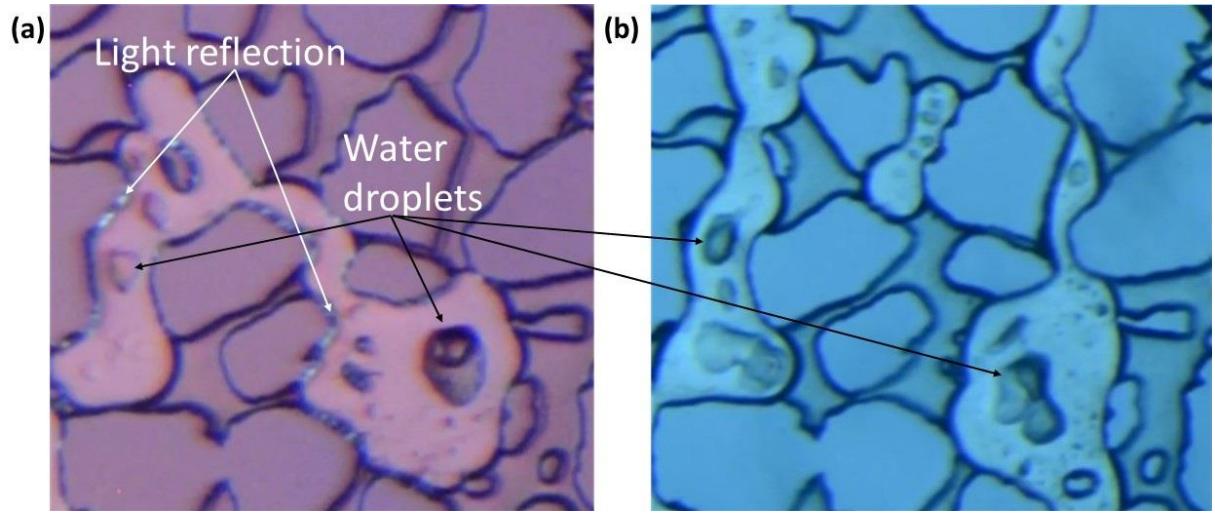

Figure 3.6. (a) Illustration of light-blue layers developed between the grains and gas due to light reflection from rough pore-walls and water droplets residing below the gas phase. (b) The image taken in the opposite side of the micromodel has another color and shows no sign of light-blue layers between the grains and gas.

3.3 Image analysis method

Besides the qualitative description of the hydrate formation and dissociation on pore-scale, the intention of this work was to quantitatively study the hydrate behavior. The estimated pore volume of the micromodel does not exceed 0.01 mL that is several orders smaller than the volume of tubing (Flatlandsmo, 2015; Iden, 2017). Therefore, any material balance calculations would not be applicable as they would be extremely sensitive to any small leakages from the system and possible plugging of the tubing upon hydrate formation. For this reason, fluid saturations and hydrate growth rates were estimated through the quantitative characterization of the images utilizing two different visualization software: Paint.net and ImageJ.

3.3.1 Hydrate growth rates

Hydrate growth rates were calculated by means of the image processing software ImageJ. In this work, methane hydrate was observed to grow in different locations: in the gas-phase along the water-gas interface and in the water phase. At the water-gas interface, hydrate appeared to grow at different rates depending on the direction. The hydrate growth along the pore wall (defined as the pore wall growth rate) was significantly faster than the perpendicular growth from the pore wall toward the pore center (defined as the pore center growth rate). Methane hydrate was also observed to grow in the water phase. Even though this growth was rare and detected only in few locations within the field of view, the hydrate growth in water was also quantified to provide an enhanced insight into the hydrate formation mechanism. Figure 3.7 shows a visual definition of all growth types.

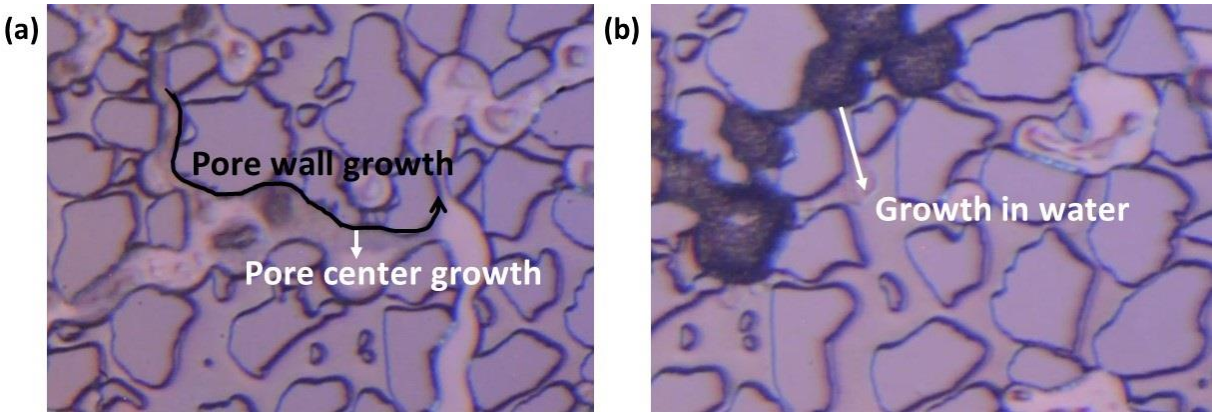

Figure 3.7. Visual definition of different growth types. (a) Pore wall growth (black) and pore center growth (white) at the water-gas interface. (b) Hydrate growth in the water phase.

The pore center growth rate was estimated by measuring the length between grain and hydrate propagation front towards the pore center at incrementing time step. The pore wall growth rate was calculated by measuring the distance between a fixed point on the grain surface and propagating hydrate film along grains at incrementing time step. The hydrate growth rate in water was estimated by measuring the length of the growing hydrate crystal from the water-hydrate interface at incrementing time step. The distance measured in pixels in ImageJ was converted to µm by comparing with a known reference distance in the micromodel. The data points were plotted on a graph of distance (µm) vs time (s) and a linear fit was then applied to all data points for each location, with the slope of a graph representing the growth rate.

The detection of the hydrate growth along the pore wall is complicated due to two main reasons. First, this growth type proceeds significantly faster compared with other growth types. Second, the hydrate film along the pore wall is so thin that it was sometimes difficult to observe with the selected microscope magnification. Therefore, the pore wall growth rate may generally have a greater uncertainty compared with two other growth types. Figure 3.8 illustrates the procedure for the

detection of the pore wall growth. The development of thin hydrate film along the pore wall is identified by the darkening of the light-blue layer between the grains and gas (red arrows on Figure 3.8).

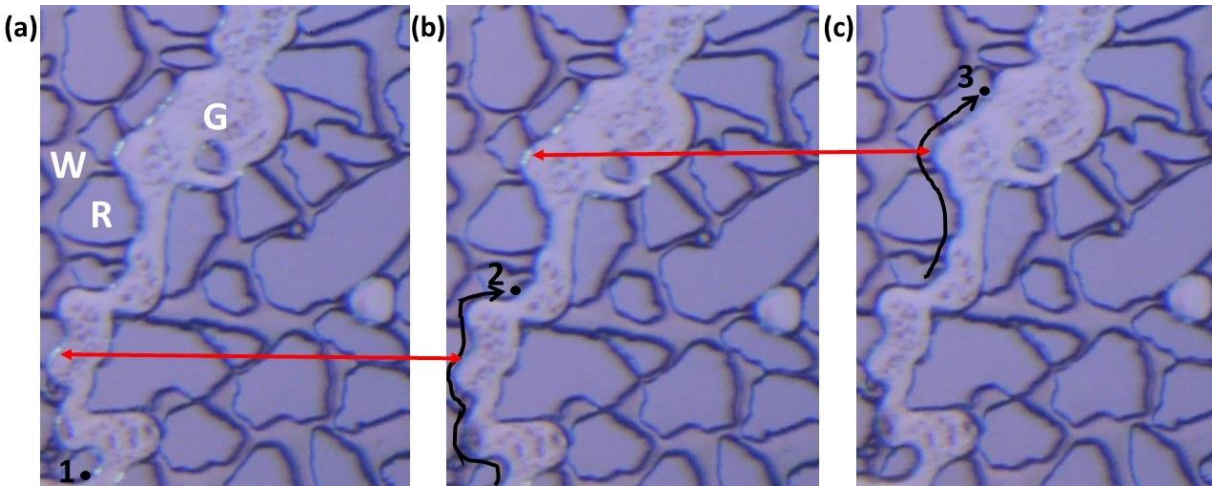

Figure 3.8. Detection of propagating hydrate film along the pore wall at incrementing time intervals. Gas (G), water (W) and grains (R) are present in the pore network. (a) Prior to hydrate formation: the light-blue layer between the grains and gas (due to light reflection from the rough pore wall) is denoted by the red arrow. Point 1 indicates the location where the development of a thin hydrate film is first detected. (b) and (c) The hydrate film propagates along the grains to the point 2 and 3 respectively indicated by the black arrows. The development of hydrate film is detected by the darkening of the light-blue layer between the grains and gas denoted by the red arrows.

Pore size determination

One of the objectives of this work was to investigate the effect of pore sizes on the hydrate growth rates. For this purpose, the pore center growth rates were estimated in distinct pore sizes. The pores were defined as the void space enclosed by the grains as shown on Figure 3.9. To estimate the size of a single pore with non-circular shape, an ellipse was inscribed within the pore and the length of the long and short axes were measured in ImageJ. The average pore diameter was then calculated by averaging the lengths of the axes. For the pores with approximately circular shape, the pore diameter was estimated by measuring the length between the grains. Since this procedure provides only a rough approximation of the pore sizes, all pores were classified into three main types: small, medium and large (Table 3.1).

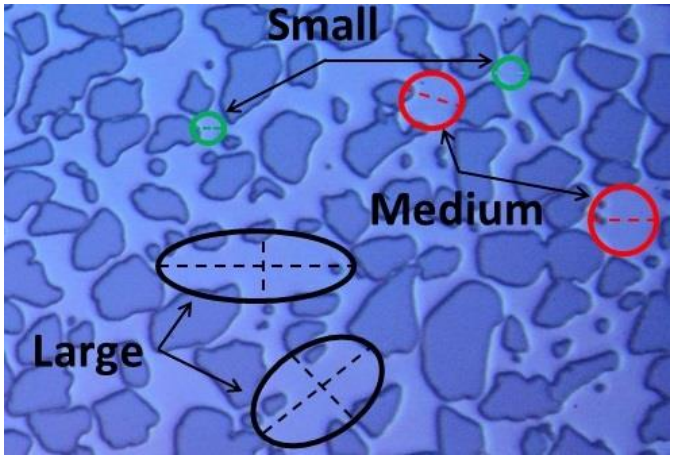

Figure 3.9. Three types of pore sizes: small (green), medium (red) and large (black). The dashed line represents the pore diameter.

Table 3.1. Different types of pore sizes and their respective diameter.

Pore type	Small	Medium	Large
Pore diameter [μm]	<80	Between 80 and 180	>180

3.3.2 Two-dimensional saturation

The growth rates were studied with respect to pore sizes and initial water saturation. The saturation profiles were obtained for hydrate dissociation to get an overview of how the fluid distribution is affected by pressure depletion. To estimate the initial water saturation in the entire micromodel prior to hydrate formation experiment, the images were captured in five different positions in the model: four in the corners and one in the middle of the model. The arithmetic mean of the estimated water saturations in the field of view was then calculated and the formula for standard deviation was used in the calculation of uncertainty. One image (field of view) was around 1% of the porous network area in the whole model.

The standard deviation for a sample set of data is calculated as follows:

$$S = \sqrt{\frac{\sum_{i=1}^{n}(x_i - \bar{x})^2}{n-1}} \tag{3.1}$$

where x_i is each value in the data set, $\bar{x}$ is the mean of all values in the data set and n is the number of values in the data set.

A graphics editor program Paint.net was utilized to estimate the porosity and saturation of each fluid occupying the porous network in the micromodel. A raw image was processed in Paint.net by locating and coloring the grains and all phases except water with distinct colors (Figure 3.10). The total image area is expressed in pixels, and each color covers a certain number of pixels. The two-dimensional porosity and fluid saturations were estimated through the pixel count analysis, utilizing the following computational formulas:

$$\phi_p = \frac{A_v}{A_{tot}} = \frac{N_v}{N_{tot}} = \frac{N_{tot} - N_{grains}}{N_{tot}} \tag{3.2}$$

where ϕ_p is porosity, A_v and A_{tot} are the area of void space and the total area of the image respectively, N_v, N_{tot} and N_{grains} are the number of void pixels, total number of pixels in the image and the number of grain pixels respectively.

$$S_i = \frac{A_i}{A_v} = \frac{N_i}{N_v} \tag{3.3}$$

where A_i is the area of a particular phase (gas or hydrate) in the image and N_i is the number of a phase pixels (gas or hydrate). Since the sum of all phases saturating the pore space must be equal unity, the water saturation was estimated as the difference between unity and the sum of remaining phases saturations.

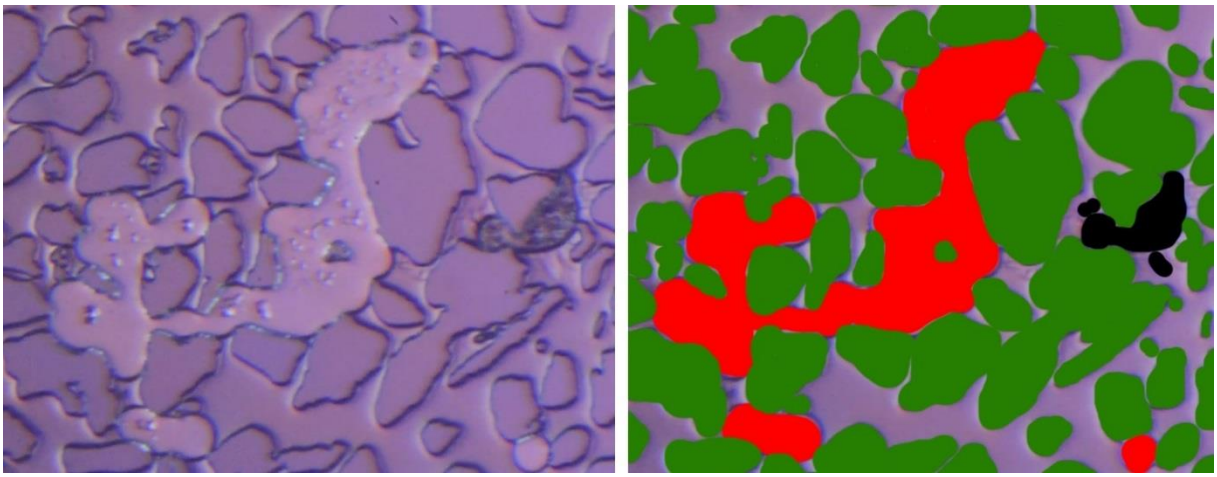

Figure 3.10. Saturation estimation procedure using Paint.net. Left: raw image. Right: processed image with grains, gas and hydrate films/shell being colored green, red and black respectively. Water remained uncolored.

If not otherwise stated, two-dimensional hydrate saturations were obtained under assumption that methane hydrate can appear both black (with encapsulated gas) and transparent (massive crystalline without gas). In other words, once the hydrate film encloses the gas phase (detected by black color), a pore is assumed to be saturated by hydrate in two-dimensional view, even though gas bubbles are encapsulated between or below hydrate film.

The saturation estimation procedure has two main limitations. First, the curves of fluid saturations are obtained locally within the field of view (around 1% of the entire micromodel area), whereas the fluid saturations may vary globally in the entire micromodel. Second, the estimated estimation profiles reflect only two-dimensional fluid distributions, whereas three-dimensional saturation profiles remain unclear due to possible coexistence of more than one fluid in the pore depth of 25 μm. Therefore, the obtained two-dimensional saturation curves are only a local approximation to the three-dimensional fluid distributions in the entire micromodel.

4 Results and discussion

This chapter reports the experimental results, which are described and analyzed both qualitatively and quantitatively. The chapter is divided into three main parts. Section 4.1 focuses on the qualitative description of hydrate formation, whereas section 4.2 quantifies the hydrate growth. Section 4.3 emphasizes the hydrate dissociation.

4.1 Hydrate formation mechanisms

To effectively extract natural gas from hydrates, an enhanced fundamental understanding of hydrate formation mechanisms and growth patterns is needed. The hydrate growth has extensively been studied in bulk systems and porous media on core-scale. By comparison, few authors have reported the direct pore-scale visualization of methane hydrate formation (section 2.1). This MSc project further investigates methane hydrate formation on pore-scale in high-pressure silicon micromodel. The results of this thesis supplement previous research on pore-scale hydrate growth, which in turn may assist in an improved interpretation of the general phenomena of methane hydrate formation in porous media.

Fifteen primary and twenty-two secondary hydrate formations were carried out in this MSc project, where secondary formation indicates the experiments performed by re-pressurizing the system after the primary hydrate had been dissociated. To distinguish between two types of hydrate formation, primary and secondary formation experiments are numbered differently. The primary hydrate formations are numbered from 1 to 15, whereas the numbering of the secondary formations has a general form of X_SEC_Y, where X denotes the reference primary formation experiment after which the secondary formation was performed and Y indicates the number in subsequent secondary formation experiments. For example, the experiment 8_SEC_3 is the third secondary formation experiment conducted after the primary hydrate formation in experiment 8.

Table 4.1 summarizes all primary hydrate formation experiments. The primary hydrate formation experiments 1-7 were carried out to study the hydrate formation mechanisms and to investigate the effect of initial water saturation in the entire micromodel (global saturation), $\bar{S}_{wi}$, and pore sizes on the hydrate growth rates. For this purpose, formation pressure, p, and temperature, T_{sys}, were maintained nearly constant, lying in the range of 83-84 bar and 1.2-1.4 °C respectively. The initial global water saturation varied from 0.30 to 0.60, and its uncertainty, $\Delta\bar{S}_{wi}$, is calculated as the standard deviation of saturation values estimated in five different parts of the micromodel (four in the corners and one in the middle), totally covering around 5% of the entire micromodel area. A significant scatter in $\Delta\bar{S}_{wi}$ is related to an uneven water distribution within the entire micromodel caused by gas injection. Six out of seven hydrate formations were induced by agitation (flow of fluids), whereas only one hydrate formation was achieved statically (condition of no flow and constant pressure) without agitation.

The intention of primary hydrate formation experiments 8-15 was to investigate the effect of driving force (expressed in terms of degree of subcooling) on the hydrate formation mechanisms and on the hydrate growth rates. These experiments were therefore performed at different pressures, ranging from 42 to 115 bar. The temperature was nearly constant and ranged between 1.4-1.6 °C, except from experiment 8. The initial global water saturation was approximately 0.50 (confirmed visually) for all experiments. All hydrate formations were triggered by agitation.

Table 4.1. Primary hydrate formation experiments.

Exp.	$\bar{S}_{wi}$ [fraction]	Non-constant $\bar{S}_{wi}$ $\Delta\bar{S}_{wi}$ ±	p [bar] ±1.4	T_{sys} [°C] ±0.2	Condition	Nearly constant $\bar{S}_{wi}$ Exp.	p [bar] ±1.4	T_{sys} [°C] ±0.2	Condition
1	0.45	0.16	83.0	1.2	Static	8	115.0	4.9	Agitation
2	0.33	0.13	83.0	1.3	Agitation	9	57.5	1.4	Agitation
3	0.60	0.04	84.0	1.3	Agitation	10	45.9	1.5	Agitation
4	0.30	0.01	83.0	1.2	Agitation	11	46.0	1.6	Agitation
5	0.39	0.10	83.0	1.4	Agitation	12	42.0	1.5	Agitation
6	0.50	0.06	83.0	1.3	Agitation	13	52.0	1.5	Agitation
7	0.50	0.04	83.0	1.3	Agitation	14	67.0	1.5	Agitation
						15	100.0	1.5	Agitation

An overview of secondary hydrate formations is presented in Table 4.2. The left part of Table 4.2 describes the secondary formation experimets that were conducted with varying pressure in the micromodel. The initial pressure, $p_{initial}$, specifies the pressure at which the hydrate growth was first observed within the field of view, whereas final formation pressure, p_{final}, denotes the final pressure at which the system was maintained. The intention of the secondary experiments with varying pressure was to examine the effect of increasing pressure on the hydrate growth mechanisms.

The right part of Table 4.2 summurizes the secondary formation experiments at which the system's pressure, *p*, was set to a constant value once the hydrate growth had been detected within the field of view. The range of experiments 8_SEC_1 – 8_SEC_11 was carried out to dissolve sifficient amount of methane in water to induce massive hydrate growth in the water phase. The main objective of the remianing experiments described in Table 4.2 was to further study the hydrate growth mechanisms and obtain more data for the measurements of the hydrate growth rates.

Table 4.2. Secondary hydrate formation experiments.

Exp.	Non-constant p $p_{initial}$ [bar] ±1.4	p_{final} [bar] ±1.4	T_{sys} [°C] ±0.2	Exp.	Constant p p [bar] ±1.4	T_{sys} [°C] ±0.2
4_SEC_1	60.0	83.0	1.1	7_SEC_5	80.0	1.2
7_SEC_1	77.0	81.1	1.3	7_SEC_8	32.6	1.2
7_SEC_2	38.0	81.1	1.3	7_SEC_9	62.0	1.3
7_SEC_3	39.0	82.5	1.3	7_SEC_10	75.0	1.3
7_SEC_4	63.0	82.5	1.3	8_SEC_1	79.0	2.6
7_SEC_6	32.0	83.0	1.2	8_SEC_2	57.0	1.6
7_SEC_7	32.0	80.0	1.2	8_SEC_3	60.0	0.1
8_SEC_9	80.0	105.0	0.6	8_SEC_4	40.0	0.1
				8_SEC_5	111.0	0.1
				8_SEC_6	110.0	0.1
				8_SEC_7	35.0	0.6
				8_SEC_8	117.0	0.7
				8_SEC_10	71.6	0.6
				8_SEC_11	115.0	0.6

The reported uncertainties in pressure and temperature are mainly due to apparatus. The Quizix Q5200 pump system has an uncertainty of ±1.4 bar, whereas the uncertainty of thermocouple lies within the range of ±0.1 °C. However, the overall uncertainty in temperature measurements was set to ±0.2 °C due to the temperature variations in the laboratory.

4.1.1 Observations of hydrate growth mechanisms

One can find a wide range of gas hydrate-related publications investigating the bulk systems. The experimental results have allowed the researchers to reach a consensus regarding the hydrate formation mechanism from a free gas phase and water in bulk volumes, where the hydrate growth initiates at the water-gas interface with a following hydrate film thickening and inhibited mass-transport through the solid hydrate layer. Investigations of gas hydrates in bulk systems do not reflect the effect of mineral surfaces, wettability, capillarity and fluid distributions. The gas hydrate studies in porous media are therefore needed to improve overall knowledge about the hydrate formation mechanisms in nature. This MSc research project adds information to previously proposed hydrate formation mechanisms in artificial sediments (Tohidi et al. (2001); Katsuki et al. (2007); Hauge et al. (2016)).

Figure 4.1 provides a visual description of the main steps in hydrate formation. In this particular example and in chapter 4 in general, the symbols W, G, WD, R, HF, Hw and H denote water, gas, water droplets, grains, hydrate films/shell, hydrate grown in water and crystalline hydrate respectively. The pore space was initially filled with gas and water (image a). Hydrate growth was first observed to occur at the water-gas interface in the continuous gas phase along the pore walls, followed by the hydrate film propagation towards the pore center (image b). Further growth distributed to the isolated gas bubbles with similar formation pattern from the pore walls towards the pore center (image c). After the hydrate films/shell had developed around methane (both continuous and isolated), the gas phase could either be totally consumed by inward crystal growth with a subsequent conversion to crystalline hydrate (symbol H in image d); or remain in the pore space as a bubble trapped inside the hydrate films/shell. The hydrate growth in the water phase was only noticed in few locations and initiated at the phase boundary between water and hydrate (symbol Hw in image c). Hydrate growth was also observed in the initially water-filled pores due to water displacement by gas (green circles in images d and e). All the hydrate formation steps described here will be discussed separately and in detail in this section.

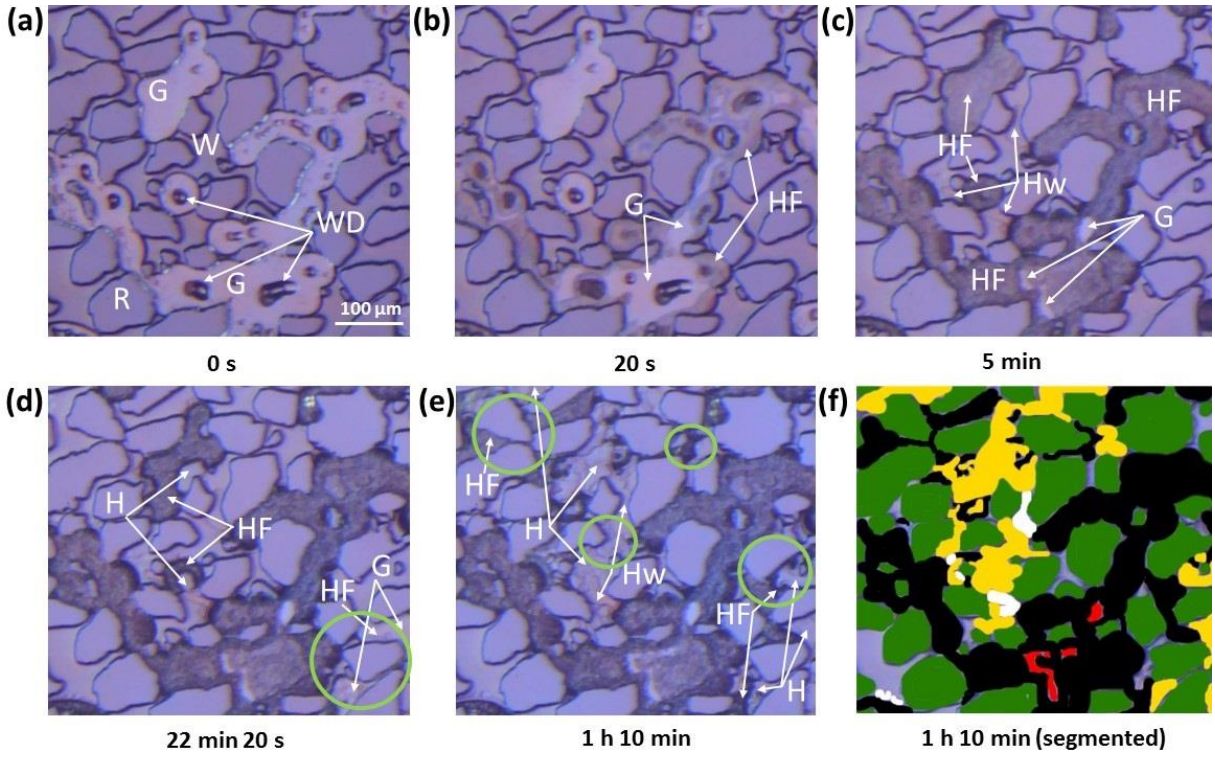

Figure 4.1. Image sequences from primary formation experiment 2. The time lapses after the onset of hydrate formation are provided below each image. (a) Micromodel prior to hydrate formation. Water (W), methane gas (G), grains (R) and water droplets (WD) residing below the gas phase are present in the micromodel. (b) Hydrate films/shell (HF) enclose the continuous gas phase with a growth pattern from pore walls towards the pore center. (c) The hydrate films/shell (HF) development spreads to isolated gas bubbles. Hydrate crystals also grow in the water phase (Hw) with a transparent appearance. (d) and (e) illustrate (1) the development of crystalline hydrate (H) with a transparent appearance; and (2) hydrate formation [both as films/shell (HF) and crystalline (H)] in the previously water-filled pores (green circles). (f) is a segmented illustration to (e) with hydrate films/shell encapsulating the gas phase (black), gas (red), crystalline hydrate (yellow) and hydrate crystals grown in the water phase (white). Water remained unsegmented.

Hydrate growth at the water-gas interface in the continuous gas phase

Similar to bulk volumes and previous hydrate studies in the micromodels (section 2.1), the hydrate growth initiated at the water-gas interface since the concentrations of water and methane at their interface greatly exceeds mutual fluid solubilities (Sloan, 2003). However, instead of simultaneous growth at all water-gas interfaces, the hydrate film first developed rapidly at the interface between a thin water film coating the grains and gas and then distributed towards the pore center at a significantly slower rate. Hydrate always grew first in the continuous gas phase due to sufficiently high connectivity and availability of the hydrate formers, which in turn ensured relatively rapid propagation of the hydrate formation front through the porous network.

Hauge et al. (2016) also observed similar growth pattern from the pore wall towards the pore center, which was explained by the system's wettability and rectangular cross-sectional shape of the pores. Due to the water-wet nature of the micromodel, water films are expected to coat the grains as well as the bottom (silicon) and top (glass) of the micromodel when gas displaces water from the pores. The rectangular cross-sectional shape of the pores leads to accumulation of thick water pockets in the pore corners, whereas gas resides in the pore center with a curved water-gas interface (Figure 4.2). As a result, the hydrate first grows rapidly along the pore walls due to relatively high water availability compared with top and bottom surfaces of the micromodel. Subsequent hydrate growth towards the pore center is much slower as it relies on the relatively slow water migration through the wetting water films from pore corners and neighboring water-occupied pores. For experiments 1-7 with nearly similar pressure-temperature conditions, the hydrate growth along the pore walls (pore wall growth rate) was

approximated to 1100 µm/s, whereas the growth towards the pore center (pore center growth rate) was on average 8 µm/s, which is approximately two orders of magnitude slower. A brief discussion of the hydrate growth rates will be provided in section 4.2.

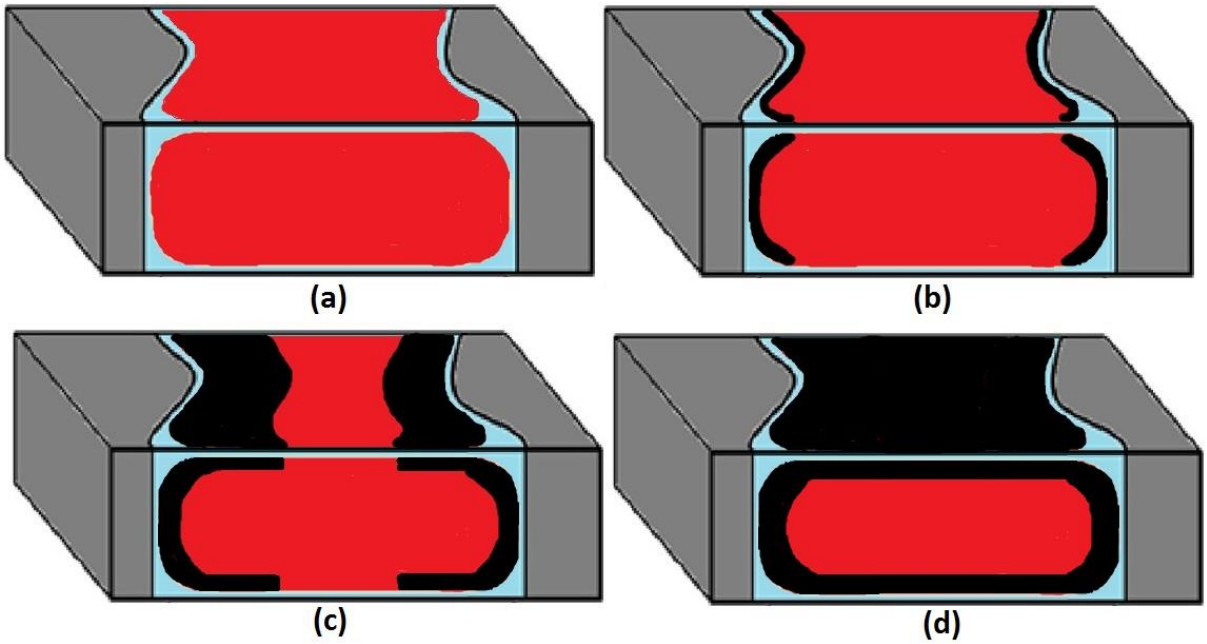

Figure 4.2. Three-dimensional conceptual model of a single pore in the micromodel with grains (grey), water (blue), gas (red) and hydrate films/shell (black) (modified from Hauge et al., 2016). (a) Thin water films coat the top and bottom part of the micromodel as well as the grains due to water-wet nature of the porous network. Wetting water films coating the top of the micromodel are drawn only in two-dimensional cross-sectional view. Water films are thicker in the pore corners due to rectangular cross-sectional shape of the pore and curved water-gas interface. (b) Thin hydrate film develops rapidly along the grains (pore walls) due to higher water accessibility. (c) Hydrate grows slowly from the pore walls towards the pore center encompassing the gas phase. (d) Gas is completely enclosed by hydrate films/shell.

The observed hydrate films/shell development from pore corners towards pore center underlines the importance of the pore shape on the growth pattern. Various pore geometries exist in nature, with both angular and rounded shape. Consider three distinct water-wet pore structures: flat (triangular-shaped), convex (star-shaped) and concave (circular-shaped) as shown in Figure 4.3.

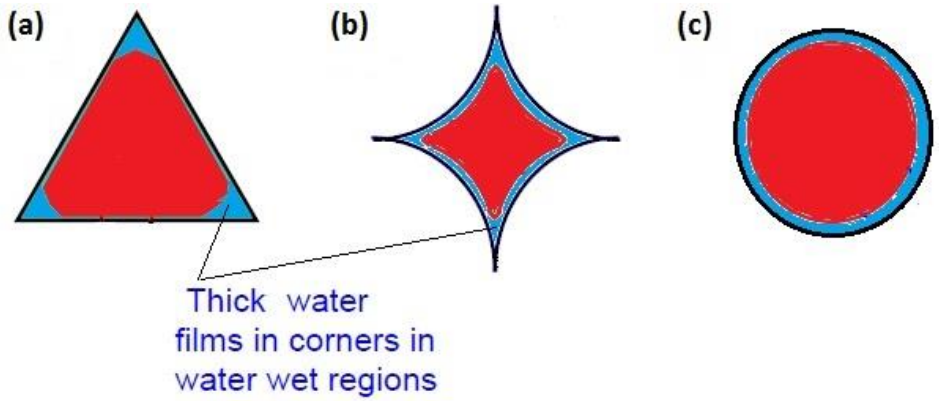

Figure 4.3. Alternative cross-sectional pore shapes with grains contact (black), water films (blue) and gas (red) (Modified from Skauge, 2016). Gas hydrate is expected to grow first in the pore corners of triangular-shaped (a) and star-shaped (b) pores due to thicker water films. In circular-shaped pores (c), hydrate is expected to grow at all water-gas interfaces simultaneously.

In convex and flat pores, thick water films accumulate in the pore corners, whereas they are thinner in the remaining parts of the pore. Thus, hydrate is expected to grow first at the water-gas interface in the pore corners. In contrast, wetting water films in the concave pores have uniform thickness, likely causing the hydrate film to develop at all water-gas interfaces simultaneously. This model is appropriate only in strongly water-wet pore network with ideal pore shapes. The naturally occurring systems can have heterogeneous wettability and pore shapes with significant surface roughness and facilitate various growth patterns.

Hydrate growth in the isolated gas phase

Once the hydrate films/shell had encapsulated the continuous gas phase, further growth proceeded to the isolated gas bubbles. As in continuous gas, hydrate films/shell first grew along the pore walls, with a following movement towards the pore center. The mechanisms by which hydrate growth proceeded in the isolated gas bubbles varied. In some cases, hydrate formation occurred in isolated gas due to contact with a hydrate crystal growing in water (Figure 4.4). In other cases, hydrate growth spread to isolated gas bubbles without any visible hydrate front movement (Figure 4.5). Tohidi et al. (2001) observed similar behavior, which was explained by a change in the structure of the surrounding water. Likely, hydrate formation in isolated gas could also be caused by movement of very small hydrate crystals through water from hydrate-forming area; however, this transport was not detected due to insufficient resolution.

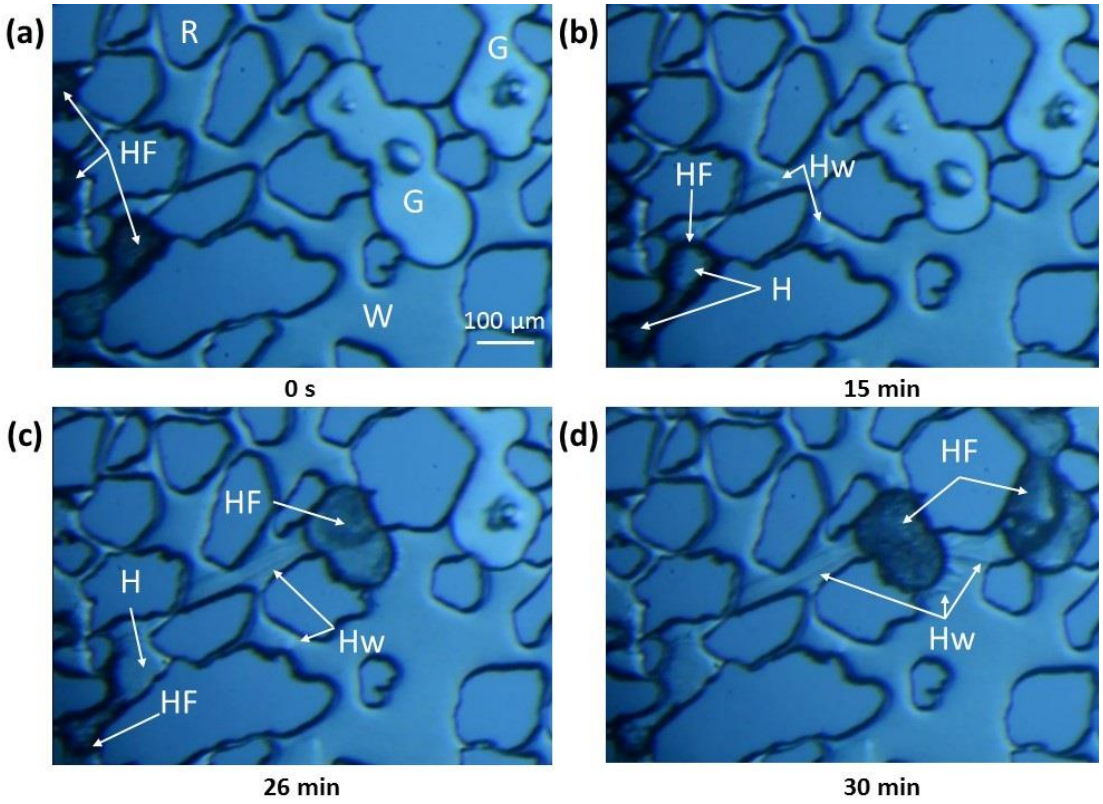

Figure 4.4. Hydrate films/shell formation (HF) in isolated gas bubbles (G) due to hydrate crystals growing in water (Hw) in experiment 14. (a) The gas phase already enclosed by hydrate films/shell (HF) and free gas bubbles (G) are present. (b) Hydrate crystals grow in water (Hw). A fraction of gas is consumed and converted to crystalline hydrate (H). (c) Hydrate films/shell (HF) enclose the isolated gas bubble when the growing hydrate crystal (Hw) encounters gas. (d) Hydrate crystal growing in water (Hw) encounters another gas bubbles with consequent development of hydrate films/shell (HF).

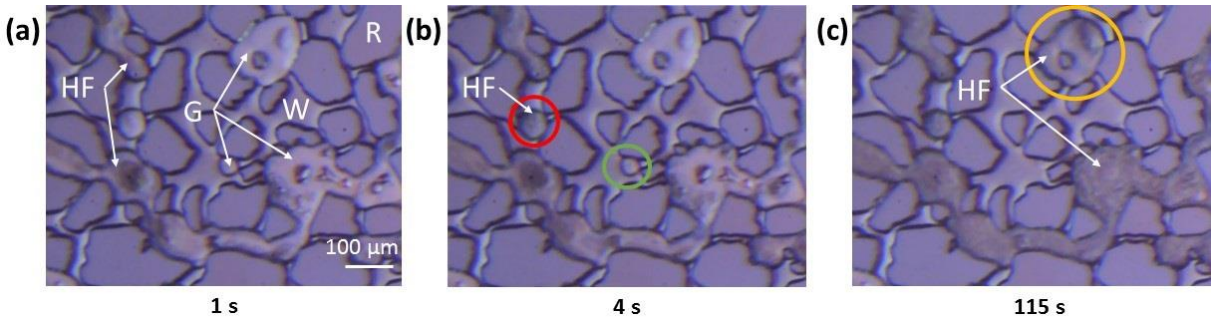

Figure 4.5. Hydrate films/shell formation (HF) in isolated gas bubbles (G) without visible hydrate front movement (experiment 2). (a) 1 s after the hydrate films/shell (HF) had started to develop around continuous gas phase. (b) Hydrate growth spreads to the closest isolated gas bubble (red circle). (c) Another gas bubble (yellow circle) is enclosed by hydrate films/shell. Note that the small isolated bubble denoted by a green circle in (b) is dissolved in water instead of conversion to hydrate.

Even though no specific growth pattern emerged, hydrate formation in the isolated gas bubbles seemed to depend on the distance from already developed hydrate. It was observed that the isolated gas bubbles closest to hydrate were first to be encompassed by the hydrate films/shell. This is an expected behavior as the shortest distance between isolated gas and hydrate-forming area ensures the fastest transfer of hydrate crystals to the isolated gas.

Hydrate growth in the water phase

Hydrate crystals were observed to grow in water at the water-hydrate interface. However, this growth was rare, mainly due to restricted methane transfer to supply further growth. Methane could be supplied to the hydrate-forming region from two different sources: 1) through water as dissolved gas and 2) through the hydrate films/shell from gaseous methane trapped inside the films/shell. Methane transfer from these two sources is limited due to poor methane solubility in water and inhibited mass transport through the solid hydrate films/shell.

The growth of hydrate crystals in water was mainly observed in regions where the isolated free gas bubbles resided within a relatively short distance from already formed hydrate. Figure 4.6 shows the hydrate crystal growth in water. As a hydrate crystal grew, neighboring methane bubble shrunk, suggesting gas dissolution and its transport through water to the hydrate forming area. The hydrate growth in water ceased when neighboring gas bubble was either completely dissolved or converted to hydrate. This behavior can be interpreted by difference in concentrations of dissolved methane in pore water and in the hydrate forming area. The hydrate formation decreases the concentration of dissolved gas in the vicinity of hydrate, whereas its concentration in pore water remains constant (Katsuki et al., 2007). The resulted concentration gradient and insufficient amount of dissolved gas in water cause dissolution and transfer of isolated gas bubble to the existing hydrate surface to sustain further hydrate growth. The grown hydrate crystals resembled the columnar/faceted morphology as shown on Figure 1.12a and Figure 1.14a.

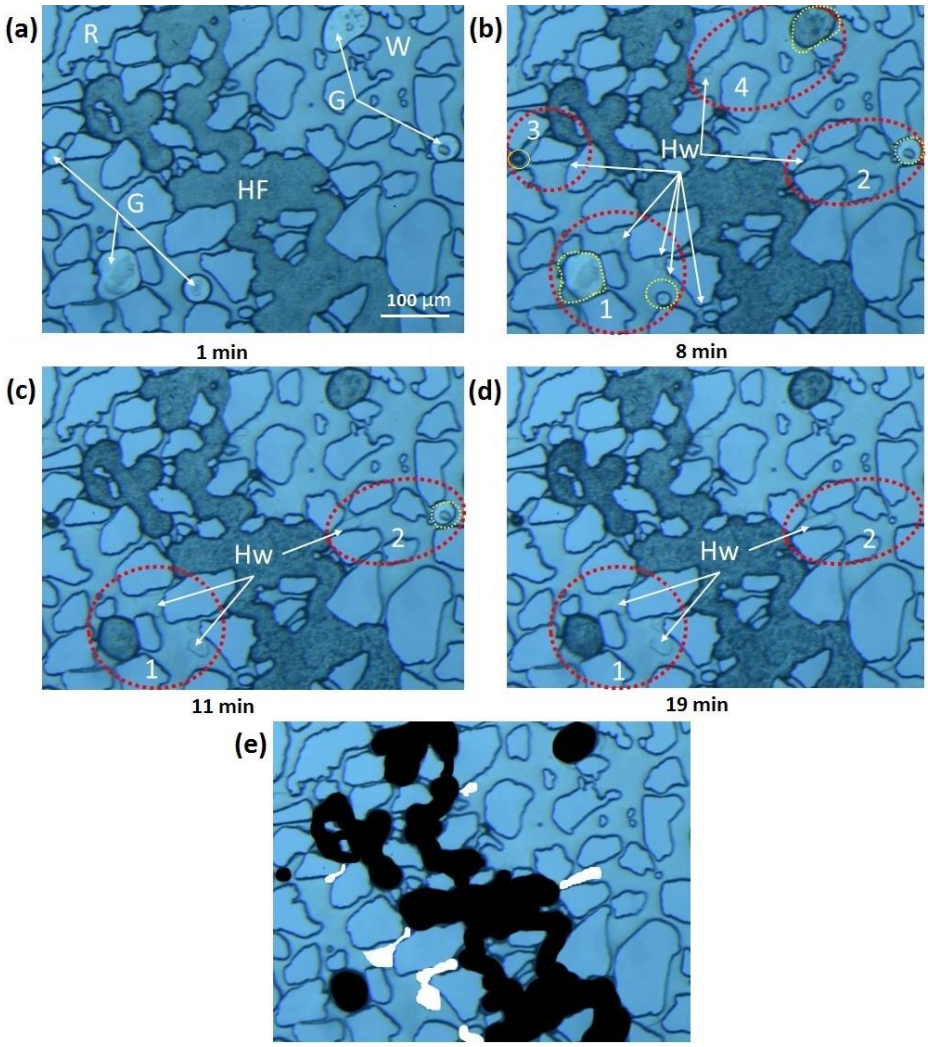

Figure 4.6. Illustration of hydrate crystals growth (Hw) in water in experiment 3. (a) 1 min after the initial hydrate growth (HF) had been observed in the continuous gas phase. Isolated gas bubbles (G) are not converted to hydrate. (b) Hydrate crystals grow in four different areas (red circles) where the isolated gas bubbles are available. As crystals grow, neighboring gas bubbles shrink, suggesting dissolution and transport of gas to hydrate-forming area. The dashed yellow circles indicate the original size of bubbles. In areas 3 and 4, hydrate crystals terminate to grow because the neighboring gas bubbles are encapsulated by hydrate films/shell. (c) In area 1, the largest gas bubble is enclosed by hydrate films/shell, whereas the smallest bubble is completely dissolved. As a result, growth of hydrate crystals in water ceases. In area 2, hydrate crystal continues to grow. (d) In area 2, the gas bubble is completely dissolved, leading to termination of hydrate growth in water. (e) Segmented illustration of (d) with hydrate films/shell (black) and hydrate crystals grown in water (white). Water and grains are not segmented.

Two mechanisms govern the growth of hydrate crystals in water: gas diffusion through hydrate films/shell and gas transport through water. The hydrate growth in water preferentially initiated at the water-hydrate interfaces near the isolated gas bubbles and terminated when these bubbles become unavailable due to complete dissolution or conversion to hydrate. Therefore, transport of dissolved gas through water is likely a main controlling mechanism of growth in water, especially at later stages. However, gas diffusion through hydrate films/shell coupled with gas transport through water may control the growth of hydrate crystals in water at earlier stages when porous hydrate film has not yet been completely solidified, thereby allowing some gas transfer (see “Hydrate formation mechanism” in section 1.4.3 for a discussion of porous vs solid nonporous hydrate film). The hydrate growth rate in water was averaged to 0.3 µm/s (experiments 2-6), which is approximately one order of magnitude slower than pore center growth rate at the water-gas interface. This supports the dependence of the hydrate growth in water on slow methane-transfer.

Hydrate growth in initially water-filled pores

Hydrate formation was not only restricted to gas-filled pores but also occurred in initially water-filled pores if gas partially displaced water. Similar observation was reported and explained by Hauge et al. (2016). Since there was no sign of hydrate dissociation within the field of view, local pressure differences in the neighboring pores induced by volume expansion upon hydrate formation were likely responsible for the gas movement in the hydrate-filled pores. Figure 4.7 illustrates the fluid transport through hydrate-filled pores. The emergence of gas at the water-hydrate interface (yellow circle) initiates the water displacement in the adjacent pore (red circle). Upon advancing, gas phase transforms into hydrate behind the front, saturating the initially water-filled pores with hydrate. The displaced water seemed to enter the hydrate-filled pore (black circle) and consume the encapsulated gas, leading to the conversion of the hydrate films/shell to crystalline hydrate. Gas mobilization within the hydrate-filled pore suggests that hydrate films/shell do not necessarily encapsulate the entire gas phase, thereby allowing gas to escape the pore.

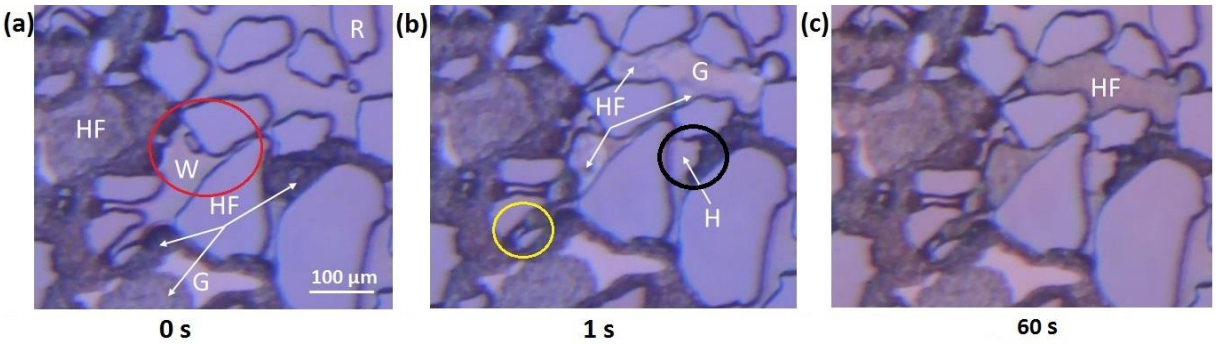

Figure 4.7. Hydrate formation in the initially water-filled pores. (a) Hydrate films/shell (HF) with enclosed gas, free gas phase (G), water (W) and grains (R) are present in porous media. The pore where water will be displaced from is marked by a red circle. (b) Gas (G) appears at the water-hydrate interface (yellow circle), with a hydrate films/shell (HF) forming behind propagating gas. Some part of water is likely displaced to the adjacent-hydrate-filled pore (black circle) and then consumes a fraction of gas with a subsequent conversion to crystalline hydrate (H). (c) Hydrate films/shell (HF) completely encapsulate the gas phase in the previously water-filled pore.

Additional observations

The hydrate growth pattern from pore walls towards pore center along the water-gas interface was observed in the absolute majority of the experiments. However, hydrate growth could also initiate in the pore center and along the pore walls simultaneously (Figure 4.8). As a result, the hydrate film front formed and propagated through the pore space in a direction marked by black arrows. This behavior was particularly noticed when hydrate growth initiated in narrow pore channels, which were in a direct contact with already existing crystalline hydrate (from previously dissociated system).

As discussed in section 3.2.3, water droplets could accumulate below the gas phase due to the surface roughness of the micromodel bottom. In some cases, these water droplets acted the nucleation sites for hydrate formation, resulting in the growth pattern from pore center towards pore wall. In other cases, they were converted to hydrate when the advancing hydrate front contacted these water droplets (Figure 4.8d).

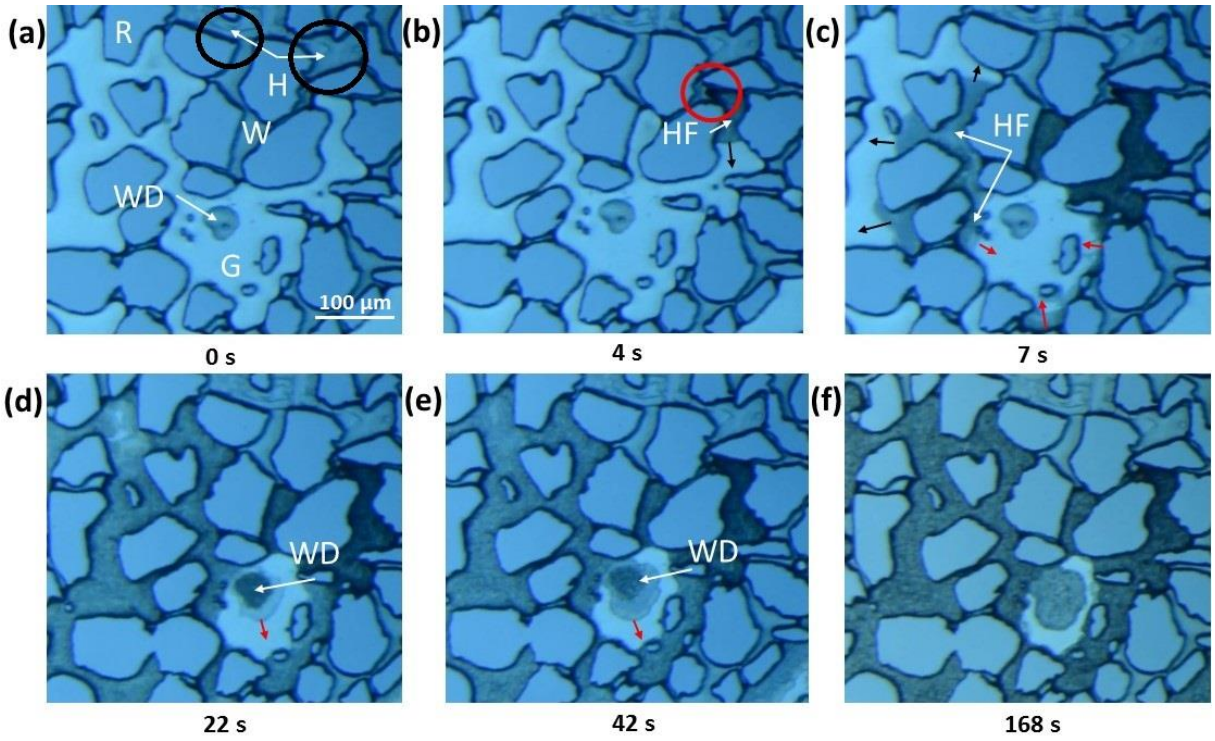

Figure 4.8. Hydrate formation in experiment 7_SEC_9. (a) Crystalline hydrate (H) from previous dissociation remain in the porous network (black circles). Water droplet (WD) resides below the gas phase (G). (b) Hydrate growth (HF) initiates at the interface between gas and already existing crystalline hydrate (red circle). A black arrow denotes the direction of resulting hydrate formation front. (c) Hydrate (HF) continues to grow through the pore space in the narrow pore channels (black arrows). In the larger pore, hydrate grows from the pore walls towards the pore center (red arrows). (d) The growing hydrate encounters the water droplet (WD), initiating further growth from water droplet towards the pore walls (red arrow). (e) The hydrate growth from water droplet continues towards the pore walls. (f) The water droplet is completely converted to hydrate, terminating further growth.

4.1.2 Hydrate configurations in porous media

Direct visual studies of hydrate pore occupancy can reveal valuable information regarding the cementing nature of gas hydrates, which in turn may have a direct impact on slope stability, hydrate detection and fluid permeability. As stated in section 1.4.4, gas hydrate can occupy the pore space (pore filling) as well as reside on the grain surface (grain cementing).

In this work, two different hydrate configurations within a pore space were observed: crystalline and hydrate films/shell with enclosed gas (Figure 4.9). Crystalline hydrate was mostly observed as dendritic crystals, similar to Katsuki et al. (2007). As discussed in section 3.2.1, crystalline hydrate appeared transparent through microscopic view, whereas hydrate films/shell had a black color. Almenningen et al. (2018) reported similar hydrate configurations and pointed out that insufficient mass-transport and/or pressure inside the gas phase was likely a cause of development of hydrate films/shell without total conversion of gas to hydrate. The experimental results reported here allow to further investigate the nature of crystalline hydrate and hydrate films/shell. This section provides a detailed discussion of factors leading to formation of two distinct hydrate configurations both globally (in the entire micromodel) and locally (within the field of view).

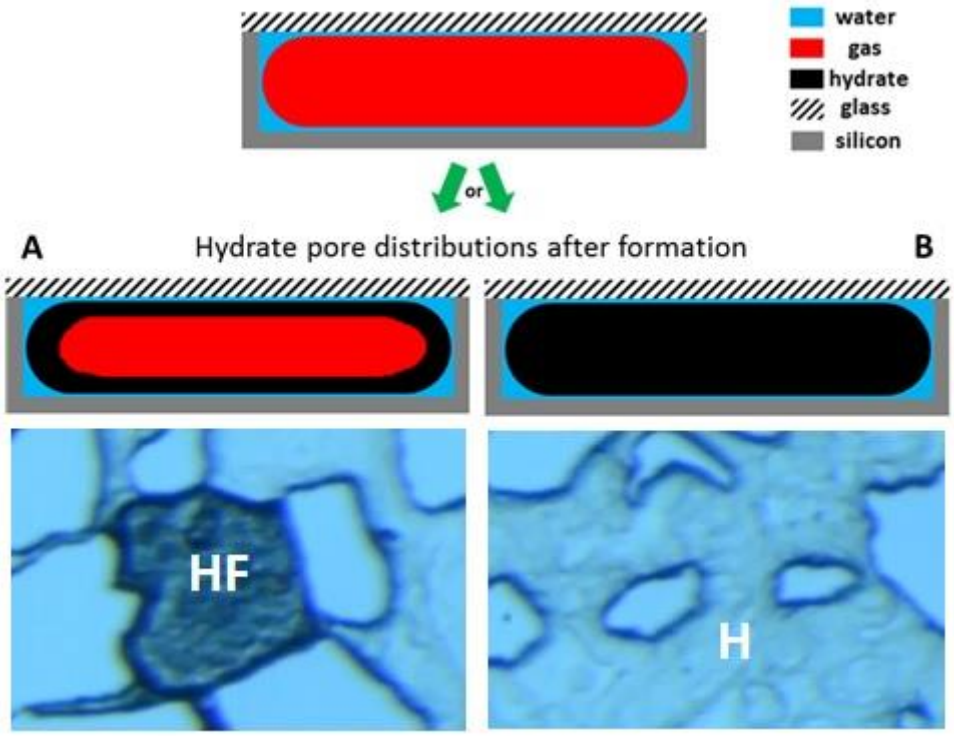

Figure 4.9. Two distinct hydrate configurations observed in this work. Top: schematic of hydrate pore-occupancy (Almenningen et al., 2018). A pore is initially filled by gas (red) and water (blue). Upon hydrate growth, gas is either enclosed (A) or totally consumed (B), thereby forming either hydrate films/shell or crystalline hydrate respectively. Bottom: illustration of black hydrate films/shell (HF) and transparent crystalline hydrate (H) with dendritic morphology in experiment 5.

Global hydrate configuration

Crystalline hydrate formed in the pore space (detected by color transformation from black to transparent) as a result of total gas consumption by inward crystal growth. Adequate water-transfer through hydrate films/shell and/or pressure support was required to totally convert the enclosed gas to hydrate. In the entire porous network, total gas consumption could be achieved mainly because of initial excess water saturation or additional water supply to the micromodel. When the initial global water saturation exceeded gas saturation, all hydrate forming regions had an excess to sufficient amount of water to maintain further gas consumption. This resulted in the formation of crystalline hydrate in all gas-filled pores (Figure 4.10). When water was the limiting component in relation to gas, total gas consumption could be triggered by water injection during hydrate growth (Figure 4.11). This ensured an adequate water-transfer and continuous surface renewal. The injection of water provides a continuous water supply and redistribution of gas and water in the model. Continuous water supply in turn ensures an adequate water-transport to hydrate-forming region, whereas surface renewal improves a water diffusion through hydrate films/shell. In fact, six out of eight secondary formation experiments (Table 4.2left) as well as primary formation experiments 1 and 11 where additional water supply was provided during hydrate growth resulted in the formation of crystalline hydrate.

Two different hydrate configurations (crystalline and films/shell) formed three distinct global hydrate distributions within the entire micromodel, where hydrate phase was mostly represented by (1) crystalline hydrate, (2) hydrate films/shell with enclosed gas, and (3) combination of crystalline hydrate and hydrate films/shell. These hydrate distributions will later be discussed in relation to hydrate dissociation (section 4.3.2).

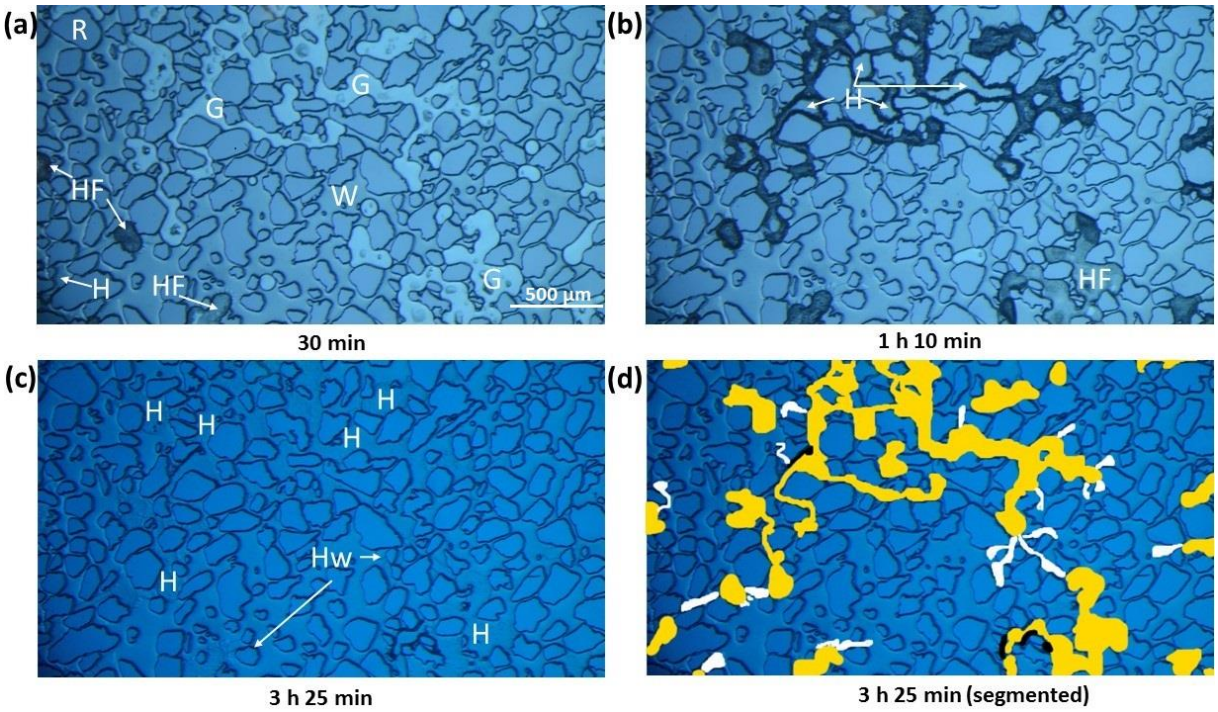

Figure 4.10. Total gas consumption in the entire micromodel due to excess water saturation in experiment 14. (a) 30 min after the initial hydrate growth was observed within the field of view. Most of the gas phase (G) is not encapsulated by hydrate films/shell (HF). Crystalline hydrate (H) grew in the lower left part of the image due to gas consumption. (b) Hydrate films/shell (HF) enclose most of the gas. Some part of the gas phase is consumed, with a consequent formation of crystalline hydrate (H). (c) Hydrate phase is mostly represented by crystalline hydrate (H) due to total gas consumption. Hydrate crystals also grew in water (Hw). (d) Segmented image of (c) with crystalline hydrate (yellow), hydrate crystals grown in water (white) and hydrate films/shell (black). Water and grains remain unsegmented.

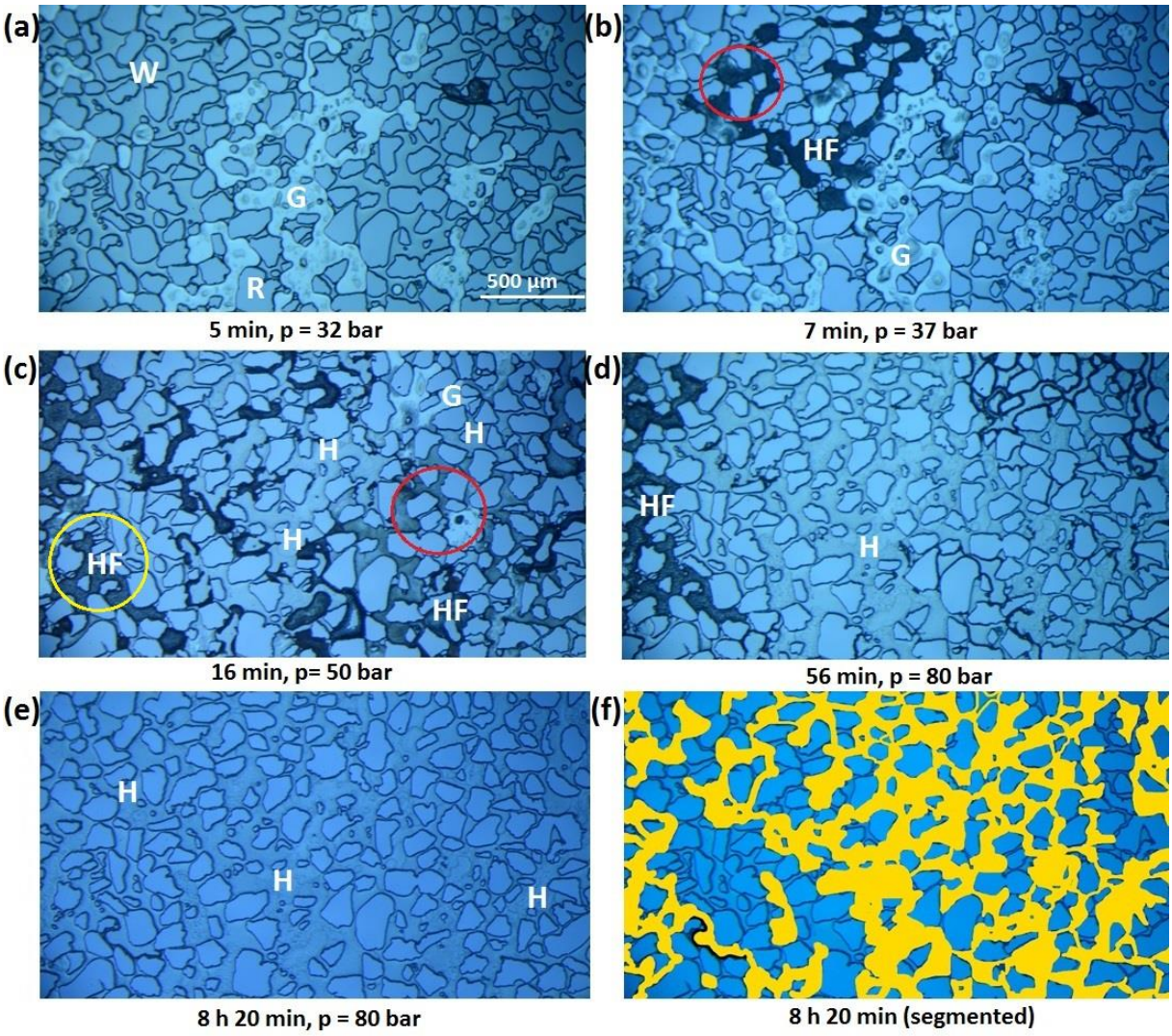

Figure 4.11. Total gas consumption in the entire micromodel due to additional water supply in experiment 7_SEC_7. Pressure is increased by injecting water from water pump cylinder. (a) 5 min after initial hydrate growth in the field of view. Porous media is mainly saturated with gas (G) and water (W). (b) Water and gas redistribution (red circle) due to pressure increase. Hydrate films/shell (HF) grow around gas (G). (c) Further pressure increase and subsequent redistribution of water and gas. Hydrate films/shell (HF) encapsulate the gas phase in the gas-filled pores (yellow circle) and previously water-filled (red circle). Some of the gas phase is consumed with a consequent development of crystalline hydrate (H). (d) The system reaches its final pressure. Most of gas is consumed with a conversion to crystalline hydrate (H). Hydrate films/shell with enclosed gas (HF) are still present within the field of view. (e) Gas is almost totally consumed to form hydrate. Crystalline hydrate (H) occupies most of the porous network. (f) Segmented illustration of (e) with crystalline hydrate (yellow) and hydrate films/shell with encompassed gas (black). Water and grain are not segmented.

Local hydrate configuration

In case of excess gas saturation in the model and no additional water supply, crystalline hydrate tended to develop locally (within the field of view) in isolated gas, whereas the continuous gas phase remained encapsulated by hydrate films/shell without total conversion to crystalline hydrate (Figure 4.12). This can be explained by water-transport limitations to hydrate forming area and restricted diffusion through hydrate films/shell. In pores occupied by a continuous gas phase, water is available in small quantities, primarily as thin wetting films coating the grains and thicker water pockets in the pore corners (Figure 4.13a). A significant fraction of water that accumulated in the pore corners is likely consumed upon the development of hydrate films/shell. Additional water supply is therefore required to maintain further hydrate growth, which can be accomplished through water-transfer from adjacent water-filled pores along wetting films. However, this water migration is time-consuming; and therefore

the hydrate films/shell grow and solidifies gradually with the consequence of reduction in permeability before water can be transported to the hydrate forming region. In contrast, in pores filled by isolated gas bubble, water availability is supported not only by wetting films but also by pore water surrounding the trapped methane bubble (Figure 4.13b). Mass-transport through wetting films from adjacent pores is therefore not required to convert isolated gas to hydrate due to sufficiently high water availability and relatively small gas volume compared to pores filled with continuous gas.

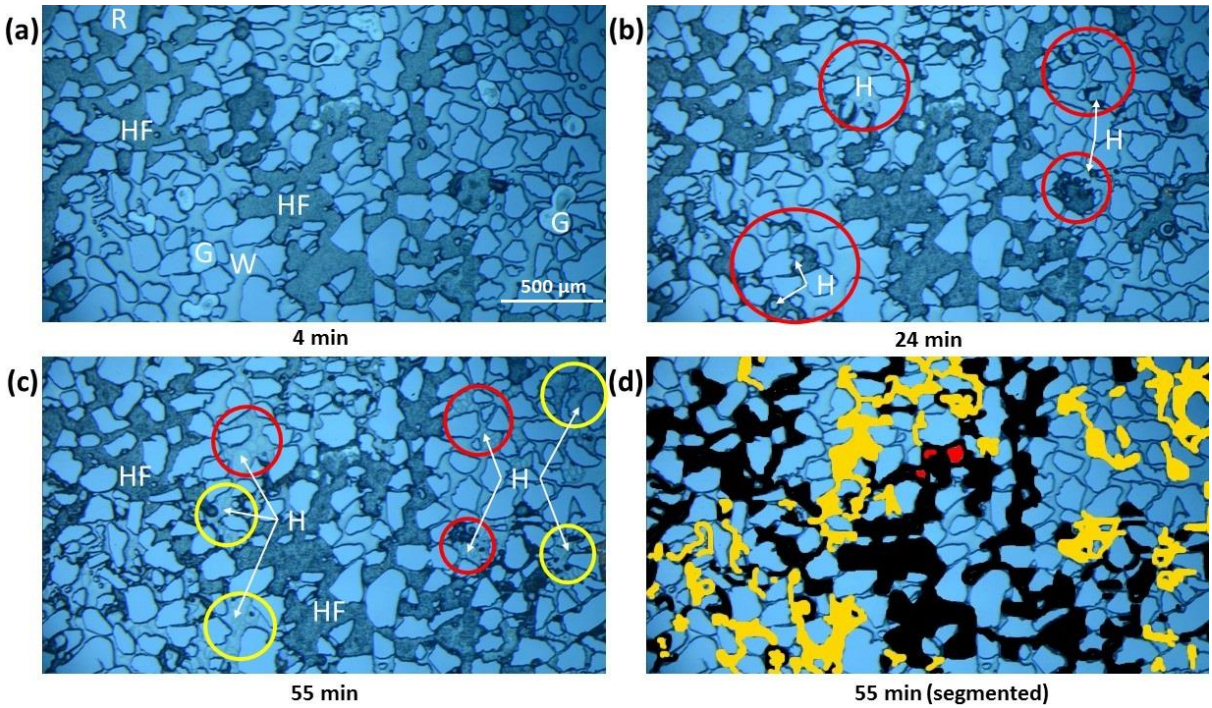

Figure 4.12. Hydrate formation experiment 7_SEC_10. (a) Fluid distributions 4 min after the initial growth was observed in the field of view. Hydrate films/shell (HF) encapsulate the continuous gas phase and several isolated gas bubbles. Some isolated gas bubbles (G) are not enclosed by hydrate films/shell yet. Water (W) and grains (R) are also present in the field of view. (b) All gas bubbles are encapsulated by hydrate films/shell. Consumption of isolated gas bubbles initiates in the areas denoted by red circles, with the formation of crystalline hydrate (H). (c) Development of crystalline hydrate (H) in the previously water-filled pores due to water displacement by gas (yellow circles). In the areas denoted by red circles, crystalline hydrate (H) reside in the pores initially occupied by isolated gas bubbles. The continuous gas phase is not totally consumed and is encompassed by hydrate films/shell (HF). (d) Segmented illustration to (c) with hydrate films/shell (black), crystalline hydrate (yellow) and gas (red). Water and grains remain unsegmented.

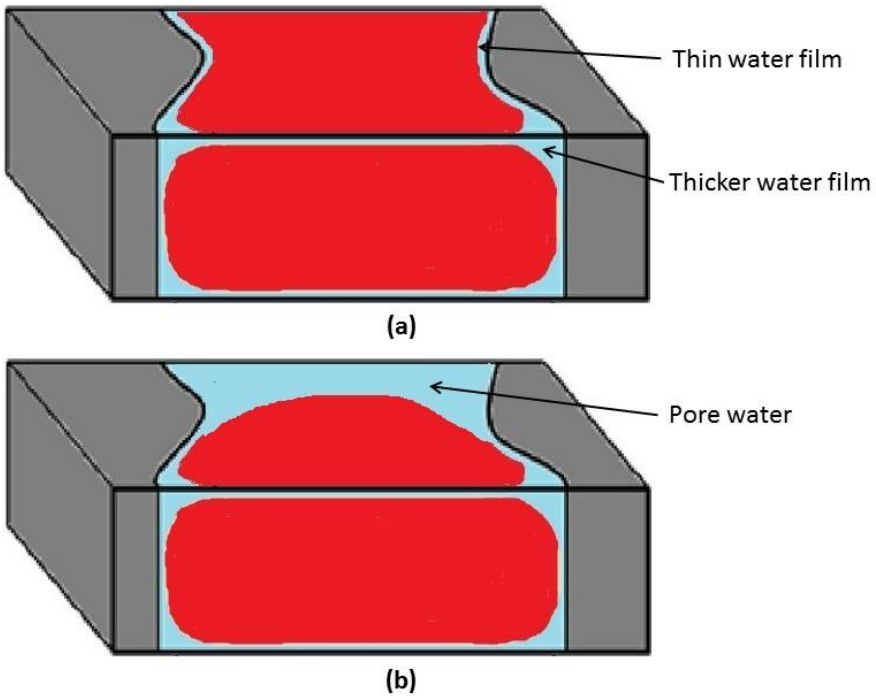

Figure 4.13. A schematic of a pore occupancy by continuous gas (a) and isolated gas (b). Water availability is limited in the pore filled with continuous gas, whereas the isolated gas bubble has an excess to pore water. The pore shapes are modified from Hauge et al. (2016).

In some cases, the development of crystalline hydrate was also observed in the initially water-filled pores where water was partially displaced by gas. Unlike hydrate films/shell growth around continuous gas, hydrate formation in the previously water-occupied pores occurred under dynamic conditions, where gas and water were in motion while hydrate films/shell were growing at the interface. This fluid movement ensured continuous surface/interface renewal, which in turn allowed water to permeate through the hydrate films/shell in quantities sufficient to consume the entire gas phase.

Controlling mechanism and hydrate conversion pattern

The nature of crystalline hydrate and hydrate films/shell discussed so far is linked to mass-transport limitations. As pointed out by Almenningen et al. (2018), termination of inward gas consumption and consequent development of hydrate films/shell could also be caused by insufficient pressure inside the gas phase to maintain further growth. In this case, one would expect the development of crystalline hydrate mainly in continuous gas as pressure support is provided by inflow of nearby gas (Almenningen et al., 2017a). On the other hand, isolated gas bubbles would remain unconverted to crystalline hydrate as the developed hydrate films/shell would inhibit any external pressure support. In this work, the opposite was observed and it is therefore reasonable to conclude that the water-transfer was the dominant mechanism controlling total gas conversion to hydrate.

Total gas consumption with following development of crystalline hydrate was also studied with respect to growth pattern. Gas was generally observed to be consumed in the pore center first, with a growth progression toward the pore walls as shown in Figure 4.14. This was likely due to thinner hydrate films/shell with better permeability in the pore center, which in turn improved water diffusion. Prior to total gas consumption, hydrate films/shell seemed to be thicker along the pore walls and thinner in the pore center, probably due to higher water accessibility in the pore corners. Water diffusion is favored through the thinner hydrate films/shell in the pore center, resulting in a gas consumption pattern from the pore center towards the pore walls. Figure 4.15 illustrates a possible cross-sectional schematic of this process.

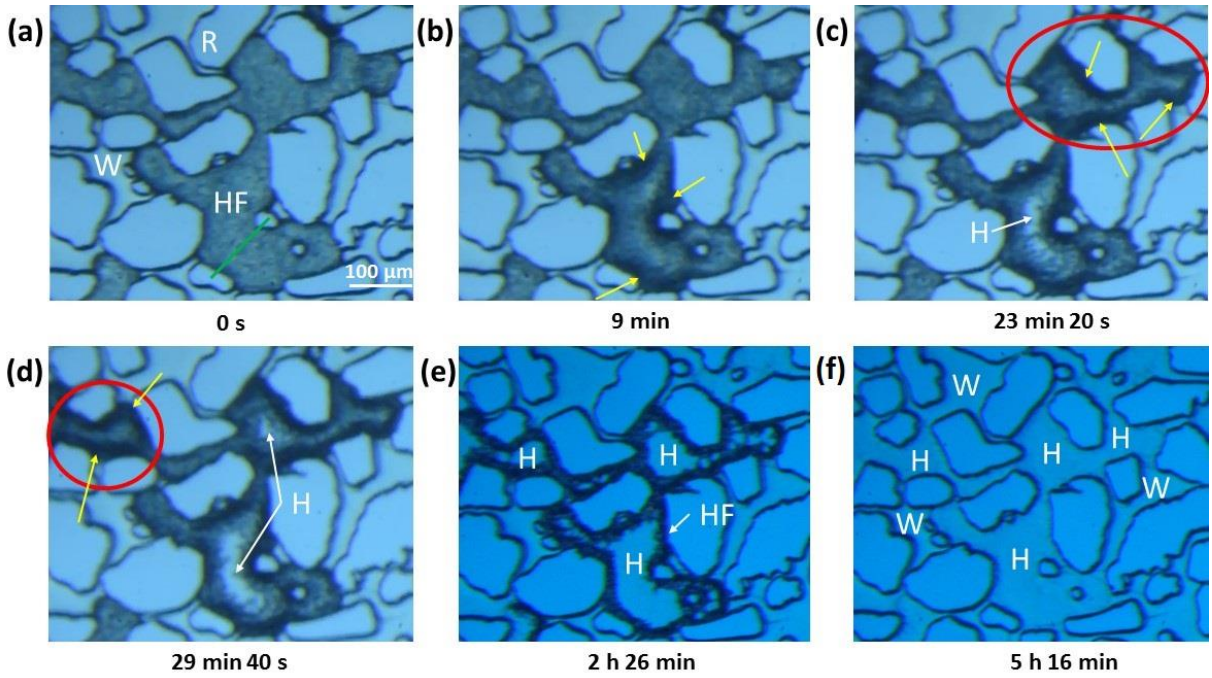

Figure 4.14. Transformation of hydrate films/shell to crystalline hydrate due to total gas consumption in experiment 7_SEC_4. (a) Gas is enclosed by hydrate films/shell (HF). (b) The yellow arrows denote the location along the grains where hydrate films/shell darken, suggesting the thickening of hydrate films/shell. (c) Hydrate films/shell transform to crystalline hydrate (H) in the middle of the pore due to gas consumption. Hydrate films/shell thicken along the pore walls in a new pore (red circle). (d) Crystalline hydrate (H) continues to grow in the middle of the pores. A red circle indicates the hydrate films/shell thickening in a new location. (e) Transformation of hydrate films/shell (HF) to crystalline hydrate (H) occurs from the pore center towards the pore walls. (f) Gas is completely consumed and the hydrate phase is represented by crystalline hydrate (H) only, surrounded by water (W).

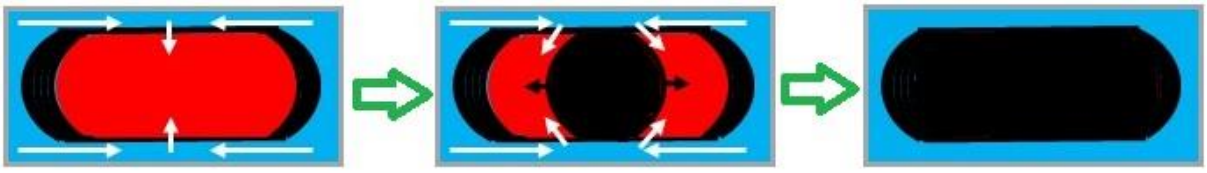

Figure 4.15. The cross-sectional schematic of gas consumption (red) encapsulated by hydrate (black). Water (blue) migrates through wetting water films and permeates through the thinner hydrate films/shell in the pore center (white arrows). Gas is consumed in the pore center. As a result, crystalline hydrate develops in the pore center and further gas consumption continues towards the pore walls (black arrows) until the gas phase is totally converted to hydrate.

To summarize, total gas conversion to hydrate was governed by water transport through wetting water films to the pore center and diffusion through hydrate films/shell. Both processes are time-consuming and therefore gas consumption could last for up to several hours. In contrast, the hydrate film along water-gas interface usually grew within several seconds interval. In a few cases, gas consumption could initiate at the vertical water-hydrate interface rather than in the middle of the pores. This pattern was mainly observed in the pores filled with isolated gas bubbles, likely due to sufficient amount of water surrounding the hydrate films/shell. In this case, water can permeate through the hydrate films/shell before the hydrate total solidification and therefore consume the gas phase.

The gray scale profiles of the pore space marked by a green line in Figure 4.14a were plotted for the same six time intervals (from images a to f) using ImageJ software (Figure 4.16). Two vertical black lines separate the grain surface from pore space filled with hydrate. Six dashed curves represent the color change in the hydrate texture during the conversion to crystalline hydrate, where the gray scale value

increases with decreasing darkness. High gray scale values indicate the transparent hydrate texture (crystalline), whereas black hydrate (films/shell) is related to low gray scale values. The black dashed curve (t_1) corresponds to hydrate films/shell, whereas the green curves relate to the crystalline hydrate (t_5 and t_6). The yellow curves represent the time intervals when the pore was filled with both crystalline hydrate and hydrate films/shell. Drop in a gray value shown by two red vertical arrows indicates the darkening of hydrate films/shell along the pore walls, whereas the increase in gray value represented by a black vertical arrow denotes the development of crystalline hydrate in the pore center. The curves for t_5 and t_6 flatten indicating the conversion from black hydrate films/shell to transparent crystalline hydrate in most of the pore space. Two horizontal blue arrows show the conversion pattern from the pore center towards the pore walls.

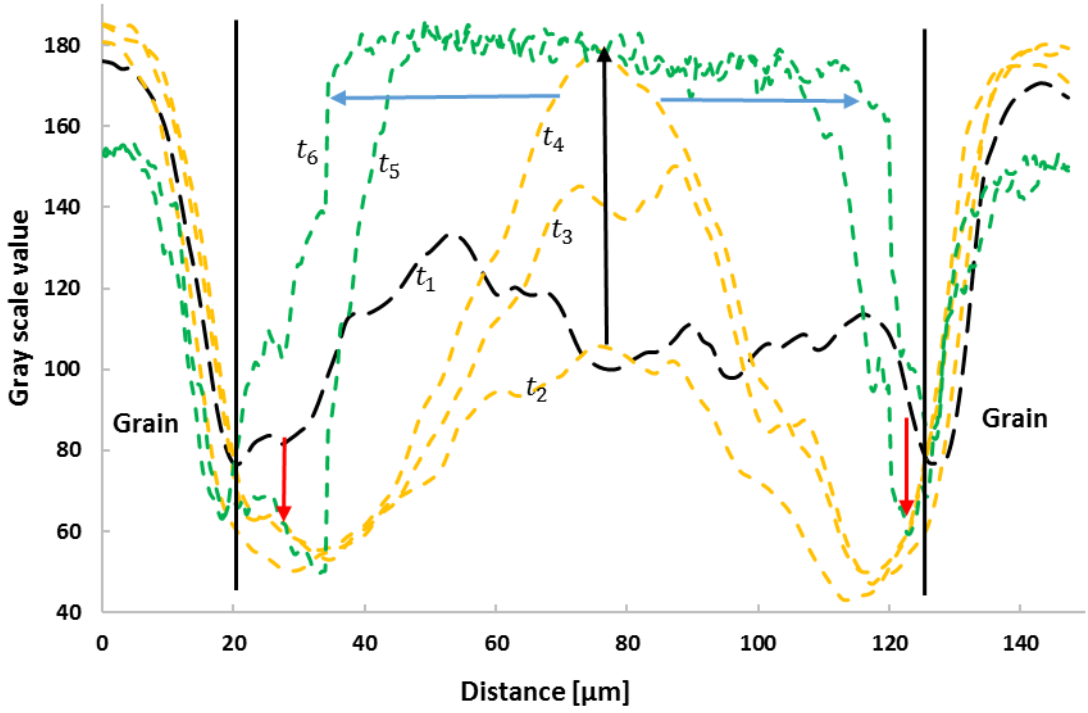

Figure 4.16. Gray scale profile of the pore space along a green line defined in Figure 4.14a at the same time intervals as in Figure 4.14. The dashed curves for t_1, t_2, t_3, t_4, t_5 and t_6 correspond to the images (a), (b), (c), (d), (e) and (f) respectively. The dashed curves are colored differently and represent the hydrate films/shell (black), crystalline hydrate (green) and the combination of both (yellow). Two black vertical lines separate the grain surface from the pore space filled with hydrate.

Cementation

Tohidi et al. (2001) and Katsuki et al. (2007) who examined the hydrate behavior at pore-scale reached opposing conclusions on the cementing nature of gas hydrates. Tohidi et al. (2001) claimed that gas hydrates were unlikely to cement the grains, whereas Katsuki et al. (2007) reported grain cementation by hydrates. However, Katsuki's conclusion was based on the inability to detect the water wetting films coating the grains due to insufficient resolution. There is no general agreement among the researchers on whether the gas hydrates that are separated from grains by a thin water wetting film can be considered as grain cementing.

Thin water films coating the grains were not detected due to the limitation of resolution (less than 4 µm); although they were assumed to exist due to the water-wet nature of the grain surfaces and lower activity of the bound water (Clennell et al., 1999). Wetting water films between water ice, a solid phase with strong similarities to gas hydrate - and a silica surface can be as thin as 5-50 nm (Churaev et al., 1993). Such thin wetting films are significantly thinner than the microscope resolution. Two hydrate

configurations observed in this work (crystalline and films/shell) are certainly pore filling; however, the degree of cementation is unclear, but will depend on both growth pattern and initial saturation.

As the wetting water films were not observed within the limit of resolution, both hydrate configurations seemed to contact the grains. From the hydrate distribution models described by Ecker et al. (1998), it is unclear whether the observed configurations (crystalline and films/shell) can be defined as contact/grain cementing. It is therefore assumed that crystalline hydrate and hydrate films/shell are partly cementing, meaning that the hydrate phase resides on the grains but does not necessarily directly attach to the grain surface due to wetting water films. Both hydrate configurations accumulate in the entire pore space in two-dimensional view and thus can also be considered as pore filling. To summarize, two extreme hydrate models (grain cementing and pore filling) cannot precisely describe the hydrate configurations observed in this work. More specific definitions are needed to accurately represent the hydrate distribution in naturally occurring systems. For natural systems, the degree of cementation will also vary with lithology and the degree of consolidation.

4.1.3 Massive hydrate growth in water

Massive growth of hydrate crystals in water was not a common observation due to poor solubility of methane. Progressive hydrate growth in water was only achieved as a result of several secondary formation-dissociation cycles with gradually decreasing temperature. Neither Tohidi et al. (2001) nor Hauge et al. (2016) observed crystal hydrate growth in water. However, Katsuki et al. (2007) reported progressive hydrate growth in water, which was accomplished by presaturating water with methane at temperatures close to the triple gaseous methane-hydrate-liquid water equilibrium temperature. In this work, methane was dissolved in water directly in the porous media. This experimental procedure supports the proposed mechanism of hydrate accumulations due to in-situ dissolution of methane (section 1.1). In nature, where processes work within geological time scales, gas hydrates may dissociate and form under temperature and pressure variations, thereby charging the pore water with methane. In present work, the applied procedure to dissolve methane in water may reproduce real geological processes occurring in hydrate systems.

Hydrate crystals massively grew in water in experiments 8_SEC_6 and 8_SEC_8, indicating that water-reached superasturation as a result of forced dissolution of methane. Hydrate growth seemed to initiate in water and gas almost simultaneously. However, it is unclear whether the hydrate growth initiated in the free gas phase itself or the moving hydrate front (from outside the field of view) converted the free gas to hydrate. Figure 4.17 illustrates the hydrate growth in water observed in experiment 8_SEC_6. Initial hydrate growth was not restricted to a certain location but occurred in several water-filled pores almost simultaneously, suggesting that the concentration of dissolved methane was the highest in these pores. The resulting local hydrate fronts then merged into a larger rapid-moving front propagating through porous network at around 25 µm/s (subcooling of 13.6 °C). The formation rate is approximately two times slower compared with the hydrate growth in water saturated with carbon dioxide reported by Tohidi et al. (2001) (55 µm/s for subcooling of 9 °C), likely due to lower methane solubility in water compared with carbon dioxide. Upon movement, the hydrate formation front converted the isolated gas bubbles to hydrate. Some water-filled pore clusters were bypassed by hydrate front, and hydrate did not form in these pores. The associated hydrate morphology had a heterogeneous texture with intersecting parallel ridges, similar to morphology observed by Tohidi et al. (2001) for carbon dioxide hydrate growth in water. However, such hydrate crystals disappeared within several hours, suggesting the redistribution and change in morphology. The pressure was then reduced to study the phase behavior in the system (Figure 4.19). Upon pressure reduction, gas bubbles evolved from solution at pressure approximately 20 bar higher than the equilibrium pressure ($p_{eq}(T_{sys}) = 26.2$ bar from Colorado School of Mines, 2009), indicating that

hydrate crystals had dissociated before, with methane remaining in the system in dissolved state. The released gas bubbles were converted to hydrate and dissociated when the pressure was further lowered below the equilibrium value.

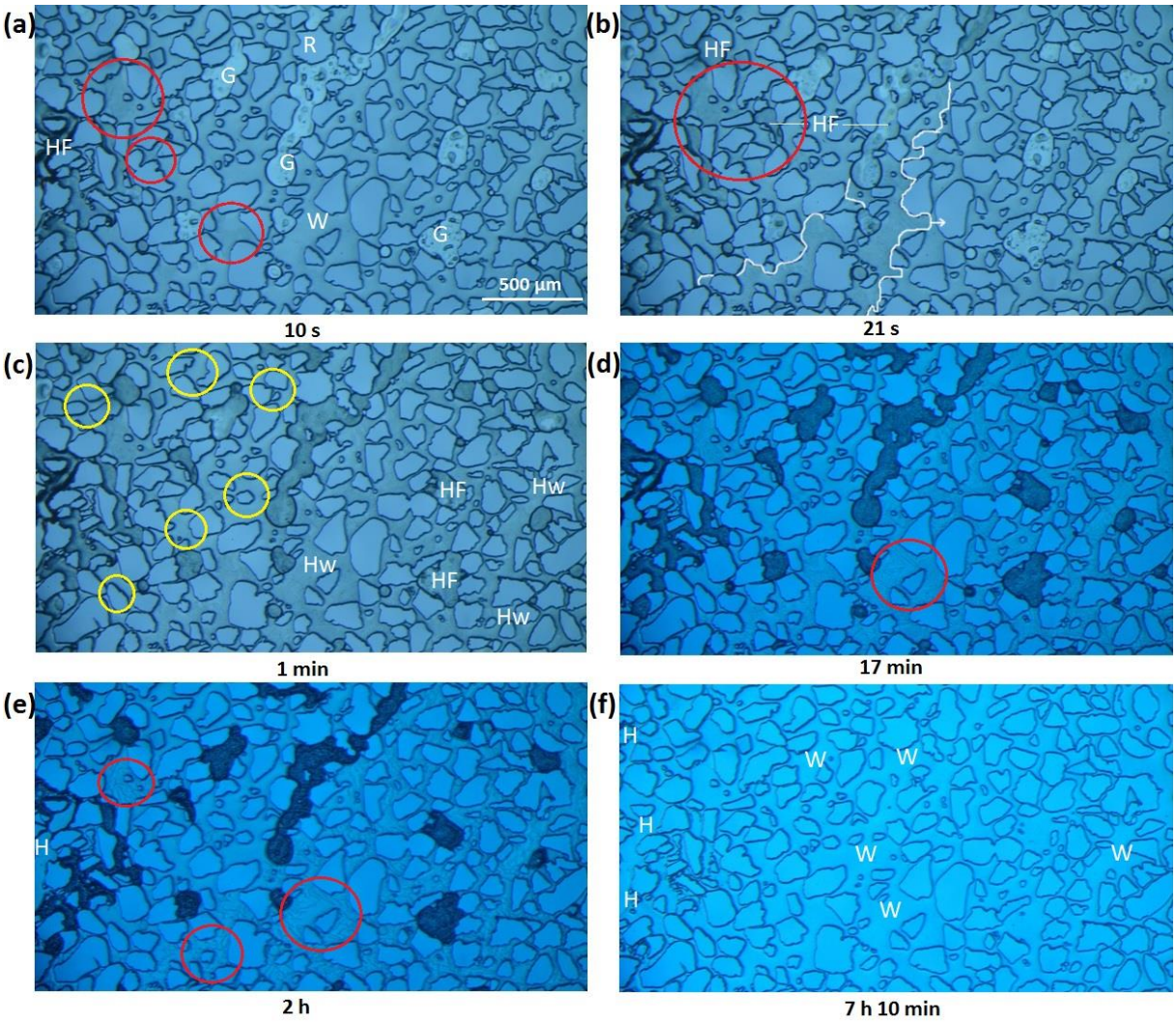

Figure 4.17. Massive hydrate growth in the water phase observed in experiment 8_SEC_6. (a) 10 s after the hydrate growth initiated in the field of view. Hydrate films/shell (HF) encapsulate the gas phase. At the same time, hydrate grows in water at several locations almost simultaneously (red circles). Water (W) and gas (G) are present in the model. (b) Hydrate films/shell (HF) develop around gas when the propagating hydrate front (in water) meets the gas phase. Hydrate terminates to grow in water in the area marked by a red circle. The hydrate front in water (denoted by white curves) grows to the right. (c) All gas bubbles are encapsulated by hydrate films/shell (HF). The entire water phase is converted to hydrate (Hw) in the right part of the image. The yellow circles show the water-filled pores, which were not converted to hydrate. (d) Hydrate phase grown in water has a rough morphology with intersecting parallel ridges. The area marked by a red circle is magnified in Figure 4.18 to illustrate the hydrate morphology. (e) Intersecting ridges begin to vanish, likely indicating the redistribution and change in morphology. (f) All hydrate crystals grown in water disappear and most of the pore space is occupied by water. Crystalline hydrate (H) developed from free gas phase remains in the left part of the image.

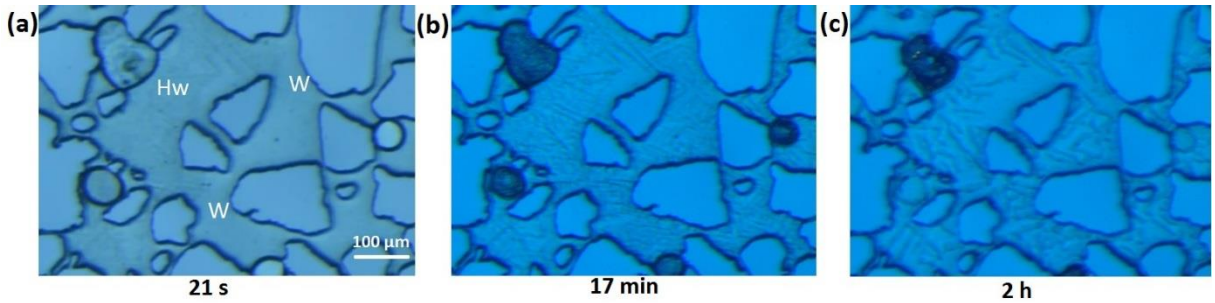

Figure 4.18. Magnified images of the area shown by a red circle in Figure 4.17d. (a) Illustration corresponds to Figure 4.17c. Interface boundary between hydrate front (Hw) and water (W). (b) Magnification of Figure 4.17d demonstrating the rough nature of hydrate crystals with intersecting parallel ridges. (c) Change in morphology as shown in Figure 4.17e. The ridges vanish, likely indicating the dissociation of crystals.

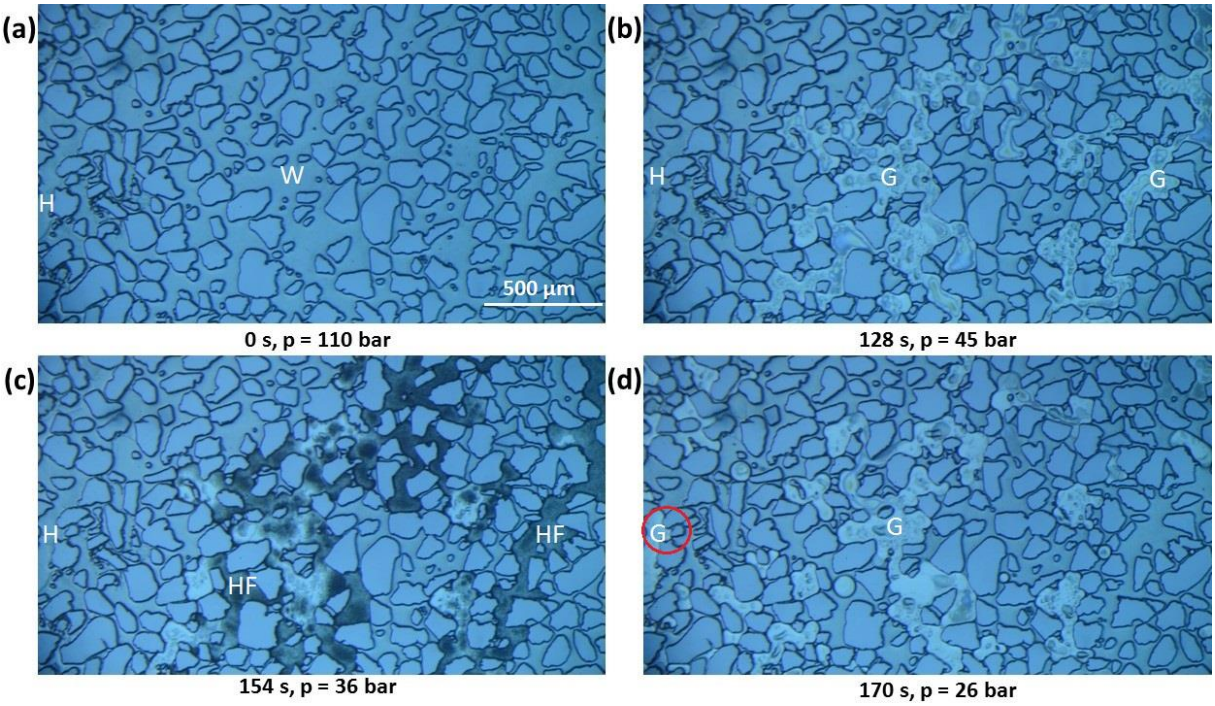

Figure 4.19. Pressure reduction in experiment 8_SEC_6. (a) Water (W) occupies almost the entire pore space, whereas some crystalline hydrate (H) reside in the previously gas-filled pores. (b) When pressure is reduced to 45 bar, which is approximately 20 bar higher than the equilibrium value, gas liberates from water and then (c) is enclosed by hydrate films/shell (HF). (d) Hydrate dissociates when pressure is outside the hydrate stability zone, including the crystalline hydrate formed in the initially gas-filled pores (red circle).

In this thesis, the observed unexpected dissociation of hydrate crystals may be explained by the undersaturation of methane in water. The massive formation of hydrate crystals occupying significant fraction of the pore space likely consumed most of methane dissolved in water. As a result, the remaining water (yellow circles in Figure 4.17c) became undersaturated with methane. According to Kvamme et al. (2016), the hydrate may re-form or dissociate through contact with phases undersaturated with hydrate formers. The direct contact between undersaturated water and hydrate might have caused the dissociation of adjacent hydrate crystals. When hydrate dissociated, the concentration of methane-in-water near the hydrate-dissociating area became higher than in the pore water, leading to hydrate dissociation and diffusive transport of dissolved methane in the pore water. As a result, water near the hydrate-dissociating area remained in the undersaturated state, thereby inducing further hydrate dissociation. Another possible explanation of the observed dissociation is related to the total amount of methane-in-water. It can be speculated that the amount of methane

dissolved in water was sufficient to induce hydrate growth, but it was not enough to support the local equilibrium for a prolonged time. This may have led to hydrate dissociation.

4.1.4 Effect of nucleation parameters on hydrate growth

Even though the hydrate growth is primarily influenced by mass- and heat-transfer coupled with intrinsic kinetics (section 1.4.3), many of the nucleation parameters affect the growth process as well. In present work, the nucleation parameters described in section 1.4.2 appeared to influence the methane hydrate formation.

The hydrate formation under static conditions (no flow and constant pressure) was rare and therefore agitation was required to initiate hydrate growth. Fourteen out of fifteen primary hydrate formations were triggered by agitation. Hauge et al. (2016) who utilized similar silicon micromodel also reported the complexities related to the formation of methane hydrate. Despite several pressure pulse agitations, they did not observe the hydrate formation, and temperature reduction was needed to induce the growth. In addition, Tohidi et al. (2001) emphasized the importance of high degree of subcooling for the methane hydrate formation. For comparison, spontaneous methane hydrate growth on core scale usually initiates within a couple of days without agitation (Graue et al., 2008; Baldwin et al., 2009; Ersland et al., 2010). The hydrate formation in micromodels under static conditions are complicated likely due to much smaller pore volume compared with core plugs. Small pore volume inhibits the fluid movement within the system, which sequentially restricts the interface renewal needed to obtain massive growth. Note that the lack of visual evidence for hydrate growth does not necessarily imply the absence of hydrate film. As estimated by Flatlandsmo (2015), hydrate film is detectable within a microscopic view when its thickness exceeds 1.5 μm. It remains unclear whether hydrate films are not observed because of their total absence in the system or due to insufficient microscope resolution.

Induction time varied in this work. In experiment 1, static hydrate growth (no agitation) was detected after two hours of induction time. For comparison, in experiment 7 (similar pressure, temperature and initial water saturation) gas hydrate did not form under static conditions during twenty four days and agitation was forced into the system to promote the growth. Even for agitated systems, induction time ranged from several seconds up to several minutes. The scatter in induction times supports the stochastic nature of hydrate nucleation.

Hydrate formation was also studied with respect to driving force expressed in terms of degree of subcooling. Although high driving forces did not seem to promote the hydrate formation under static conditions, they appeared to affect the hydrate growth rates after the induction time was over (see section 4.2.2). On the other hand, induction time was sufficiently reduced in secondary formation experiments, where hydrates could nucleate spontaneously at lower pressures (lower driving forces) compared with primary formations. Since the system was not heated to a room temperature after previous hydrate dissociation, a relatively rapid onset of the secondary hydrate formations was likely caused by memory effect. The initiation pressure at which the secondary growth occurred appeared to increase with the time elapsed between the previous dissociation and a new secondary formation.

4.2 Hydrate growth rates

The discussion of methane hydrate formation reported in section 4.1 was based on the qualitative results. This section quantitatively investigates the hydrate film and crystal growth in porous media. In literature, hydrate film growth studies at the water-hydrocarbon interface are primarily related to bulk volumes (see section 2.3.1 for a short summary). The first attempt to measure the hydrate film growth in porous media was performed by Hauge et al. (2016) in silicon micromodel but only for one experiment with fixed pressure and temperature conditions. Film growth estimations provide a basis for a model analysis of hydrate growth, which in turn can have practical implications for flow assurance both in processing engineering (rate at which hydrates plug pipelines) and in gas production industry (rate of hydrate formation near a production well). A systematic understating of hydrate film growth with adjustments to porous systems is needed. This work investigates the effect of initial water saturation, pore sizes and driving force (degree of subcooling) on hydrate film growth rate.

Section 3.3.1 provides a detailed description of the procedures for hydrate growth measurements. Whereas the propagation rate of hydrate crystals in the water phase was roughly approximated only for a few experiments, the hydrate film growth at the water-gas interface was systematically studied with respect to initial water saturation, pore sizes and driving force (degree of subcooling). At the water-gas interface, hydrate film was observed to propagate at different velocities depending on the growth direction. Both pore wall and pore center growth rates were measured in several locations and were then averaged, with the uncertainty represented by standard deviation.

Figure 4.20 and Figure 4.21 show a typical example of the hydrate growth analysis. Different locations at which hydrate grew were selected within the field of view. The distance travelled by hydrate front with respect to a certain point on the grain surface was then listed at different time intervals for each location. The data points were plotted on a graph of distance (μm/s) vs time (s) for each location and showed a linear trend. A best-fit line was applied, with the gradient representing the growth rate, v.

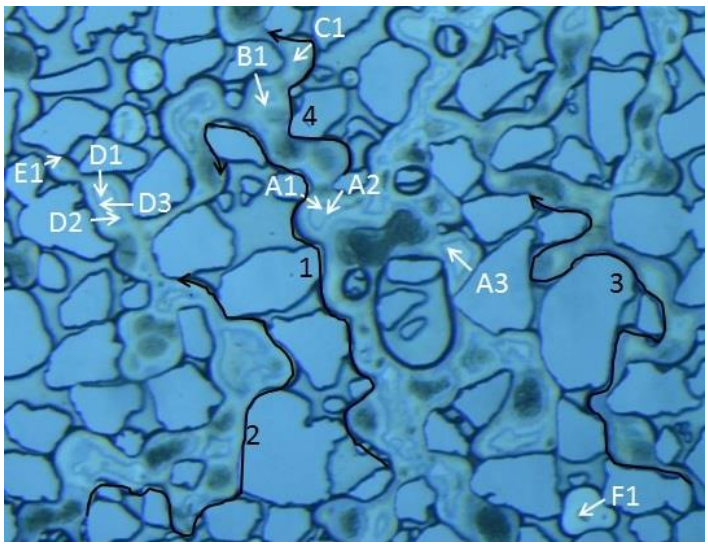

Figure 4.20. Locations of measured hydrate growth in experiment 4. The arrows denote the direction of pore center growth (white) and pore wall growth (black).

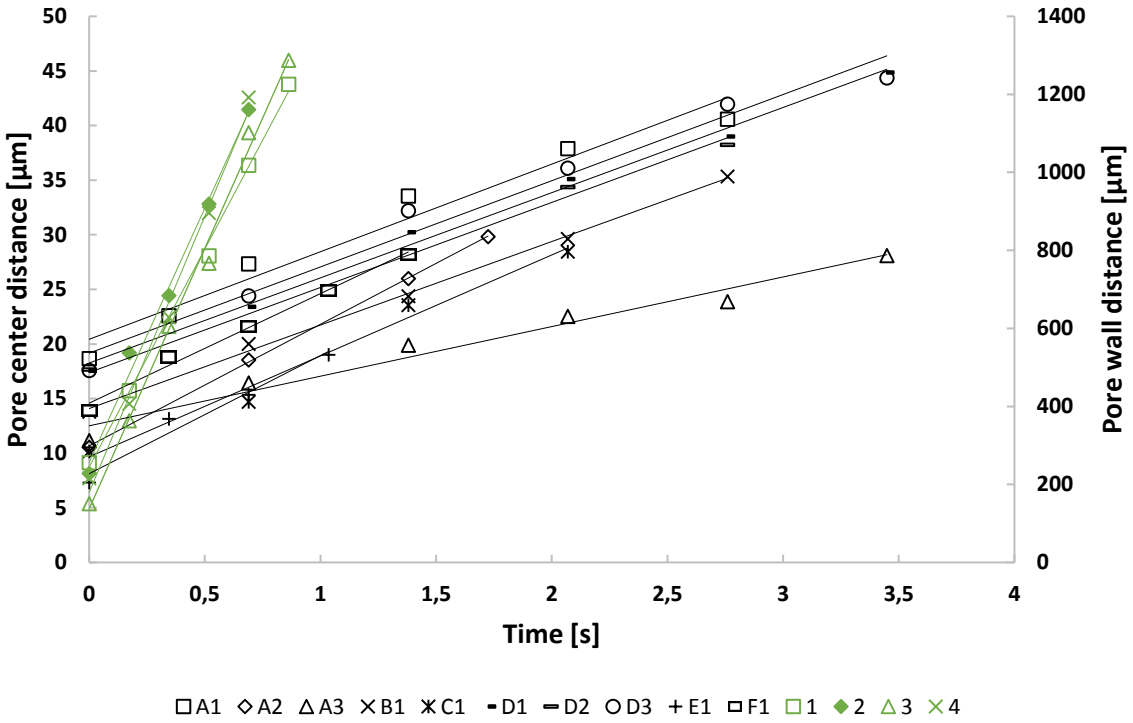

Figure 4.21. A graph of distance vs time for pore center growth (black) and pore wall growth (green) for locations defined in Figure 4.20. A linear fit was applied to all data points, with the slopes representing the growth rates. The intersections with the y-axis indicate the initial distance propagated by hydrate front.

Table 4.3 reports the estimated growth rates for each location.

Table 4.3. Hydrate growth measurements in experiment 4 for locations defined in Figure 4.20 and estimated from Figure 4.21 as the slope values. R^2-values are provided to demonstrate a good applicability of linear fit to data points.

Pore center growth			Pore wall growth		
Location	v [µm/s]	R^2	Location	v [µm/s]	R^2
A1	8.0	0.9623	1	1117	0.9971
A2	11.2	0.9997	2	1303	0.9910
A3	4.5	0.9693	3	1336	0.9937
B1	7.6	0.9976	4	1417	0.9922
C1	6.3	0.9836			
D1	7.8	0.9937			
D2	7.8	0.9921			
D3	7.9	0.9764			
E1	10.8	0.9651			
F1	10.0	0.9911			
Average	8.2			1290	
Uncertainty	2.0			130	

4.2.1 Effect of initial global saturation and pore sizes

The influence of initial water saturation and pore sizes on the hydrate growth rate was investigated in primary formation experiments 1-7 where pressure and temperature conditions remained nearly constant, whereas initial water saturation in the entire micromodel (global saturation) lied between 0.3 and 0.6. Table 4.4 summarizes the hydrate growth measurements performed for experiments 1-7.

The hydrate growth rates were mainly estimated in the continuous gas phase, and only few measurements were performed in the isolated gas bubbles. Pore center growth was typically measured in three to five locations for each pore type (small, medium and large as defined in Table 3.1), except for experiments 1 and 7 where only two pore types were studied because gas did not occupy all pore sizes. The growth rates, v, were then averaged for each pore size type and the uncertainty, Δv, was estimated as standard deviation of all measurements.

Table 4.4. Summary of growth rate measurements for experiments 1-7. Growth rates, v, their uncertainty Δv, and total number of locations where the hydrate growth was measured, *n*, are provided. The total average values were estimated based on all single measurements for each growth type.

		Pore center growth			Pore wall growth			Growth in water		
Exp.	Pore size	v [μm/s]	Δv ±	*n*	v [μm/s]	Δv ±	*n*	Rate [μm/s]	Δv ±	*n*
1	Medium	2.7	0.9	4						
	Large	3.2	0.7	3						
	Average v	2.9	0.8	7	680	70	3			
2	Small	2.5	0.9	3						
	Medium	2.1	0.8	3						
	Large	1.7	1.0	3						
	Average v	2.1	0.9	9	1330	200	3	0.14		1
3	Small	13.5	1.3	3						
	Medium	14.2	2.0	4						
	Large	15.4	3.8	4						
	Average v	14.4	2.5	11	1090	370	4	0.18	0.08	4
4	Small	8.6	2.3	2						
	Medium	8.2	1.0	5						
	Large	7.9	3.3	3						
	Average v	8.2	2.0	10	1290	130	4	0.53	0.46	3
5	Small	7.2	1.4	3						
	Medium	6.8	2.2	5						
	Large	4.9	1.0	3						
	Average v	6.4	1.9	11						
6	Small	8.0	1.5	4						
	Medium	6.1	1.4	3						
	Large	5.6	2.8	3						
	Average v	6.7	2.0	10	1280	220	3	0.21	0.10	3
7	Small	10.0	2.1	5						
	Medium	10.5	1.5	5						
	Average v	10.3	1.8	10	1150	130	3			
Total average v		8	4	125	1100	300	20	0.3	0.3	11

The relationship between pore center growth rate in distinct pore sizes and initial global water saturation is shown in Figure 4.22 for each experimental run. No clear trend between pore sizes and growth rate was noticed. The fastest growth rate was observed in the largest pores in two experimental runs; one time in the medium-size pores; and four times in the smallest pores. The difference in growth rates between different pore sizes did not typically exceed the limit of uncertainty. It can therefore be concluded that the pore sizes have no clear effect on the hydrate growth rate, which is consistent with Sloan and Koh (2008) and Kang et al. (2009). However, pore sizes of the same magnitude were examined in this work. To draw a more general conclusion regarding the influence of pore sizes on growth rate, different rock types with more heterogeneous pore-size distributions should be studied as they will cover pore sizes of different orders of magnitudes.

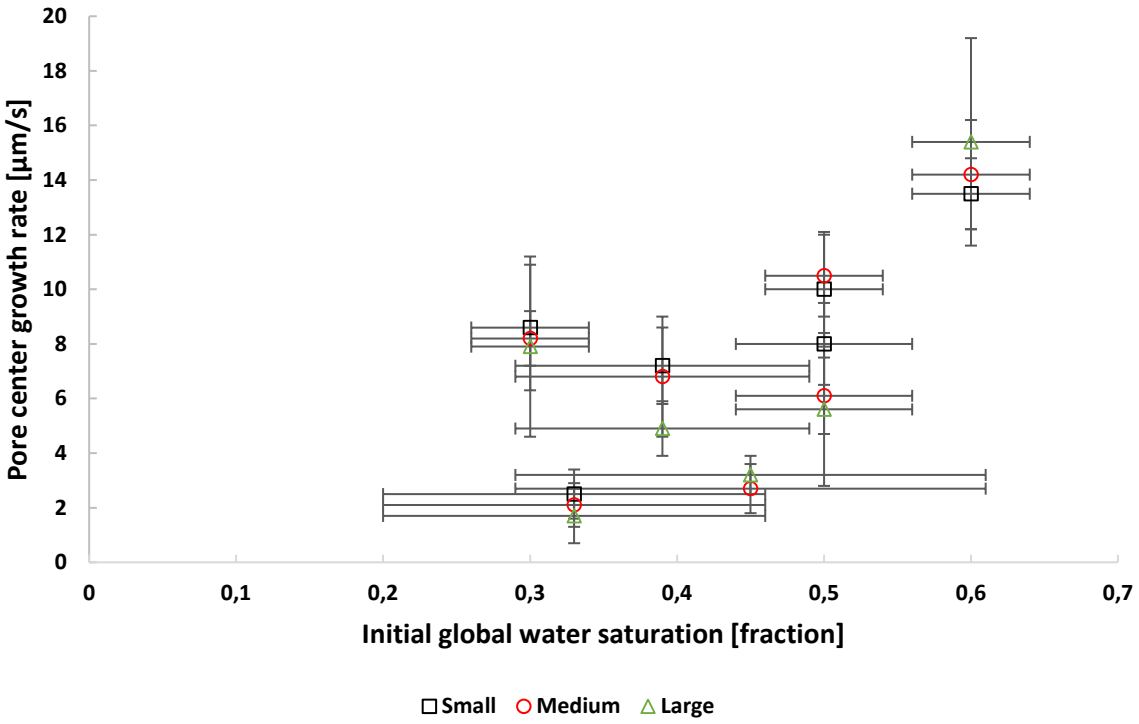

Figure 4.22. A relationship between pore center growth rates and initial global water saturation for small (black), medium (red) and large (green) pores as reported in Table 4.4. Initial global water saturations are provided in Table 4.1.

To investigate the effect of initial global water saturation, pore center growth rates were averaged for all pore sizes and plotted on Figure 4.23. No clear trend was observed. Both linear and power law trends showed a poor correlation. The effect of initial water saturation was also studied with respect to pore wall growth, which was usually measured in three to four locations for each experiment. In experiment 5, pore wall growth was not studied because of poor quality data. The smaller number of single measurements compared with pore center growth is due to generally higher visual uncertainty in estimation method (see section 3.3.1). Looking at Figure 4.24, it can be seen that pore wall growth rate and initial water saturation were poorly correlated. The majority of points lied between 1000 and 1400 µm/s, with only one point outside this range. By removing the outlier from the graph, a relationship between the remaining points is significantly improved, but the correlation is still weak. In summary, no clear trend between hydrate growth rate and initial global water saturation was observed. This conclusion is only valid for a limited range of water saturation. It was difficult to attain end-point water saturations in the entire micromodel. Water saturation below 0.3 was not achieved due to capillary-trapped water residing in the smallest pores after gas flood. At water saturations

exceeding 0.6, gas was completely dissolved after cooling as the methane solubility in water increases with decreasing temperature.

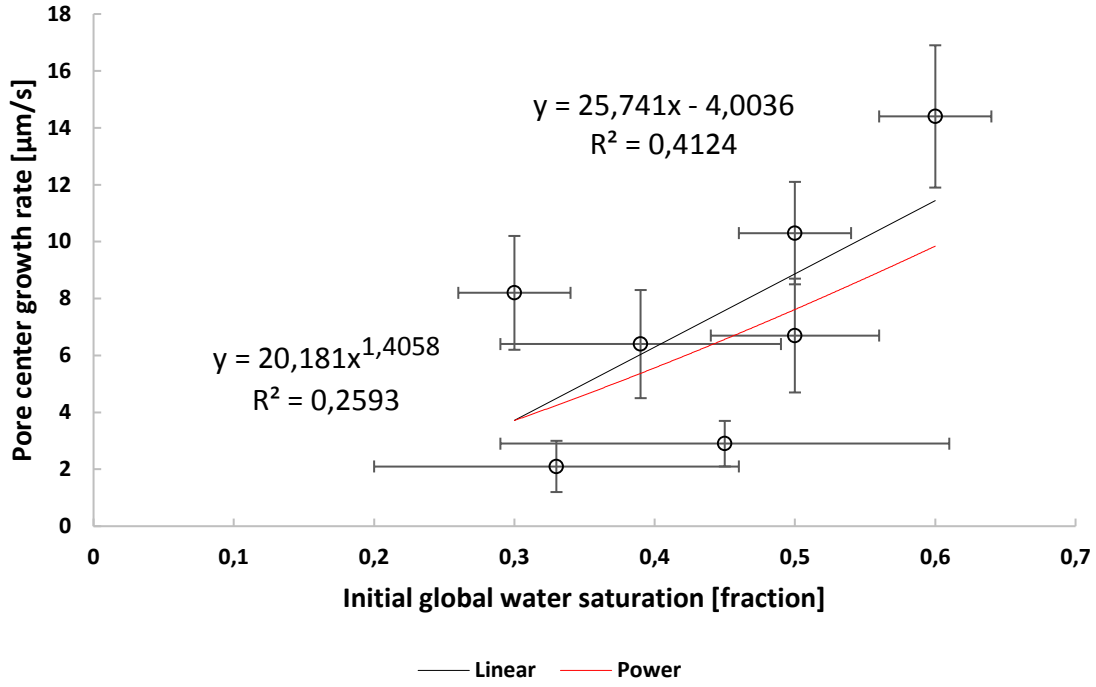

Figure 4.23. The effect of initial global water saturation on the pore center growth rates. Data points on y-axis represent the average values calculated for all pore sizes as reported in Table 4.4. Both linear (black) and power law (red) trends show a poor correlation.

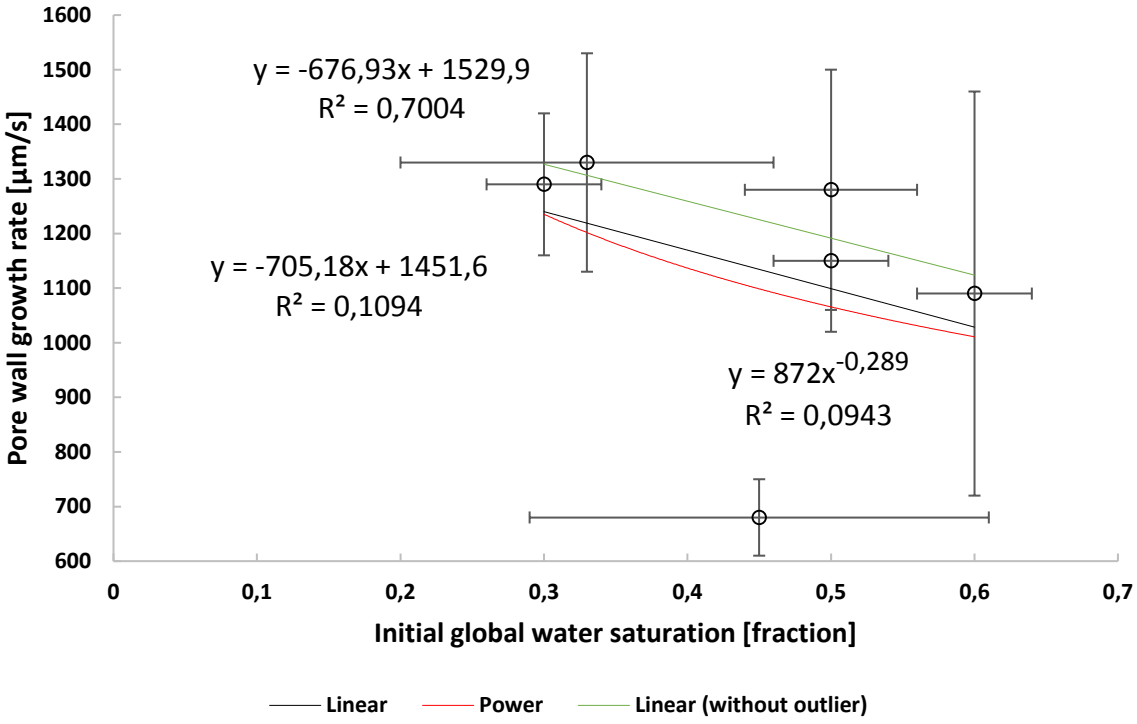

Figure 4.24. The effect of initial global water saturation on the pore wall growth rates as reported in Table 4.4. No clear trend emerges. The linear trend is improved by removing the outlying data point but the correlation is weak.

Investigation of hydrate growth rates with respect to water saturation has two main limitations. First, initial global water saturation was determined based on five images generated in different parts of the micromodel, with totally covered area of approximately 5%. In some experiments, water saturation varied significantly as a result of uneven displacement by gas, resulting in the uncertainty greater than 0.1. Second, effect of agitation on fluid saturation was not investigated. In experiments 2-7 where agitation was needed to initiate the growth, water saturation had been calculated before the system was agitated. The hydrate formation could occur within several seconds after agitation, and the system was set to video recording prior to agitation as it would later allow to perform the estimations of hydrate growth rate. It was therefore not practical to move the microscope after agitation in order to collect new images because it could result in a failure to record the onset of hydrate growth. It is unclear whether agitation had a significant impact on global fluid saturations.

The quantitative results support the visually proposed conclusion of much faster hydrate film growth along the pore walls at the water-gas interface compared with growth towards the pore center. As discussed before, this significant difference in growth rates was likely caused by mass-transfer limitations through the wetting films towards the pore center (see “Hydrate growth at the water-gas interface in the continuous gas phase” in section 4.1.1). The growth of hydrate crystals in water was not systematically examined with respect to pore sizes and fluid saturations due to its rare occurrence. Estimates of hydrate growth in water are listed in Table 4.4, which shows that growth of hydrate crystals in water had the slowest rate, likely due to slow methane-transport to the hydrate-forming area.

4.2.2 Effect of driving force

The relationship between hydrate growth and driving force expressed in terms of degree of subcooling was investigated in this work. Degree of subccoling, ΔT, is defined as the difference between the equilibrium temperature of the methane-hydrate-water system at a given pressure, T_{eq}, and the temperature of the system, T_{sys}. The equilibrium system temperature at a given pressure was estimated using CSMGem (Colorado School of Mines, 2009). The studies of growth rates with respect to degree of subcooling provide a foundation for a modelling of hydrate film growth. Hydrate growth models have been proposed for bulk systems (Freer et al., 2001; Peng et al., 2007). This work is aimed at investigating the influence of driving force on hydrate growth rates in porous media. Hydrate film growth was studied with respect to degree of subcooling for both pore wall and pore center growth as reported in Table 4.5.

Table 4.5. Overview of average hydrate rates, v, at the water-gas interface for all experiments where the rates were measured. Δv and *n* represent the uncertainty in v and total number of measurements respectively.

Exp.	T_{eq} [°C]	ΔT [°C]	Pore center growth			Pore wall growth		
			v [µm/s]	Δv ±	n	v [µm/s]	Δv ±	n
1	11.3	10.1	2.9	0.8	7	680	70	3
2	11.3	10.0	2.1	0.9	9	1330	200	3
3	11.4	10.2	14.4	2.5	11	1090	370	4
4	11.3	10.1	8.2	2.0	10	1290	130	4
4_SEC_1	8.2	7.1	8.2	3.6	7	570	50	3
5	11.3	9.9	6.4	1.9	11			
6	11.3	10.0	6.7	2.0	10	1280	220	3
7	3.8	10.0	10.2	1.8	10	1150	130	3
7_SEC_2	3.8	2.5				100	10	3
7_SEC_10	10.3	9.0	11.4	2.6	15	1020	220	3
8	14.1	9.2	8.5	2.2	13			
8_SEC_4	4.3	4.2	2.8	1.3	12	190	40	3
8_SEC_7	3	2.4	1.8	0.7	10	80	15	5
9	7.8	6.4	3.5	1.9	7	450	40	3
10	5.7	4.2	1.7	0.7	7	220	20	5
11	5.7	4.1	1.7	0.5	7	180	10	5
12	4.8	3.3	1.2	0.4	7	100	20	5
13	6.9	5.4	1.5	0.7	7	270	10	5
14	9.3	7.8	2.7	1.0	8	590	60	5
15	12.9	11.4	3.6	2.2	7	1460	70	5

The pore center growth rates generally appeared to increase with increasing degree of subcooling but the relationship is weak (Figure 4.25). This can be caused by several factors. First, it may indicate that the hydrate film growth towards the pore center is more dependent on the slow water-transport through wetting water films rather than on the driving force. It is unclear whether higher subcooling enhances the water-transport towards the pore center. Second, pore center growth could be affected by agitation. In some cases, the system had to be agitated more than once to promote the hydrate growth. Agitation resulted in fluid redistribution within the model and consequent interface renewal, which in turn might have improved the transport of water towards the pore center. Third, pore center growth generally showed a greater scatter within a single experimental run, indicating that the rates varied for each location. The pore center growth could be accelerated by additional water supply provided by the presence of water droplets below the gas phase and/or by adjacent water-filled pores. The relationship between primary and secondary formations is not clear and more data are needed to investigate this effect.

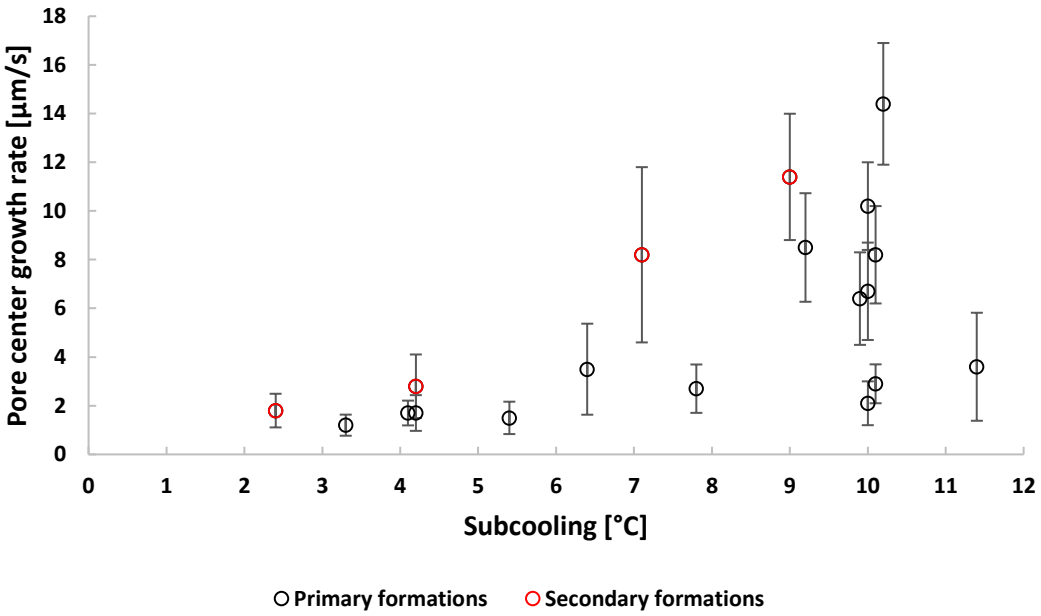

Figure 4.25. A graph of pore center growth rate vs time for the measurements provided in Table 4.5. Growth rate appears to increase with subcooling but the data points are weakly correlated. No clear difference between primary (black) and secondary (red) hydrate formations is observed.

Figure 4.26 illustrates the relationship between the degree of subcooling and hydrate film growth along the pore walls. Similar to hydrate film growth studies in bulk volumes (see section 2.3.1), hydrate film growth was proportional to driving force expressed in terms of subcooling. This observation is also consistent with Kang et al. (2009) who examined the influence of driving force on the hydrate formation rate (gas consumption over time) in silica gel pores. The data points were best-fitted by a power law trend, similar to Taylor et al. (2007) and Peng et al. (2007). There was one data point lying far beyond the best-fit curve [10.1; 677]. By eliminating this point, the fit was slightly improved, with the growth rate being proportional to around ΔT^2 and the R^2 values approximating 0.98. For a given range of data, no clear difference was observed between primary and secondary formations. Memory effect therefore reduces the induction time (section 4.1.4); but has no visible effect on hydrate film growth.

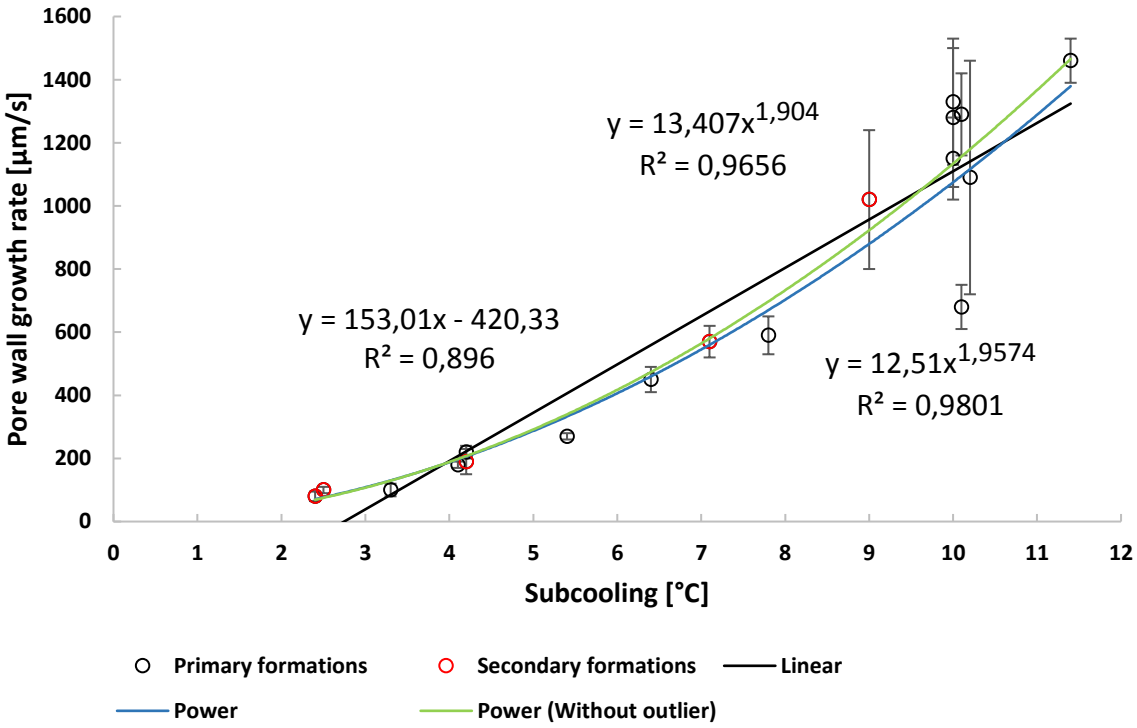

Figure 4.26. Pore wall growth rate as a function of subcooling. Growth rate increases with subcooling, best represented by a power law. The correlation is improved by removing the outlier. No difference between primary and secondary formations is observed.

Figure 4.27 compares the pore wall growth rates obtained in this work with those measured by Hauge et al. (2016). The data point calculated by Hauge et al. (2016) for a similar silicon micromodel fits well into the results of present work. The pore wall film growth is further compared to the measurements of the film growth at the planar water-methane interface in bulk reported by Freer et al. (2001). Although the growth rates in porous media are higher than in bulk, the results are still comparable especially at lower driving forces.

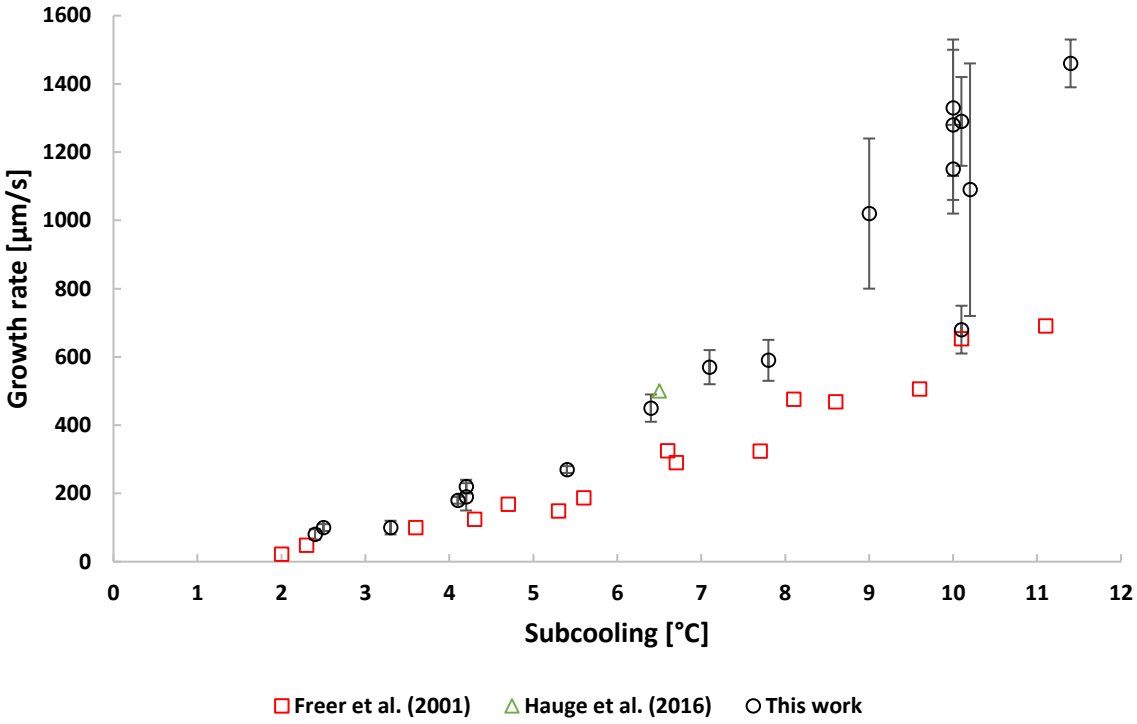

Figure 4.27. Comparison of data with results obtained by Hauge et al. (2016) (green) and Freer et al. (2001) (red). The data point calculated by Hauge et al. (2016) fits well into the results of this work. The values are slightly higher but show the same increasing trend as data provided by Freer et al. (2001).

Apparatus- and/or system-dependency can cause the difference in growth rates. The uncertainty of the visual method was the main limitation of hydrate growth measurements along the pore walls. Water was represented by a very thin film coating the grains, complicating the detection of the pore wall growth. In addition to apparatus-limitation, porous and bulk systems have different properties. The latter does not include the mineral surfaces, which could have led to the observed difference in results. In fact, Kvamme et al. (2007) showed that nucleation and growth of methane hydrate was slower in bulk than in porous media. The measurements reported by Freer et al. (2001) were estimated for a planar water-methane interface. In porous media, the boundary between water and methane has a distinct geometry due to tortuosity. Peng et al. (2007) studied the kinetics of hydrate formed from a single gas bubble suspended in water (non-planar interface, which might better reproduce porous systems) and proposed a model where the growth rate was proportional to $\Delta T^{2.5}$. Unlike Freer et al. (2001), Taylor et al. (2007) reported that a power law best represented hydrate film growth at a planar interface. It is unclear whether the interface geometry has an impact on hydrate growth rates.

The relationship between film growth and degree of subcooling reported so far did not take into consideration the effect of system's temperature. Specifications of subcooling may yield erroneous results, as it represents a simplified measure of the driving force. Most of the experiments were

conducted at temperatures ranging between 1.1 and 1.6 °C, which is typically related to the uncertainty in temperature measurements of ± 0.2 °C. The results obtained at this temperature range were compared to Freer et al. (2001) for $T_{sys} = 1$ and 2 °C; and to Peng et al. (2007) for $T_{sys} = 2.25$ °C and $T_{sys} = 0.25$ °C (Figure 4.28). In addition, data points obtained in present work at ΔT lying within the range of ± 0.2 are merged together to improve the data fit. Note that Peng et al. (2007) did not tabulate the experimental raw data and their growth rates were plotted based on proposed formula for hydrate growth and estimated input parameters. By comparing different curves, it can be seen that the experimental results from this study are slightly higher but in a much better agreement with Peng's model for $T_{sys} = 2.25$ °C (Peng et al., 2007) compared to $T_{sys} = 0.25$ °C and the results reported by Freer et al. (2001). The dependence of film growth rate on subcooling is non-linear and follows a power law in this work as well as in Peng et al. (2007). The results of this work does not therefore allow to postulate whether the hydrate growth proceeded by continuous or step mechanism as discussed in section 1.4.3 (see "General crystal growth mechanism"). Merging of data for similar ΔT did not improve the R^2 values. The best fit of data points is demonstrated in Figure 4.26, where hydrate film growth rate along the pore walls is proportional to ΔT^2 with the R^2 values approaching 0.98. Based on the experimental results reported here, the correlation of growth rate versus subcooling in porous media can be written as follows:

$$v_f = \beta \Delta T^2 \tag{4.1}$$

where v_f is the film growth rate along the pore walls, ΔT is degree of subcooling, and β is the proportionality coefficient. Based on the models proposed by Freer et al. (2001) and Peng et al. (2007), the constant β might be a function of film thickness, heat transfer and growth kinetics as well as properties of the porous media. Film thickness was not quantified in this work due to insufficient microscope resolution.

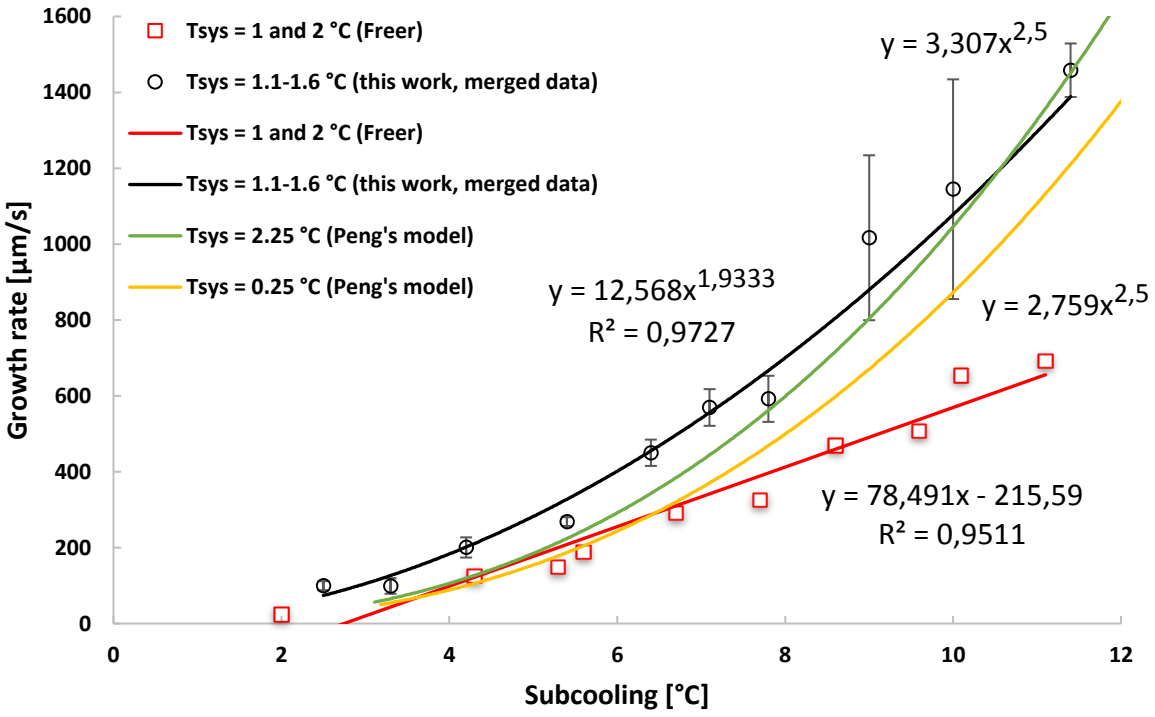

Figure 4.28. Comparison of merged data points obtained in this work with Freer et al. (2001) and Peng et al. (2007) for approximately similar temperature conditions. The Peng's model for $T_{sys} = 2.25$ °C shows a better agreement.

4.3 Hydrate dissociation

The steadily increasing demand for natural gas and gradual depletion of conventional gas resources underlines the importance of alternative gas sources. The growth of natural gas hydrate was assigned to a great attention by a number of different research groups, whereas lack of experimental studies on hydrate dissociation restricts full-scale models of hydrate production schemes in natural reservoirs. The production of gas from methane hydrates can be implemented by various dissociation techniques but all of them face several challenges such as reduced permeability, slope instability and the endothermic nature of hydrate dissociation. This work focuses on the hydrate dissociation by means of depressurization as it is considered as the most cost-efficient production technique (Sloan & Koh, 2008).

Thirty-four hydrate dissociation experiments were conducted in this work, where fifteen experiments related to the dissociation of primary hydrate and the remaining nineteen experimental were performed on secondary hydrate (Table 4.6). The dissociation experiments have the same numbering system as the hydrate formation experiments. The time interval between hydrate formation and dissociation was typically within one to two days. In a few experiments, secondary hydrate was dissociated several hours after the initial formation had been observed. The hydrate dissociation procedure was conducted by lowering the system's pressure several bars below the equilibrium pressure. For experiments 1-6, the system was depressurized by gas pump cylinder, whereas the water pump cylinder was utilized to dissociate gas hydrate in the remaining experiments. Once the initial hydrate dissociation was noticed in the field of view at a given pressure, p_{diss}, the system's pressure could further be reduced to accelerate the hydrate dissociation process.

Table 4.6. Overview of hydrate dissociation experiments.

Primary hydrate			Secondary hydrate		
Exp.	Initial p_{diss} [bar] ±1.4	T_{sys} [°C] ±0.2	Exp.	Initial p_{diss} [bar] ±1.4	T_{sys} [°C] ±0.2
1	8.0	1.2	4_SEC_1	27.0	1.2
2	25.0	1.3	7_SEC_1	27.0	1.3
3	24.0	1.3	7_SEC_2	22.0	1.3
4	27.0	1.2	7_SEC_3	27.0	1.3
5	27.0	1.3	7_SEC_4	10.0	1.3
6	27.0	1.3	7_SEC_5	27.0	1.2
7	27.0	1.3	7_SEC_6	27.0	1.2
8	29.0	2.6	7_SEC_7	27.0	1.2
9	26.0	1.5	7_SEC_9	24.0	1.3
10	26.0	1.5	7_SEC_10	28.5	1.2
11	27.0	1.6	8_SEC_1	20.0	2.6
12	27.0	1.4	8_SEC_2	28.0	1.6
13	27.0	1.5	8_SEC_3	24.0	0.1
14	27.0	1.5	8_SEC_4	24.0	0.1
15	24.0	1.5	8_SEC_5	24.0	0.1
			8_SEC_7	25.0	0.6
			8_SEC_9	23.0	0.6
			8_SEC_10	24.0	0.6
			8_SEC_11	24.3	0.6

4.3.1 Observations of hydrate dissociation mechanisms

Direct visual observations of porous network can provide a valuable knowledge on the mobilization of fluids upon pressure depletion, which in turn can improve a general understanding of hydrate dissociation phenomenon. Pore-scale dissociation mechanisms observed in this work depended on the hydrate pore occupancy. Methane hydrate formed two distinct hydrate configurations: crystalline hydrate and hydrate films/shell with encapsulated gas. These configurations responded differently to depressurization, with respect to both dissociation rate and pattern. The gas from the dissociated crystalline hydrate formed a front that slowly propagated through the pore space, initiating further dissociation of the adjacent hydrate (Figure 4.29a). Katsuki et al. (2008) also observed the flow of gas from dissociated hydrate crystals with a subsequent dissociation of the neighboring hydrate. The hydrate films/shell dissociated more rapidly, with a decomposing pattern from pore center towards the pore walls (Figure 4.29b). Once the hydrate films/shell completely dissociated, the initially enclosed gas mobilized and began to flow through the entire porous network. Almenningen et al. (2018) observed similar dissociation mechanism.

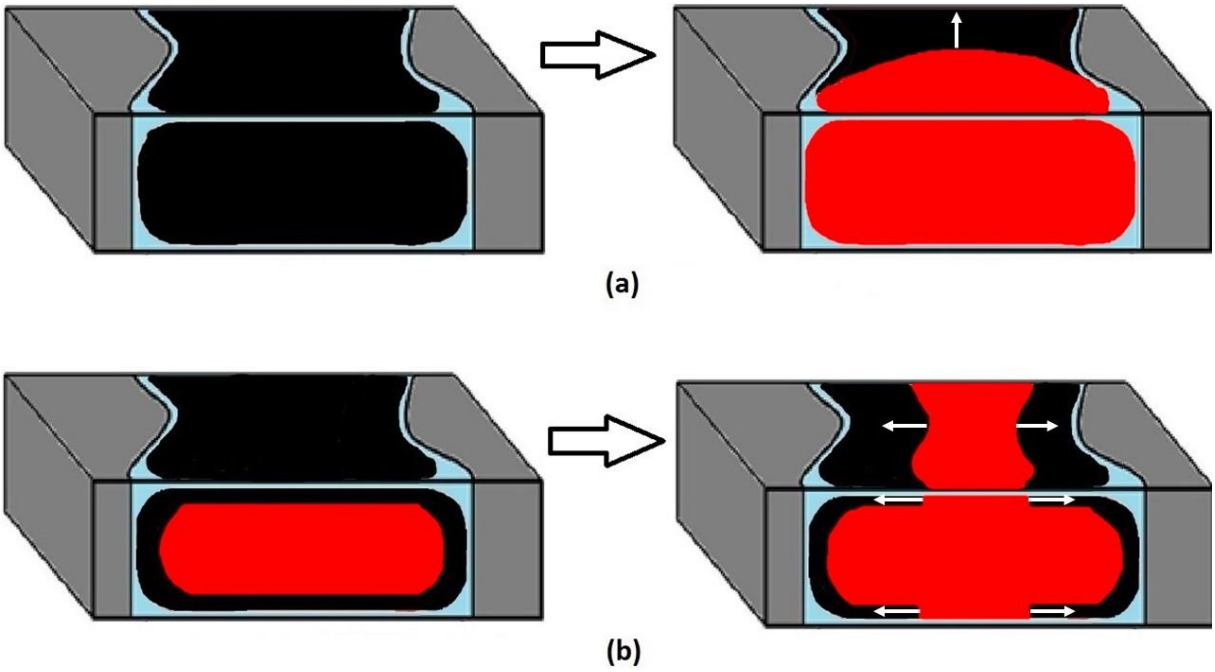

Figure 4.29. Three-dimensional conceptual model of hydrate dissociation in the micromodel with grains (grey), water (blue), gas (red) and hydrate (black) (the pore shapes were modified from Hauge et al., 2016). (a) Dissociation of crystalline hydrate. Left: Pore occupancy prior to hydrate dissociation by pressure depletion: crystalline hydrate (black) and wetting water films (blue). Right: Gas (red) is released upon depressurization. The gas front (marked by a white arrow) propagates through the pore space. (b) Left: fluid distribution prior to dissociation of hydrate films/shell. Water (blue), gas (red) and hydrate (black) reside in the pore space. Right: hydrate dissociation initiates in the pore center and progresses towards the pore walls (indicated by white arrows).

The observed dissociation mechanisms can explained by the hydrate thickness. In films/shell configuration, the hydrate seemed to be thinner in the pore center compared with the pore walls (see "Controlling mechanism and hydrate conversion pattern" in section 4.1.2). When the pressure reduction propagated through the encapsulated gas and/or wetting water films, the hydrate films/shell dissociated first in the locations with smaller hydrate thickness (pore center). In crystalline configuration, the hydrate phase had uniform thickness as it occupied the entire pore depth. As a result, the crystalline hydrate dissociated in the pore center and along the pore walls simultaneously, leading to the establishment of gas front propagating through the pore space.

4.3.2 Effect of global hydrate distribution

In section 4.3.1, the hydrate dissociation was discussed in relation to hydrate configurations within a single pore. The global distribution of hydrate within the entire pore system is of a particular interest for the production industry. This section describes the dissociation mechanisms for three distinct global hydrate distributions, where the hydrate phase is mainly represented by 1) crystalline hydrate, 2) hydrate films/shell, and 3) combination of both hydrate films/shell and crystalline hydrate.

Dissociation of crystalline hydrate

Figure 4.30 demonstrates the dissociation of crystalline hydrate. Crystalline hydrate, gas, water and grains are present in the images and they are denoted as H, G, W and R respectively. In image (a), the pore space was filled with crystalline hydrate surrounded by water. In image (b), the pressure reduction caused gas to emerge from hydrates outside the field of view. Gaseous methane from dissociated hydrate then displaced water from the pores marked by green circles. As a result, the hydrate dissociation was initiated in the adjacent pores indicated by yellow circles. In image (c), the propagating gas front induced further hydrate dissociation in the pores marked by yellow circles. In image (d), the hydrate-filled pores with narrow pore throats were bypassed by the gas front due to higher capillary forces. This allowed the hydrate crystals to exist for a prolonged time in the pores indicated by red and black circles. The hydrate crystals stabilized by small pore throats were generally observed to dissociate by two different mechanisms. In the first mechanism, which is shown in this particular example, the gas phase did not enter the hydrate-saturated pore. The gas bubbles did not release from dissociated hydrate (images e and f). Katsuki et al. (2008) observed similar behavior and suggested that the gas molecules evolved from dissociating hydrate diffused through water to the adjacent free gas phase. This phenomenon was explained by the temperature difference at the surface of dissociating hydrate and at the interface of water and free gas in the adjacent pore. Due to endothermic nature of hydrate dissociation, the temperature in the hydrate-dissociating area is lower than at the phase boundary between water and free gas in the neighboring pore. The solubility of methane in water is temperature-dependent at constant pressure. Therefore, the concentration of methane in water in equilibrium with hydrate differs from that of in equilibrium with gaseous methane. The resulted concentration gradient caused the diffusion and transfer of methane from hydrate-dissociating region to the gaseous methane in the adjacent pore. In the second mechanism, the hydrate crystals dissociated when the free gas was forced into the pore because of expanding gas phase in the entire micromodel. The examples of the second mechanism will also be shown in this section.

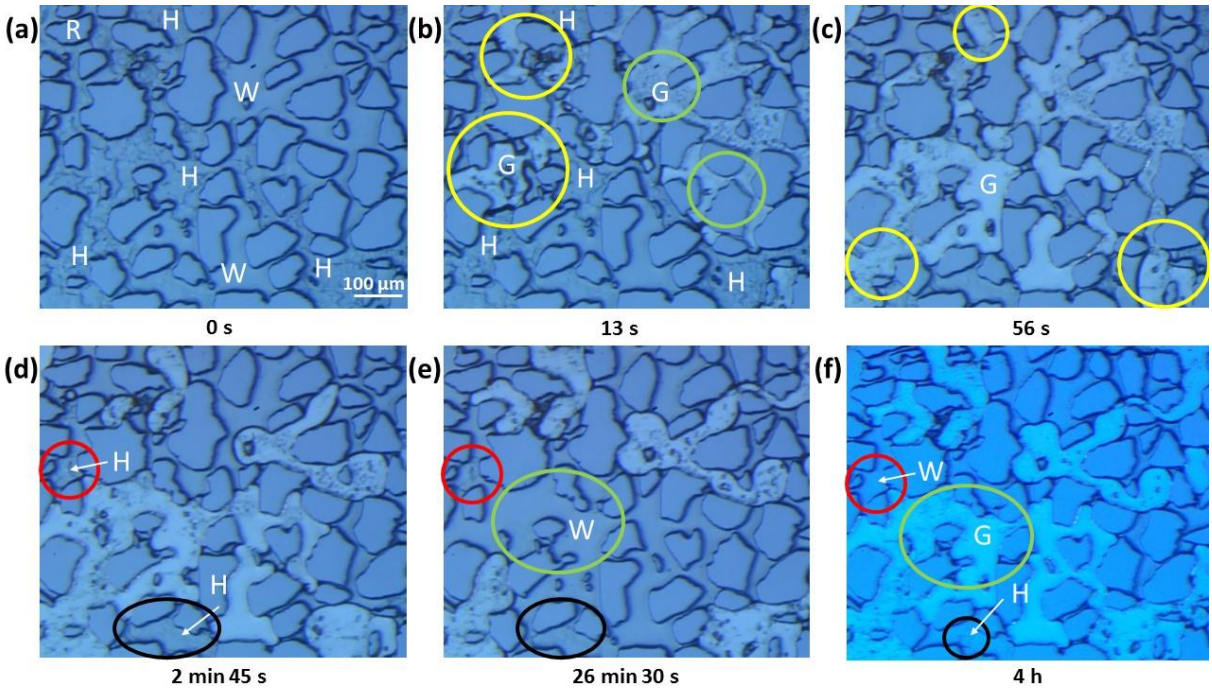

Figure 4.30. Dissociation of crystalline hydrate in experiment 14. Crystalline hydrate, gas, water and grains are indicated as H, G, W and R respectively. (a) Before hydrate dissociation, crystalline hydrate and water reside in the pore space. (b) Gas from dissociated hydrate displaces water from pores (green circles). The hydrate dissociation is initiated in the adjacent pores (yellow circles). (c) Gaseous methane from dissociated hydrate adds to already developed gas front, which leads to the hydrate dissociation in the pores denoted by yellow circles. (d) The hydrate is stabilized by small pore throats (red and black circles). (e) Free gas does not enter these pores and hydrate dissociation is slower. Gas retreats in the pores marked by a green circle due to overall fluid flow in the micromodel. (f) Hydrate dissociated in the pore indicated by a red circle, whereas a small hydrate crystal remains in the pore denoted by a black circle.

The two-dimensional saturation profiles were estimated for this experiment in particular (Figure 4.31) and all other examples in this section (Figure 4.33; Figure 4.35). The saturation profiles provide an insight into the fluid mobility during dissociation. The two-dimensional hydrate saturation was calculated as the sum of crystalline hydrate and hydrate films/shell. The detailed procedure for saturation measurements and their main limitations were discussed in section 3.3.2. The image sequences in this section cover only a part of the field of view. The fluid saturations were however estimated in the entire field of view but not only for the shown images.

Figure 4.31 demonstrates the saturation profile during the hydrate dissociation in experiment 14. The blue, red, black and green curves represent the water-, gas-, hydrate saturation and pressure respectively. Once the pressure was brought outside the hydrate stability zone, the hydrate saturation, S_h, dropped from 0.76 to 0.20 within three minutes with a subsequent reduction in the dissociation rate. Further decrease in S_h down to 0.1 was achieved around seven minutes later. The deceleration in dissociation rate was caused by small pore throats, which stabilized the hydrate. At the earlier stages (first several minutes), the saturation curves for hydrate and gas were nearly a mirror reflection of each other. This shows that for the first several minutes, the dissociating hydrate was the main source of free gas in the observed area. At the later stages (after five minutes), water and gas were both highly mobile and displacing each other chaotically within the field of view. The fluctuations in the pressure curve were likely related to the release of gas from dissociated hydrate in other parts of the model.

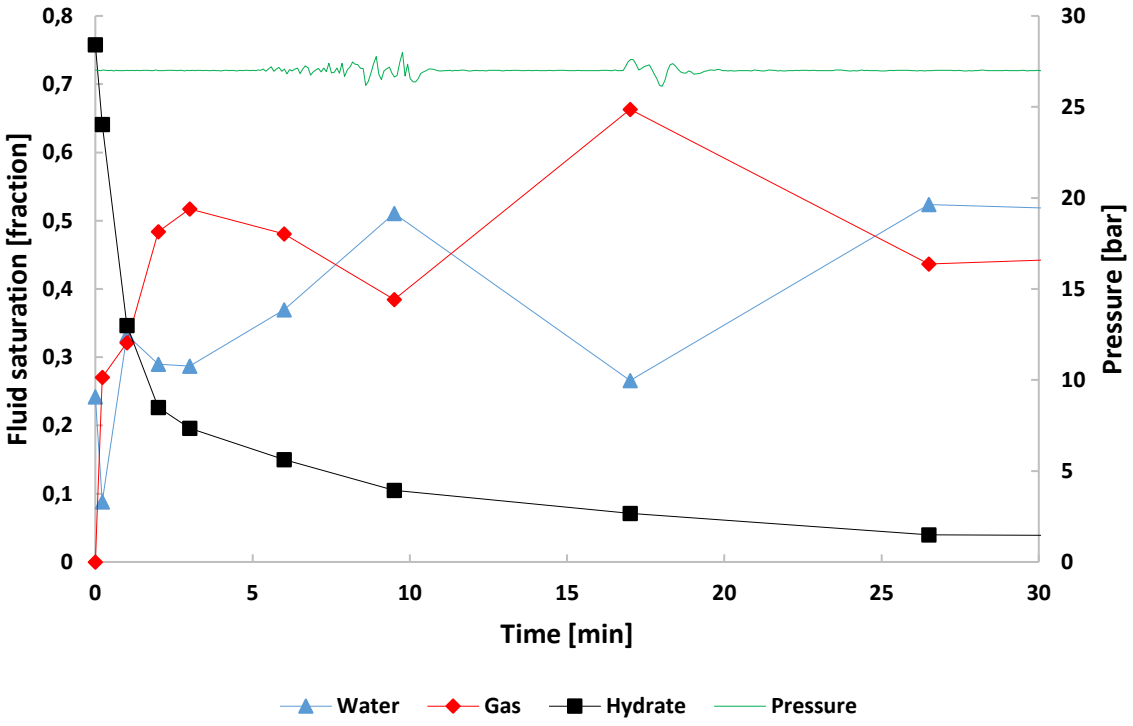

Figure 4.31. Saturation profile for dissociation of crystalline hydrate in experiment 14. The blue, red and black curves represent the saturation of water, gas and hydrate respectively. The pressure recordings are represented by a green curve.

Dissociation of hydrate films/shell

The dissociation of hydrate films/shell is shown in Figure 4.32. The hydrate films/shell, crystalline hydrate, water, water droplets, gas and grains are marked as HF, H, W, WD, G and R respectively. Image (a) demonstrates the fluid distributions prior to the dissociation, with relatively high saturation of hydrate films/shell; and small hydrate crystals (crystalline hydrate) and water residing in the smallest pores. Image (b) illustrates that the dissociation of hydrate films/shell initiated simultaneously in all pores due to high phase connectivity. The dissociation started in the middle of the pores first and then proceeded towards the pore walls. In image (c), the hydrate films/shell completely dissociated, leaving many water droplets below the gas phase. The green circles indicate the pores with small hydrate crystals. In image (d), the mobilized gas entered the pores saturated with small hydrate crystals, leading to their dissociation.

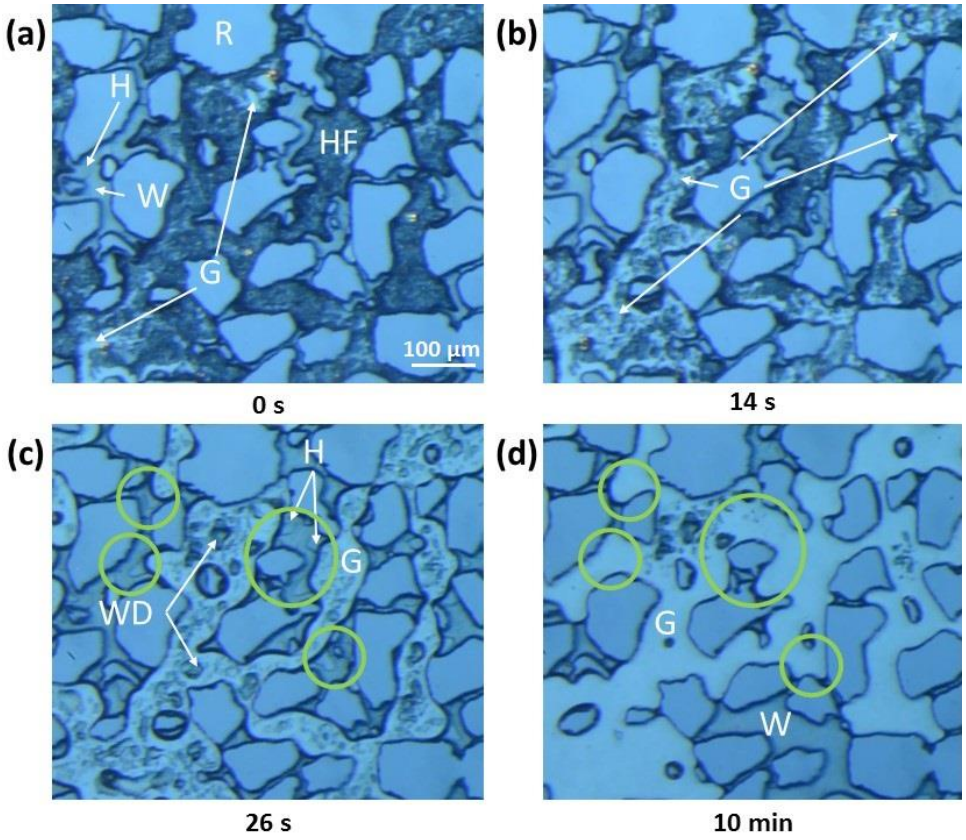

Figure 4.32. Dissociation of hydrate films/shell in experiment 4. Crystalline hydrate, hydrate films/shell, gas, water, water droplets and grains are denoted as H, HF, G, W, WD and R. (a) The pore space is mainly filled with hydrate films/shell. Water and hydrate crystals (crystalline hydrate) reside the smallest pores. (b) The dissociation of hydrate films/shell initiates in the middle of the pores when the pressure is lowered. (c) The hydrate films/shell is completely dissociated, releasing and mobilizing the gas phase. Water droplets reside below free gas. The green circles denote the pores with small hydrate crystals. (d) The small hydrate crystals dissociate due to gas inflow in the pores marked by green circles.

The saturation profile for dissociation of hydrate films/shell is illustrated in Figure 4.33. The blue, red, black and green curves represent the water-, gas-, hydrate saturation and pressure respectively. The hydrate saturation rapidly decreased from 0.74 to 0.07 when the pressure was lowered down to 27 bar. This indicated that most of the hydrate films/shell dissociated. For comparison, it took around seventeen minutes to reach nearly the same hydrate saturation during the dissociation of crystalline hydrate (Figure 4.31). This shows that the dissociation of hydrate films/shell was significantly faster compared to crystalline hydrate. An almost flat pressure curve indicates minor volumetric expansion. This suggests that less methane was bound in films/shell hydrates compared to the experiment with crystalline hydrate and that most of the hydrate dissociated simultaneously at earlier stages within the entire pore space of the model.

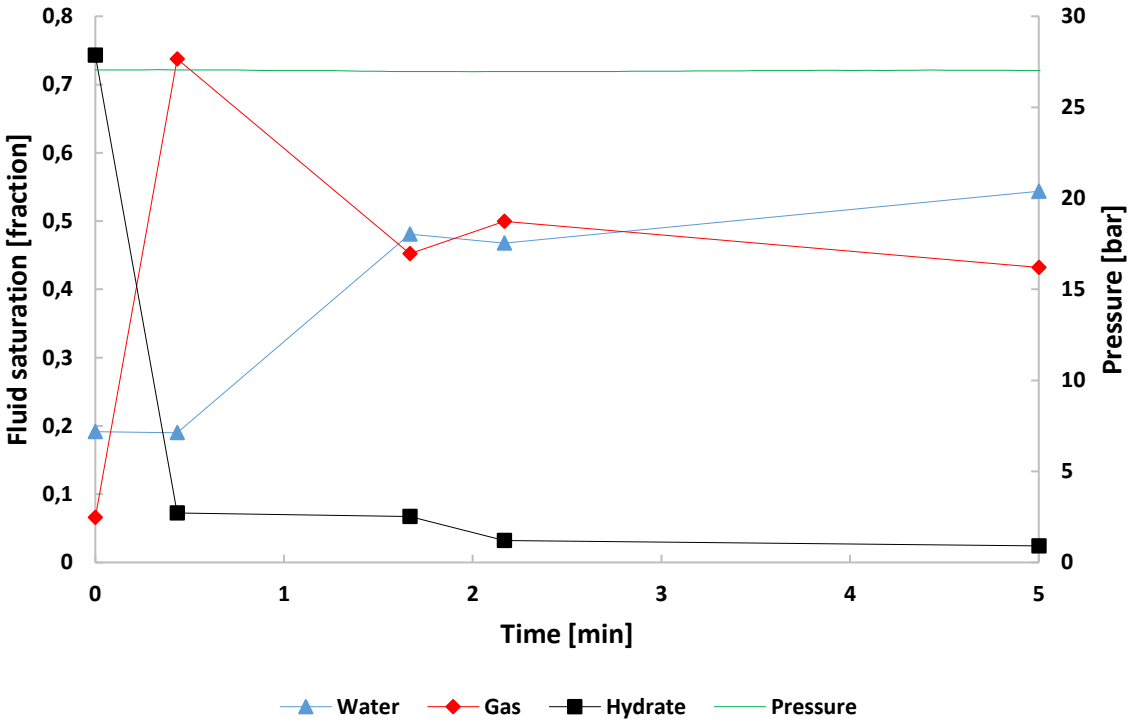

Figure 4.33. Saturation profile for dissociation of hydrate films/shell in experiment 4. The blue, red and black curves represent the saturation of water, gas and hydrate respectively. The pressure recordings are represented by a green curve.

Combined dissociation of hydrate films/shell and crystalline hydrate

Figure 4.34 illustrates the dissociation of the system that was saturated with both crystalline hydrate and hydrate films/shell. The symbols HF, H, W, G and R denote the hydrate films/shell, crystalline hydrate, water, gas and grains respectively. Image (a) shows the fluid distributions prior to pressure reduction. In image (b), the system's pressure was brought outside the hydrate stability zone. The hydrate films/shell with enclosed continuous gas phase dissociated immediately, thereby mobilizing the gas phase. In image (c), the crystalline hydrate began to dissociate in the location where the hydrate crystals were in contact with a gas bubble enclosed by hydrate films/shell (HF) marked by a yellow circle. The color change from transparent to dark indicated that the gas bubbles were released inside the crystalline hydrate but they were still enclosed by hydrate films/shell. The continuous gas phase retreated from the pores denoted by red circles due to the global gas flow in the model. In image (d), the release of gas bubbles continued from crystalline hydrate inside the hydrate films/shell indicated by the yellow circle. In image (e), when the saturation of these gas bubbles reached the critical value, the hydrate films/shell dissociated, leading to further mobilization of gas. The mobilized gas expanded and entered the pore marked by a yellow circle. The green circles denote the pores where crystalline (transparent) and hydrate films/shell (black) had not been dissociated yet because of transport restriction through small pore throats. In image (f), the hydrate phase surrounded by small pore throats dissociated only after the free gas phase had entered these pores.

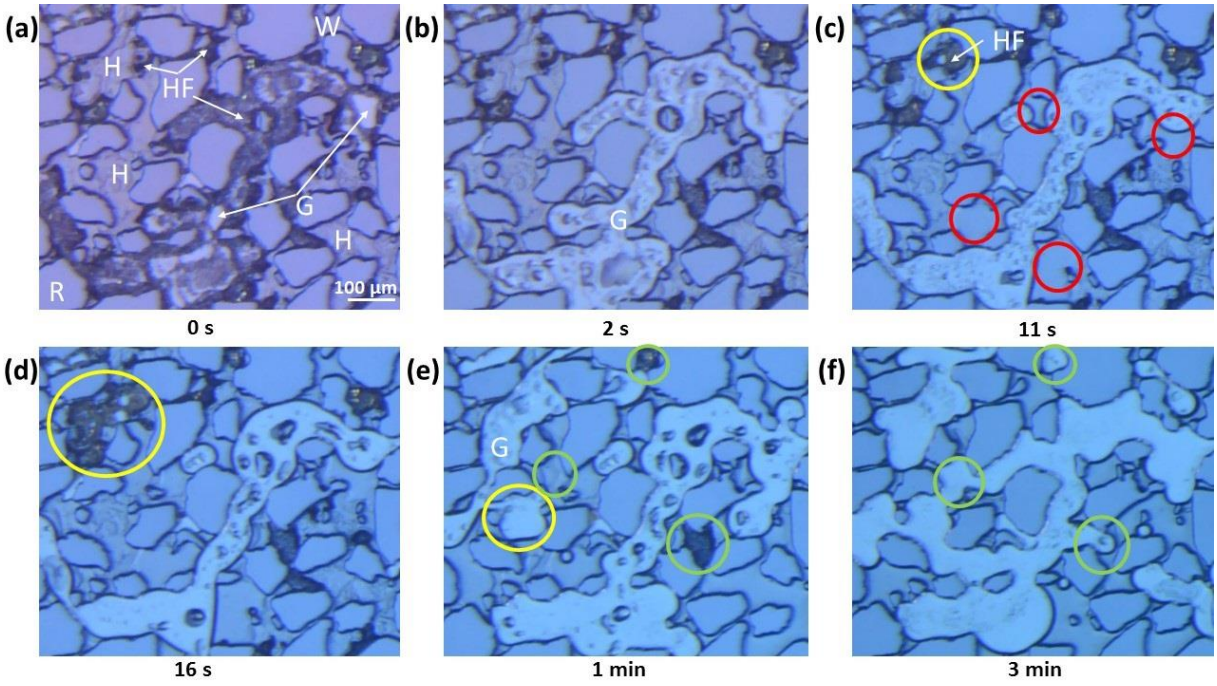

Figure 4.34. Hydrate dissociation experiment 2. Crystalline hydrate, hydrate films/shell, gas, water and grains are denoted as H, HF, G, W and R. (a) Fluid distributions before the hydrate dissociation was observed in the field of view. (b) Pressure reduction induces the dissociation of hydrate films/shell with enclosed gas (G). (c) The red circles denote the pores where gas retreated due to high gas mobility. The dissociation of crystalline hydrate began in the area adjacent to the hydrate films/shell (HF) (yellow circle). (d) The yellow circle shows the area where gas continues to emerge from crystalline hydrate but remains encapsulated by hydrate films/shell. (e) Gas (G) is released from hydrate films/shell and expands to the adjacent pore (yellow circle). The green circles denote the pores with narrow pore throats where non-dissociated crystalline (transparent) hydrate and hydrate films/shell (black) reside. (f) The hydrate phase surrounded by small pore throats finally dissociated when free gas contacted hydrate as denoted by green circles.

Figure 4.35 presents the saturation profile for dissociation of crystalline hydrate and hydrate films/shell. Water-, gas- and hydrate saturation are represented by blue, red and black curves respectively. The green curve indicates the system's pressure. The pressure reduction below the equilibrium value decreased the hydrate saturation, S_h, from 0.81 to 0.47 within several seconds, which was due to the dissociation of hydrate films/shell with enclosed continuous gas phase. Subsequent slower decrease in S_h to 0.07 was caused by dissociation of crystalline hydrate. The rate of dissociation was further decelerated, indicating that small pore throats stabilized the remaining hydrate. The average dissociation rate was much faster compared with crystalline hydrate (Figure 4.31) but was nearly the same as in the systems containing hydrate films/shell (Figure 4.33). The variations in pressure are likely due to the gas expansion from the dissociated crystalline hydrate in different parts of the micromodel.

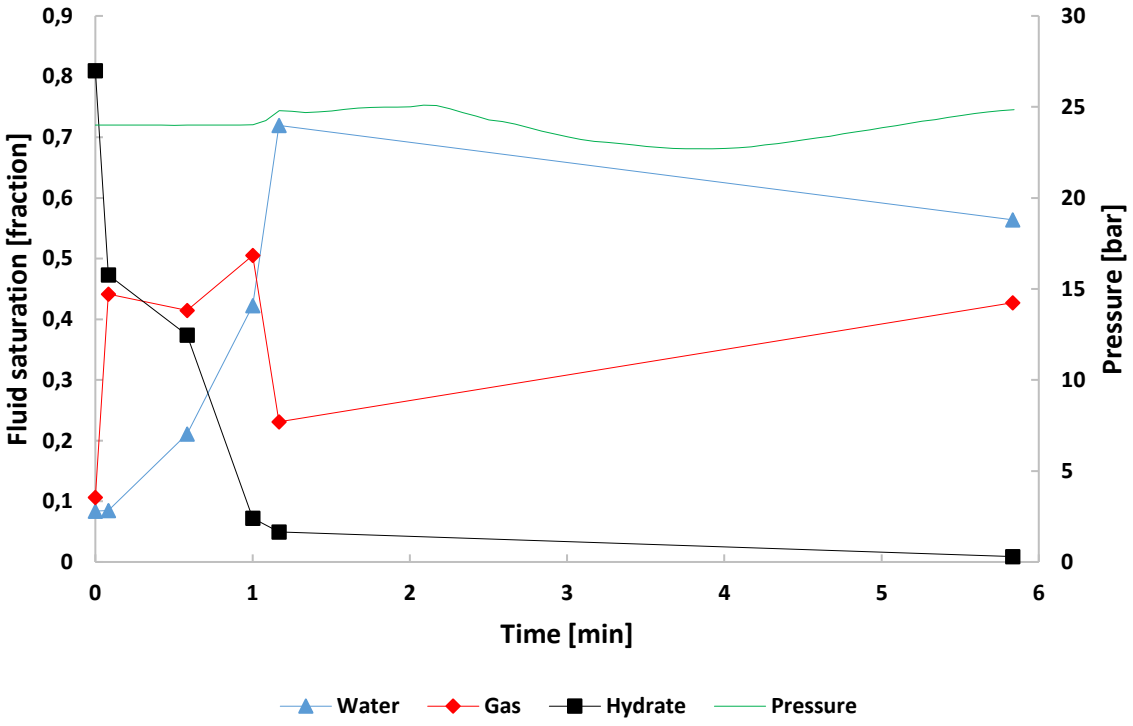

Figure 4.35. Saturation profile for dissociation of hydrate films/shell combined with crystalline hydrate in experiment 2. The blue, red and black curves represent the saturation of water, gas and hydrate respectively. The pressure recordings are represented by a green curve.

Summarizing all the results discussed in section 4.3.2, the average rate of dissociation was the slowest when the hydrate phase was represented by crystalline hydrate, whereas the hydrate films/shell dissociated much faster. The hydrate phase surrounded by smaller pore throats was always the last to dissociate. The hydrate dissociation was favored in the locations where the hydrate was in contact with free gas and rather than water. In naturally occurring systems, the hydrate accumulations with a significant fraction of free gas would therefore be a preferential target for production by pressure depletion.

4.3.3 Effect of hydrate saturation

It was observed that not only the hydrate configuration but also its saturation affected the dissociation process. In experiment 1, the crystalline hydrate massively grew in the entire micromodel due to additional water and gas supply during the growth process, with the resulting hydrate saturation approaching unity. The pressure was initially reduced to 25 bar to destabilize the hydrate. After approximately four hours without visible hydrate dissociation, the pressure was further reduced to 8 bar, which resulted in hydrate dissociation within field of view two hours later. By studying other parts of the micromodel, it was noticed that the hydrate dissociation had initiated before but proceeded very slowly towards the field of view. The dissociation process is illustrated in Figure 4.36. Image (a) shows the fluid distribution prior to the dissociation process with almost only crystalline hydrate present. In image (b), the gas front from dissociated hydrate entered the field of view and initiated the subsequent dissociation of the adjacent hydrate. Near the gas front, the hydrate dissociation was observed to occur without the release of gas bubbles, suggesting that methane molecules diffused through water to the neighboring gaseous methane. The white arrows in image (b) denote the phase boundary between crystalline hydrate (H) and water from dissociated hydrate. In image (c), the free gas front had a very low mobility and it propagated further to that pore, which was filled with water from dissociated hydrate marked by a yellow circle. This can be explained by the higher pressure in gas compared to water, where gas will seek escape in pores with low resistance to flow: the larger pores with mobile water. To accelerate the dissociation process, the pressure was gradually reduced to 4 bar and then to atmospheric conditions. As a result of decreased pressure, free gas also propagated into the hydrate-filled pores, inducing further dissociation (images (d) and (e)). The white arrows in image (d) indicate the interface between crystalline hydrate and water from dissociated hydrate. In image (f), the gas phase retreated due to overall flow in the system, leaving water in the pores marked by a red circle. The hydrate phase continued to slowly dissociate in the adjacent pores, where the white arrows denote the hydrate-water interface. The hydrate dissociated completely in the field of view around two hours later. A comparison of all the experiments where crystalline hydrates dissociate show that the propagation rate of the gas front from dissociated hydrate appeared to increase with decreasing pressures.

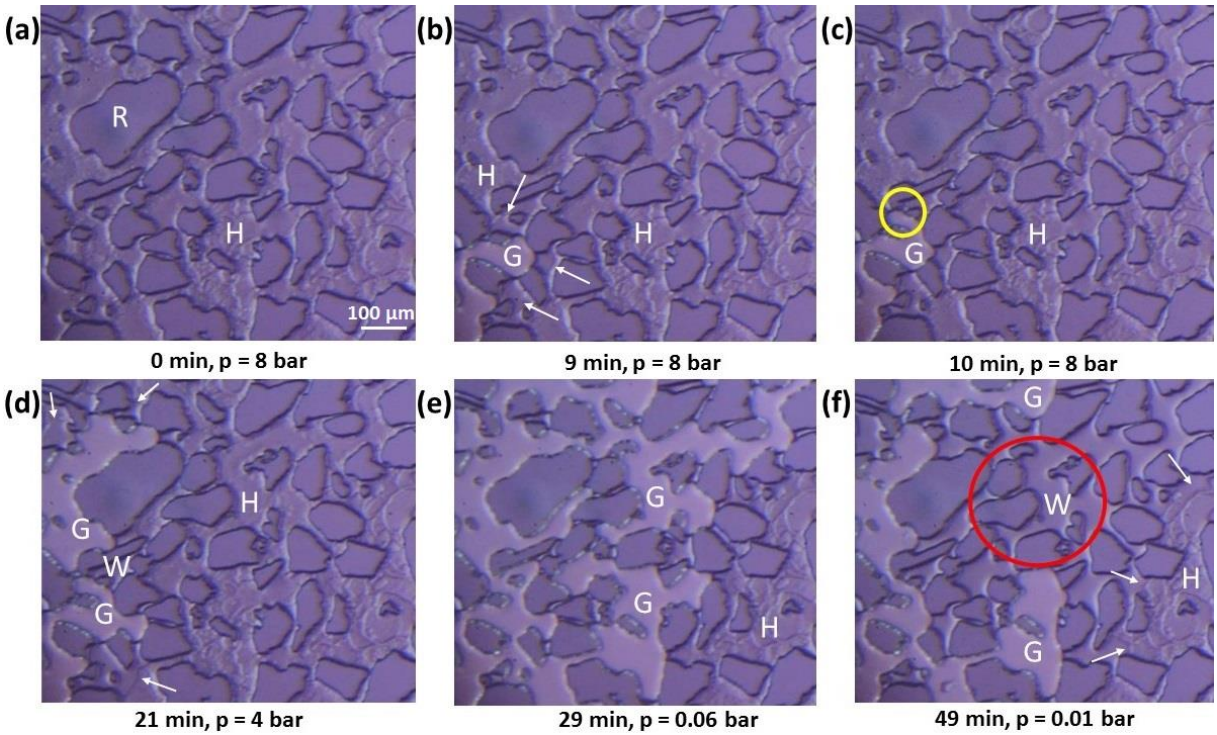

Figure 4.36. Hydrate dissociation experiment 1. Crystalline hydrate, gas, water and grains are denoted as H, G, W and R. (a) The pore space is filled with crystalline hydrate (H) before the hydrate dissociation initiates in the field of view. (b) Gas from already dissociated hydrate enters the field of view and destabilizes the hydrate phase in the adjacent pores. The gas molecules from dissociated hydrate diffuse through water to the adjacent free gas. The white arrow indicates the hydrate-water interface. (c) Free gas displaces water from the neighboring pore (yellow circle). (d) The reduction in pressure causes further hydrate dissociation, which results in the release and mobilization of gas. Water from dissociated hydrate is enclosed by free gas and hydrate. The white arrows show the phase boundary between water and hydrate. (e) The pressure is lowered to atmospheric, which promotes further dissociation with a subsequent release of gas. (f) Gas retreats because of overall gas flow in the entire micromodel and water remains in the pores indicated by a red circle.

Figure 4.37 represents the saturation of fluids during the hydrate dissociation in experiment 1. The blue, red, black and green curves correspond to water-, gas- and hydrate saturations and pressure respectively. While pressure was gradually decreasing from 8 to 4 bar, the hydrate saturation decreased from 0.98 to 0.91 within thirty minutes. The pressure was further lowered to atmospheric conditions, which in turn significantly improved the gas mobility. As a result, the hydrate saturation dropped from 0.91 to 0.61 within three minutes. The rate of dissociation then decelerated as no external pressure drive was applied.

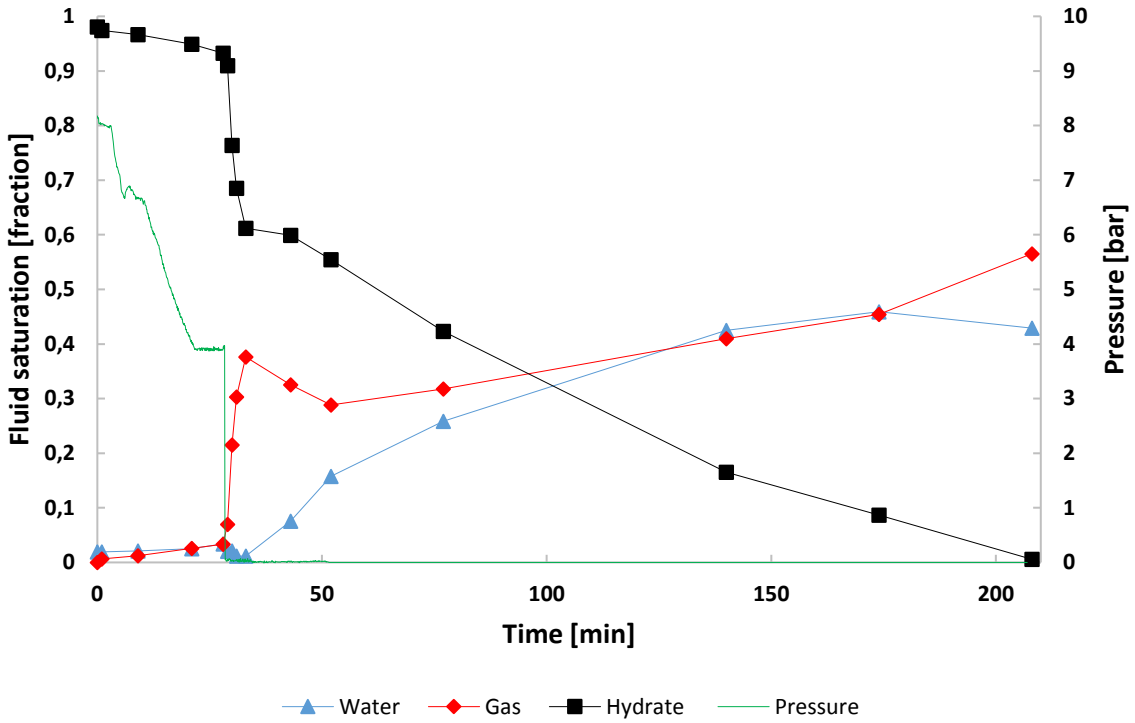

Figure 4.37. Saturation profile for dissociation of crystalline hydrate in experiment 1. The blue, red and black curves represent the saturation of water, gas and hydrate respectively. The pressure recordings are represented by a green curve.

The delayed dissociation of crystalline hydrate may represent the self-preservation of natural gas-hydrates for temperatures above 0 °C as discussed in section 1.4.5. The saturation profile for this particular example (Figure 4.37) can be compared to the experiment where the hydrate phase was also represented by crystalline hydrate but with lower saturation (Figure 4.31). It can be seen that the overall rate of dissociation is slower for high hydrate saturation. Note, however, that hydrate saturations close to unity are not commonly found in nature. The methane hydrate accumulations with saturations up to 0.8 can be found in the Nankai Trough and they are considered high (Collett, 2008).

The hydrate dissociation described in this section shows that the direct contact with free gas does not necessarily increase the dissociation rate; the gas phase has to be mobile to promote rapid dissociation. The endothermic nature of hydrate dissociation may restrict further dissociation of the adjacent hydrate if the heat is not transported to the hydrate-dissociating area. Free gas acts as the heat-insulator in relation to water. Gas with nearly zero effective permeability therefore restricts the heat-transfer to the gas-hydrate boundary, causing low dissociation rates. In cases with high-mobility gas, the hydrate prefers to dissociate in contact with gas rather than water because gas has an improved mobility compared to water. This in turn enhances the heat-transport to the hydrate-dissociating region.

4.3.4 Hydrate reformation during depressurization

One of the challenges related to extraction of natural gas from solid state hydrates is the re-formation of hydrates near the production well due to changing pressure and/or temperature conditions. In this work, the hydrate reformation during pressure depletion was observed in several experiments. This was mainly caused by gas release from hydrates melting elsewhere in the system. An example of hydrate re-formation during depressurization is shown in Figure 4.38. The porous media was initially saturated with water (W) and hydrate films/shell (HF) (image (a)). The water pump cylinder was set to retract at rate of 10 ml/h, thereby lowering the pressure in the system. In image (b), the dissociation

of hydrate films/shell initiated when the pressure was lowered to 24 bar ($p_{eq} = 26.2$ bar), leading to the release of gas from hydrates. The green circles denote the hydrate films/shell that was not dissociated. The water pump cylinder was still retracting at constant rate and was not switched to constant pressure operation. In image (c), an extensive volume expansion led to a sudden increase in pressure up to 36 bar within one minute, which in turn resulted in the formation of hydrate films/shell around free gas. The hydrate films/shell marked by green circles was converted to crystalline hydrate. In image (d), the pressure was reduced below the equilibrium value with a constant pressure operation mode, which led to hydrate dissociation. The experiments with hydrate re-formation illustrate the importance of a carefully controlled pressure reduction during gas production from hydrates. Local temperature fluctuations during hydrate dissociation were not investigated in this thesis due to the limitations in the apparatus. The maximum decrease in temperature registered by the thermocouple was in the range of 0.1 °C, which does not exceed the limit of uncertainty in the temperature measurements.

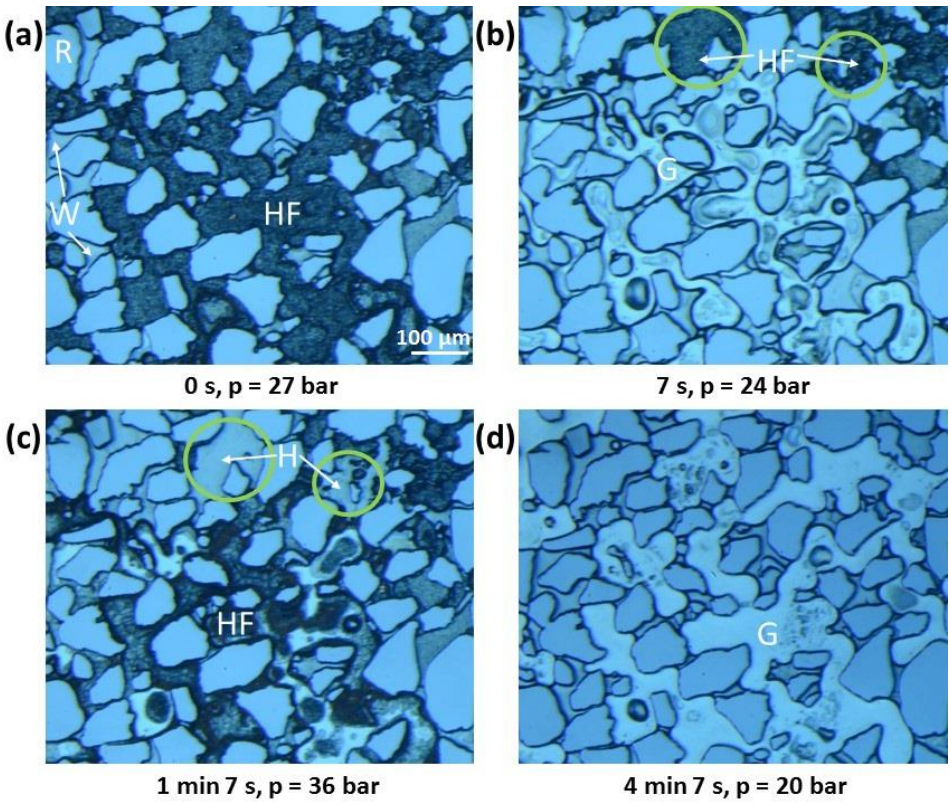

Figure 4.38. Hydrate reformation during pressure depletion in experiment 8_SEC_5. (a) The system's pressure is still within the hydrate stability zone. Hydrate films/shell, water and grains are present and denoted as HF, W and R respectively. (b) The pressure is lowered below the equilibrium value. Most of the hydrate films/shell dissociated, releasing the gas phase. The green circles indicate the pores where the hydrate films/shell did not dissociate. (c) The transformation from solid hydrate to gaseous methane leads to volumetric expansion in the model, which in turn causes the pressure to increase above the equilibrium value ($p_{eq} = 26.2$ bar). As a result, hydrate films/shell encompass the gas phase. The green circles denote the pores where the hydrate films/shell was converted to crystalline hydrate (H). (d) Hydrate dissociates during pressure reduction.

5 Conclusions

The methane hydrate formation and dissociation mechanisms were investigated both qualitatively and quantitatively on pore scale utilizing silicon micromodel. This chapter presents key observations and is divided into three main groups: hydrate formation mechanisms, hydrate growth rates and hydrate dissociation.

Hydrate formation mechanisms

- Hydrate growth initiated rapidly in the continuous gas phase at the water-gas interface along the pore walls and then slowly proceeded towards the pore center. Further hydrate formation progressed to isolated gas bubbles, with a similar growth pattern from pore walls towards pore centers.
- Hydrate growth resulted in two distinct hydrate configurations: hydrate films/shell with encapsulated gas and crystalline hydrate without enclosed gas. Water availability and transport was a dominant factor leading to formation of the latter configurations.
- Most of gas was totally converted to crystalline hydrate in the entire micromodel if either excess initial water saturation or additional water supply fed further hydrate growth. In case of limited water excess, the isolated gas bubbles were mainly converted to crystalline hydrate, whereas the continuous gas remained encapsulated by hydrate films/shell.
- Hydrate growth in water was rarely observed and depended on the availability of free gas in the neighboring pores. Massive hydrate formation in water was only achieved when an adequate mass of methane was forced to dissolve in water.
- Most of primary formations were triggered by agitation. Secondary hydrate formations initiated spontaneously at lower pressures, supporting the memory effect phenomenon.

Hydrate growth rates

- Hydrate films grew linearly with time at the water-gas interface.
- Hydrate film growth rate along the pore walls was approximately two orders of magnitude faster than the hydrate growth towards the pore center.
- The growth of hydrate crystals in water was around one order of magnitude slower than the pore center growth rate due to slow diffusive transport to hydrate-forming areas.
- No clear effect of initial water saturation and pore sizes on the growth rates was found.
- Driving force expressed in terms of subcooling had a clear influence on the growth rates.
- Pore center growth rate increased with subcooling (ΔT) but the correlation was weak and likely suppressed by mass transport limitations. Pore wall growth rate seemed to be proportional to ΔT^2.
- The hydrate film growth along the pore walls was slightly faster but showed a good agreement with film growth measurements reported in literature for bulk systems.

Hydrate dissociation

- Two hydrate configurations (crystalline and films/shell) resulted in different dissociation patterns during depressurization.
- Gas from dissociated crystalline hydrate formed a front that slowly propagated through the pore space, inducing further dissociation of the adjacent hydrate.
- Hydrate films/shell with enclosed gas dissociated more rapidly, with a dissociation pattern from pore center towards pore walls. The enclosed gas was mobilized and flowed through the entire pore network.
- Hydrate dissociated preferentially through contact with free gas rather than water.
- Hydrate was observed to dissociate last in the pores surrounded by small pore throats.

- The overall dissociation rate of crystalline hydrate appeared to increase with higher gas mobility and with lower hydrate saturation.

6 Future work

The following suggestions for further studies are based on the author's interest and unanswered research tasks that became apparent in this MS work. The way forward if more time and funding allowed would be:

- Investigation of methane hydrates growth in micromodels using a microscope with improved resolution. This might enable the quantification of the hydrate film thickness and the detection of thin wetting water films coating the grains.
- Studies of methane hydrate phase transitions in micromodels with different wettability and mineral surfaces.
- Complementary investigation of methane hydrate growth rates in micromodels at various pressure-temperature conditions.
- Measurements of carbon dioxide hydrate growth rates in micromodels to compare with results from the methane hydrate growth rates reported here.
- Pore scale studies of methane - carbon dioxide exchange in hydrate-bearing porous media.

Nomenclature and abbreviations

Nomenclature

A_i	Area of a particular phase (gas or hydrate)	[μm^2]
A_{tot}	Total image area	[μm^2]
A_v	Area of void space in the image	[μm^2]
ΔG	Excess Gibbs free energy	[J]
ΔG_{crit}	Critical excess free energy	[J]
$\Delta G'_{crit}$	Critical excess free energy for heterogeneous nucleation	[J]
ΔG_s	Surface excess free energy	[J]
ΔG_v	Volume excess free energy	[J]
Δg^{exp}	Total molar change in Gibbs free energy of hydrate formation	[J/mol]
$\Delta g^{reactants}$	Molar change in Gibbs free energy for reactants (gas and water)	[J/mol]
$\Delta g^{products}$	Molar change in Gibbs free energy for products (hydrate)	[J/mol]
N_{grains}	Number of grain pixels in the image	[J/mol]
N_i	Number of a phase pixels (gas or hydrate) in the image	-
N_{tot}	Total number of pixels in the image	-
N_v	Number of void pixels in the image	-
$n_{hydrate}$	Refractive index of methane hydrate	-
$n_{methane}$	Refractive index of methane gas	-
n_{water}	Refractive index of water	-
n	Number of values in the data set	-
n	Number of measurements	-
p	System's pressure	[bar]
p_{diss}	System's pressure during hydrate dissociation	[bar]
p_{eq}	Equilibrium system's pressure under a given temperature	[bar]
p_{final}	Final system's pressure during hydrate formation	[bar]
$p_{initial}$	System's pressure at which the hydrate formation is initially observed	[bar]
r	Radius of a sphere	[m]
r_c	Radius of the critical cluster/nuclei	[m]
S	Standard deviation	-
S_i	Saturation of a particular fluid (S_w - water; S_g - gas; S_h - hydrate)	[fraction]
$\bar{S}_{wi}$	Initial global water saturation	[fraction]
$\Delta\bar{S}_{wi}$	Uncertainty in the initial global water saturation	[fraction]
T_{eq}	Equilibrium system's temperature under a given pressure	[°C]
T_{sys}	System's temperature	[°C]
ΔT	Degree of subcooling	[°C]
t	Time	[s]
v	Hydrate film growth rate	[µm/s]
Δv	Uncertainty in the hydrate film growth rate	[µm/s]
v_f	Hydrate film growth rate along the pore walls	[µm/s]
$\bar{x}$	Mean value of all values in the data set	-
x_i	Each value in the data set	-
β	Proportionality coefficient for the pore wall growth rate	-
θ	Contact angle	[degrees]
γ_{cl}	Interfacial tension between solid crystalline and liquid	[J/m^2]
γ_{cs}	Interfacial tension between solid crystalline and foreign solid surface	[J/m^2]
γ_{sl}	Interfacial tension between foreign solid surface and liquid	[J/m^2]
ϕ	Proportionality coefficient between $\Delta G'_{crit}$ and ΔG_{crit}	-
ϕ_p	Porosity	[fraction]

Abbreviations

DRIE	Deep reactive ionic etching
G	Methane gas
H	Crystalline hydrate without encapsulated gas
HEN	Heterogeneous nucleation
HF	Hydrate films/shell with encapsulated gas
HON	Homogeneous nucleation
HSZ	Hydrate stability zone
Hw	Hydrate in water
MRI	Magnetic resonance imaging
NGH	Natural gas hydrate
PEEK	Polyetheretherketone
R	Grains in the rock structure
SEM	Scanning electron microscope
sI	Structure I hydrate
sII	Structure II hydrate
sH	Structure H hydrate
W	Distilled water

Bibliography

Almenningen, S., Flatlandsmo, J., Fernø, M. A., & Ersland, G. (2017a). Direct Pore-Level Visualization of Methane Hydrate Growth in an Authentic Sandstone Replicate. Paper presented at the *Proceedings of the 9th International Conference on Gas Hydrates*, Denver, Colorado, USA.

Almenningen, S., Flatlandsmo, J., Fernø, M. A., & Ersland, G. (2017b). Multiscale Laboratory Verification of Depressurization for Production of Sedimentary Methane Hydrates. *SPE Journal*, *22*(01), 138-147.

Almenningen, S., Iden, E., Fernø, M. A., & Ersland, G. (2018). Pore-scale salinity effects on methane hydrate dissociation. Submitted to *Journal of Geophysical Research: Solid Earth*.

Arjmandi, M., Tohidi, B., Danesh, A., & Todd, A. C. (2005). Is subcooling the right driving force for testing low-dosage hydrate inhibitors?. *Chemical engineering science*, *60*(5), 1313-1321.

Baldwin, B. A., Stevens, J., Howard, J. J., Graue, A., Kvamme, B., Aspenes, E., ... & Zornes, D. R. (2009). Using magnetic resonance imaging to monitor CH4 hydrate formation and spontaneous conversion of CH4 hydrate to CO2 hydrate in porous media. *Magnetic resonance imaging*, *27*(5), 720-726.

Buchgraber, M., Al-Dossary, M., Ross, C. M., & Kovscek, A. R. (2012). Creation of a dual-porosity micromodel for pore-level visualization of multiphase flow. *Journal of Petroleum Science and Engineering*, *86*, 27-38.

Bylov, M., & Rasmussen, P. (1997). Experimental determination of refractive index of gas hydrates. *Chemical engineering science*, *52*(19), 3295-3301.

Cahn, J. W., Hillig, W. B., & Sears, G. W. (1964). The molecular mechanism of solidification. *Acta Metallurgica*, *12*(12), 1421-1439.

Christiansen, R. L., & Sloan Jr, E. D. (1995). *A compact model for hydrate formation* (No. CONF-9503132--). Gas Processors Association, Tulsa, OK (United States).

Churaev, N. V., Bardasov, S. A., & Sobolev, V. D. (1993). On the non-freezing water interlayers between ice and a silica surface. *Colloids and Surfaces A: Physicochemical and Engineering Aspects*, *79*(1), 11-24.

Clennell, M. B., Hovland, M., Booth, J. S., Henry, P., & Winters, W. J. (1999). Formation of natural gas hydrates in marine sediments: 1. Conceptual model of gas hydrate growth conditioned by host sediment properties. *Journal of Geophysical Research: Solid Earth*, *104*(B10), 22985-23003.

Collett, T. S. (2008). Geology of marine gas hydrates and their global distribution. In *Offshore Technology Conference*. Offshore Technology Conference.

Colorado School of Mines (2009). Center for hydrate research. Retrieved May 6, 2018, from: http://hydrates.mines.edu/CHR/Software.html

Davies, S. R., Selim, M. S., Sloan, E. D., Bollavaram, P., & Peters, D. J. (2006). Hydrate plug dissociation. *AIChE Journal*, *52*(12), 4016-4027.

Demirbas, A. (2010). *Methane gas hydrate*. Springer Science & Business Media.

Ecker, C., Dvorkin, J., & Nur, A. (1998). Sediments with gas hydrates: Internal structure from seismic AVO. *Geophysics*, *63*(5), 1659-1669.

Ersland, G., Husebø, J., Graue, A., Baldwin, B. A., Howard, J., & Stevens, J. (2010). Measuring gas hydrate formation and exchange with CO2 in Bentheim sandstone using MRI tomography. *Chemical Engineering Journal*, *158*(1), 25-31.

Fitzgerald, G. C., Castaldi, M. J., & Schicks, J. M. (2014). Methane hydrate formation and thermal based dissociation behavior in silica glass bead porous media. *Industrial & Engineering Chemistry Research*, *53*(16), 6840-6854.

Flatlandsmo, J. (2015). *Visualization and interpretation of methane hydrate growth and dissociation in synthetic porous media* (Master's thesis, The University of Bergen).

Freer, E. M., Selim, M. S., & Sloan Jr, E. D. (2001). Methane hydrate film growth kinetics. *Fluid Phase Equilibria*, *185*(1-2), 65-75.

Goldberg, D., & Saito, S. (1998). Detection of gas hydrates using downhole logs. *Geological Society, London, Special Publications*, *137*(1), 129-132.

Graue, A., Kvamme, B., Baldwin, B., Stevens, J., Howard, J. J., Aspenes, E., ... & Zornes, D. (2008). MRI visualization of spontaneous methane production from hydrates in sandstone core plugs when exposed to CO2. *SPE Journal*, *13*(02), 146-152.

Hammerschmidt, E. G. (1934). Formation of gas hydrates in natural gas transmission lines. *Industrial & Engineering Chemistry*, *26*(8), 851-855.

Handa, Y. P., & Stupin, D. Y. (1992). Thermodynamic properties and dissociation characteristics of methane and propane hydrates in 70-. ANG.-radius silica gel pores. *The Journal of Physical Chemistry*, *96*(21), 8599-8603.

Hauge, L. P., Gauteplass, J., Høyland, M. D., Ersland, G., Kovscek, A., & Fernø, M. A. (2016). Pore-level hydrate formation mechanisms using realistic rock structures in high-pressure silicon micromodels. *International Journal of Greenhouse Gas Control*, *53*, 178-186.

Hong, H., Pooladi-Darvish, M., & Bishnoi, P. R. (2003). Analytical modelling of gas production from hydrates in porous media. *Journal of Canadian Petroleum Technology*, *42*(11), 45-56.

Hornbach, M. J., Holbrook, W. S., Gorman, A. R., Hackwith, K. L., Lizarralde, D., & Pecher, I. (2003). Direct seismic detection of methane hydrate on the Blake Ridge. *Geophysics*, *68*(1), 92-100.

Hornbrook, J. W., Castanier, L. M., & Pettit, P. A. (1991). Observation of foam/oil interactions in a new, high-resolution micromodel. In *SPE Annual Technical Conference and Exhibition*. Society of Petroleum Engineers.

Iden, E. (2017). *Pore-Level Interpretation of Methane Hydrate Growth and Dissociation with Deionized and Saline Water* (Master's thesis, The University of Bergen).

International Energy Agency (2017). *World energy outlook 2017, executive summary.* Retrieved May 9, 2018, from: https://www.iea.org/publications/freepublications/publication/WEO_2017_Executive_Summary_English_version.pdf

Iwai, H., Kimoto, S., Akaki, T., & Oka, F. (2015). Stability analysis of methane hydrate-bearing soils considering dissociation. *Energies*, *8*(6), 5381-5412.

Kashchiev, D., & Firoozabadi, A. (2003). Induction time in crystallization of gas hydrates. *Journal of crystal growth*, *250*(3-4), 499-515.

Kang, S. P., Seo, Y., & Jang, W. (2009). Kinetics of methane and carbon dioxide hydrate formation in silica gel pores. *Energy & Fuels*, *23*(7), 3711-3715.

Katsuki, D., Ohmura, R., Ebinuma, T., & Narita, H. (2008). Visual observation of dissociation of methane hydrate crystals in a glass micro model: Production and transfer of methane. *Journal of applied physics*, *104*(8), 083514.

Katsuki, D., Ohmura, R., Ebinuma, T., & Narita, H. (2007). Methane hydrate crystal growth in a porous medium filled with methane-saturated liquid water. *Philosophical magazine*, *87*(7), 1057-1069.

Kitami Institute of Technology (n.d.). Methane hydrate. Retrieved 9 May, 2018, from: http://www-ner.office.kitami-it.ac.jp/hydrate-structure.JPG

Kumar, A., Maini, B., Bishnoi, P. R., Clarke, M., Zatsepina, O., & Srinivasan, S. (2010). Experimental determination of permeability in the presence of hydrates and its effect on the dissociation characteristics of gas hydrates in porous media. *Journal of Petroleum Science and Engineering*, *70*(1-2), 114-122.

Kvamme, B., Graue, A., Buanes, T., Kuznetsova, T., & Ersland, G. (2007). Storage of CO2 in natural gas hydrate reservoirs and the effect of hydrate as an extra sealing in cold aquifers. *International Journal of Greenhouse gas control*, *1*(2), 236-246.

Kvamme, B., Kuznetsova, T., Bauman, J. M., Sjöblom, S., & Avinash Kulkarni, A. (2016). Hydrate formation during transport of natural gas containing water and impurities. *Journal of Chemical & Engineering Data*, *61*(2), 936-949.

Lee, S. Y., & Holder, G. D. (2001). Methane hydrates potential as a future energy source. *Fuel processing technology*, *71*(1-3), 181-186.

Li, X. S., Xu, C. G., Zhang, Y., Ruan, X. K., Li, G., & Wang, Y. (2016). Investigation into gas production from natural gas hydrate: A review. *Applied Energy*, *172*, 286-322.

MacDonald, G. J. (1990). Role of methane clathrates in past and future climates. *Climatic Change*, *16*(3), 247-281.

Makogon, Y. F., & Ghassemi, A. (2010). Effects of self-preservation of natural gas-hydrates. In *44th US Rock Mechanics Symposium and 5th US-Canada Rock Mechanics Symposium*. American Rock Mechanics Association.

Makogon, I. F. (1997). *Hydrates of hydrocarbons*. Pennwell Books.

Makogon, Y. F. (2010). Natural gas hydrates–A promising source of energy. *Journal of Natural Gas Science and Engineering*, *2*(1), 49-59.

Moridis, G. J., Collett, T. S., Dallimore, S. R., Satoh, T., Hancock, S., & Weatherill, B. (2002). *Numerical simulation studies of gas production scenarios from hydrate accumulations at the Mallik Site, McKenzie Delta, Canada* (No. LBNL--49764). Ernest Orlando Lawrence Berkeley National Laboratory, Berkeley, CA (US).

Moridis, G., Collett, T. S., Pooladi-Darvish, M., Hancock, S. H., Santamarina, C., Boswell, R., … Koh, C. (2011). Challenges, Uncertainties, and Issues Facing Gas Production From Gas-Hydrate Deposits. Society of Petroleum Engineers. doi:10.2118/131792-PA

Mullin, J. W. (2001). *Crystallization*. Elsevier.

Ohmura, R., Matsuda, S., Uchida, T., Ebinuma, T., & Narita, H. (2005). Clathrate hydrate crystal growth in liquid water saturated with a guest substance: observations in a methane+ water system. *Crystal growth & design*, *5*(3), 953-957.

Peng, B. Z., Dandekar, A., Sun, C. Y., Luo, H., Ma, Q. L., Pang, W. X., & Chen, G. J. (2007). Hydrate film growth on the surface of a gas bubble suspended in water. *The Journal of Physical Chemistry B*, *111*(43), 12485-12493.

Ripmeester, J. A., John, S. T., Ratcliffe, C. I., & Powell, B. M. (1987). A new clathrate hydrate structure. *Nature*, *325*(6100), 135-136.

Rodger, P. M. (2000). Methane hydrate: melting and memory. *Annals of the New York Academy of Sciences*, *912*(1), 474-482.

Ruppel, C. (2011). Methane hydrates and the future of natural gas. *MITEI natural gas Report, supplementary paper on Methane Hydrates*, *4*, 25.

Saito, K., Kishimoto, M., Tanaka, R., & Ohmura, R. (2010). Crystal growth of clathrate hydrate at the interface between hydrocarbon gas mixture and liquid water. *Crystal Growth & Design*, *11*(1), 295-301.

Schoderbek, D., Martin, K. L., Howard, J., Silpngarmlert, S., & Hester, K. (2012). North slope hydrate fieldtrial: CO2/CH4 exchange. In *OTC Arctic Technology Conference*. Offshore Technology Conference.

Servio, P., & Englezos, P. (2003). Morphology of methane and carbon dioxide hydrates formed from water droplets. *AIChE Journal*, *49*(1), 269-276.

Skauge (2016). *Compendium PTEK312: Pore scale physics and network modelling*. CIPR.

Sloan Jr, E. D. (2003). Fundamental principles and applications of natural gas hydrates. *Nature*, *426*(6964), 353.

Sloan Jr, E. D., & Koh, C. (2008). *Clathrate hydrates of natural gases*. CRC press.

Sloan, E. D., Koh, C. A., & Sum, A. K. (2010). Gas hydrate stability and sampling: the future as related to the phase diagram. *Energies*, *3*(12), 1991-2000.

Song, Y., Cheng, C., Zhao, J., Zhu, Z., Liu, W., Yang, M., & Xue, K. (2015). Evaluation of gas production from methane hydrates using depressurization, thermal stimulation and combined methods. *Applied Energy*, *145*, 265-277.

Staykova, D. K., Kuhs, W. F., Salamatin, A. N., & Hansen, T. (2003). Formation of porous gas hydrates from ice powders: Diffraction experiments and multistage model. *The Journal of Physical Chemistry B*, *107*(37), 10299-10311.

Steed, J. W., & Atwood, J. L. (2009). *Supramolecular chemistry*. John Wiley & Sons.

Tamaki, M., Fujii, T., & Suzuki, K. (2017). Characterization and Prediction of the Gas Hydrate Reservoir at the Second Offshore Gas Production Test Site in the Eastern Nankai Trough, Japan. *Energies*, *10*(10), 1678.

Tanaka, R., Sakemoto, R., & Ohmura, R. (2009). Crystal growth of clathrate hydrates formed at the interface of liquid water and gaseous methane, ethane, or propane: variations in crystal morphology. *Crystal Growth and Design*, *9*(5), 2529-2536.

Tang, L. G., Li, X. S., Feng, Z. P., Li, G., & Fan, S. S. (2007). Control mechanisms for gas hydrate production by depressurization in different scale hydrate reservoirs. *Energy & Fuels*, *21*(1), 227-233.

Taylor, C. J., Miller, K. T., Koh, C. A., & Sloan Jr, E. D. (2007). Macroscopic investigation of hydrate film growth at the hydrocarbon/water interface. *Chemical Engineering Science*, *62*(23), 6524-6533.

The engineering toolbox (n.d.; *a*). Refractive Index for Some Common Liquids, Solids and Gases. Retrieved April 17, 2018, from: http://www.engineeringtoolbox.com/refractive-index-d_1264.html

The engineering toolbox (n.d.; *b*). Solubility of gases in water. Retrieved May 23, 2018, from: https://www.engineeringtoolbox.com/gases-solubility-water-d_1148.html

Tohidi, B., Anderson, R., Clennell, M. B., Burgass, R. W., & Biderkab, A. B. (2001). Visual observation of gas-hydrate formation and dissociation in synthetic porous media by means of glass micromodels. *Geology*, *29*(9), 867-870.

Wilson, P. W., & Haymet, A. D. J. (2010). Hydrate formation and re-formation in nucleating THF/water mixtures show no evidence to support a “memory” effect. *Chemical engineering journal*, *161*(1-2), 146-150.

Wu, R., Kozielski, K. A., Hartley, P. G., May, E. F., Boxall, J., & Maeda, N. (2013). Methane–propane mixed gas hydrate film growth on the surface of water and Luvicap EG solutions. *Energy & Fuels*, *27*(5), 2548-2554.

Yamamoto, K., Terao, Y., Fujii, T., Ikawa, T., Seki, M., Matsuzawa, M., & Kanno, T. (2014). Operational overview of the first offshore production test of methane hydrates in the Eastern Nankai Trough. In *Offshore Technology Conference*. Offshore Technology Conference.

Yanlong, L. I., Gaowei, H. U., Changling, L. I. U., Nengyou, W. U., Qiang, C. H. E. N., Lele, L. I. U., & Chengfeng, L. I. (2017). Gravel sizing method for sand control packing in hydrate production test wells. *Petroleum Exploration and Development*, *44*(6), 1016-1021.